

High-bandwidth microrheology of cytoskeletal networks



Dissertation
for the award of the degree
“Doctor rerum naturalium”
of the
Georg-August-Universität Göttingen

submitted by
Marcel Bremerich
from Northeim, Germany

Göttingen, November 2011

Members of the thesis committee

Prof. Dr. Christoph F. Schmidt (1st reviewer and supervisor)
Drittes Physikalisches Institut - Biophysik
Georg-August-Universität Göttingen

Prof. Dr. Eberhard Bodenschatz (2nd reviewer)
Labor für Hydrodynamik, Strukturbildung und Nanobiokomplexität
Max-Planck-Institut für Dynamik und Selbstorganisation, Göttingen

Prof. Dr. Annette Zippelius
Institut für Theoretische Physik - Statistische Physik
Georg-August-Universität Göttingen

Date of the oral examination: 18.01.2012

Declaration

I herewith declare that I have produced this dissertation without the prohibited assistance of third parties and without making use of aids other than those specified; notions taken over directly or indirectly from other sources have been identified as such. This dissertation has not previously been presented in identical or similar form to any other German or foreign examination board.

The thesis work was conducted from December 2007 to November 2011 under the supervision of Prof. Dr. Christoph F. Schmidt at the Third Institute of Physics - Biophysics.

Göttingen, 30.11.2011

In Erinnerung an

Joachim & Doris Bremerich.

Ihr lehrtet mich Leben,

Ihr lehrtet mich Sterben.

Contents

Contents	v
List of Figures	vii
List of Tables	xi
Glossary	xiii
1 Introduction	1
2 Optical trapping	3
2.1 Theory	4
2.2 Acousto- and electro-optical deflection	5
2.2.1 The acousto-optical effect	6
2.2.2 The electro-optical effect	7
2.3 Back-focal-plane interferometry	8
2.4 Calibration of optical traps	10
2.5 Construction of an optical trapping setup for microrheology	12
2.5.1 Design of the beam-steering optics	13
2.5.2 Design of the microscope	16
2.5.3 Data acquisition	21
2.6 Characterization of the microrheology setup	22
2.6.1 Quantifying noise	22
2.6.2 Performance of AOD and EOD beam steering	23

CONTENTS

3	Microrheology	29
3.1	Introduction	29
3.2	The fluctuation-dissipation theorem and linear response	29
3.3	The shear modulus	31
3.4	A particle confined by a harmonic potential	32
3.4.1	Active microrheology	32
3.4.2	Passive microrheology	33
3.5	Two-particle microrheology	35
3.6	Microrheology measurements in water	36
4	Composite networks	39
4.1	Biopolymers and motor proteins	41
4.1.1	Microtubules	41
4.1.2	Actin filaments	43
4.1.3	Motor proteins	45
4.2	Microrheology of cytoskeletal model systems	46
4.2.1	Single-component networks of microtubules	46
4.2.2	Nonequilibrium networks of microtubules and DK4mer	53
4.2.3	Composite networks of microtubules and F-actin	59
4.2.4	Composite networks with cross-linkers	64
4.2.5	Nonequilibrium composite networks	65
4.3	Discussion and outlook	68
5	Stiff-filament microrheology	71
5.1	Filament bending modes	73
5.2	Results	75
5.3	Discussion	82
5.4	Conclusions and outlook	84
6	Intracellular measurements	87
6.1	Measurements in COS-cells	87
6.2	Results	88
6.3	Discussion and outlook	90
7	Summary and outlook	93

Appendix A Biochemical protocols	95
A.1 Microtubule preparation	95
A.2 Actin preparation	95
A.3 Microtubules and DK4mer	96
A.4 Preparation of composite networks	96
A.5 Labeling of microtubules with gold beads	96
A.5.1 Embedding labeled microtubules in F-actin	97
A.6 Cell culture	97
Appendix B MATLAB-programs	99
Appendix C Alignment procedure for the optical trapping setup	103
C.1 Setting up chassis and camera	103
C.2 Laser alignment	104
C.3 Implementing telescope lenses	108
C.4 Alignment of the detection part	110
C.4.1 Aligning the quadrant photodiodes	112
C.4.2 Setting up Köhler illumination for DIC	113
C.5 Alignment of AODs and EODs	115
C.6 Conversion factors	118
References	121
Danksagung	130

CONTENTS

List of Figures

2.1	Ray optics description of particle trapping	5
2.2	Principle of acousto-optical deflection	6
2.3	Electro-optical beam deflection	8
2.4	Back-focal-plane interferometry	9
2.5	2D-detector response function	10
2.6	Calibration of the optical trap	11
2.7	Schematic layout of the microrheology setup	14
2.8	Beam deflection by one of the EODs	16
2.9	Beam steering optics of the setup	17
2.10	Microscope slider for a dichroic mirror	19
2.11	Design and realization of the microscope chassis	21
2.12	Noise measurement	23
2.13	Measurement of sample creep	24
2.14	QPD response curves	25
2.15	System response	26
3.1	Shear modulus for water measured with the new microrheology setup	37
4.1	Microtubule structure	41
4.2	Structure of actin filaments	44
4.3	Cloning of the tetrameric chimera DK4mer	45
4.4	Shear modulus of a microtubule network obtained from 1PMR	47
4.5	Shear modulus of a microtubule network obtained from 1AMR	48
4.6	Comparison of active and passive measurements	49
4.7	Two-particle passive data	50

LIST OF FIGURES

4.8	Two-particle active data	51
4.9	Comparison of one- and two-particle experiments	52
4.10	Shear moduli for different tubulin concentrations	53
4.11	Microtubule aster	54
4.12	Bead aggregate in a nonequilibrium network	55
4.13	Nonequilibrium network at lower motor concentration	55
4.14	Response of a microtubule network with and without DK4mer	56
4.15	Network stiffening	57
4.16	Variation of the shear modulus for all measured samples	58
4.17	Comparison of equilibrium and nonequilibrium network	59
4.18	Confocal images of microtubule and composite networks	60
4.19	One-particle active measurement in the composite network	61
4.20	Comparison of shear moduli obtained by one- and two-particle data	62
4.21	Composite versus single-component networks	63
4.22	Composite network with cross-linked microtubules	64
4.23	Shear moduli for composite networks with and without cross-links	65
4.24	Response function of composite with and without motors	66
4.25	Stiffening of the composite in the presence of motor proteins	68
5.1	Bead versus stiff filament microrheology	72
5.2	Example of power spectra for one microtubule	76
5.3	Power spectra for different beads on the same microtubule	77
5.4	Least squares fit of a power spectrum	78
5.5	Ratio of parallel and perpendicular power spectra	80
5.6	Shear modulus of F-actin	81
5.7	Viscous cross-over	83
6.1	Microscope image of a COS-cell with injected beads	88
6.2	Intracellular shear moduli obtained from 1PMR	89
6.3	Imaginary part of the intracellular complex response function	90
C.1	Reflections at the bottom glass–water interface	106
C.2	Images of the laser profile in the back-focal plane	113
C.3	Illumination light path	114

LIST OF FIGURES

C.4 EOD input polarization 118

LIST OF FIGURES

List of Tables

5.1	Ratio of power spectra	81
C.1	Distances between beam steering optics	107
C.2	Distances between illumination optics	116
C.3	Conversion factors for the optical deflectors	118

LIST OF TABLES

Glossary

1AMR	One-particle active microrheology	BFP	Back-focal-plane
1PMR	One-particle passive microrheology	DIC	Differential interference contrast
2AMR	Two-particle active microrheology	EOD	Electro-optical deflector
2PMR	Two-particle passive microrheology	F-actin	Filamentous actin
ADP	Adenosine diphosphate	FDT	Fluctuation-dissipation theorem
AMR	Active microrheology	G-actin	Globular actin
AOD	Acousto-optical deflector	GDP	Guanosine diphosphate
ATP	Adenosine-5'-triphosphate	GTP	Guanosine-5'-triphosphate
		LED	Light emitting diode
		MSD	Mean square displacement
		NA	Numerical aperture
		PBS	Polarizing beam splitter
		PMR	Passive microrheology
		PSD	Power spectral density
		QPD	Quadrant photodiode

GLOSSARY

1

Introduction

All multi-cellular organisms are composed of highly structured, autonomous and complex building blocks, the biological cells. These units show a wealth of functionality ranging from information storage in their DNA, growth and division to proliferate, interaction with the environment by chemical and also mechanical processes and a complex metabolism to harvest energy and sustain these functions.

The morphology of cells and their mechanical properties are closely linked to a protein scaffold called the cytoskeleton, which is found in the cytoplasm of most eukaryotic cells¹. The cytoskeleton, despite its name, is not a rigid supporting structure only responsible for the overall cell shape. On the contrary, it generates and supports a remarkable variety of cellular functions which can be highly dynamic and happen on a wide range of time scales. It plays a crucial role in cell growth, locomotion and division. It has the capability of large scale reorganization, which can be seen for example in the contractility of cardiac muscle cells or the flexibility of erythrocytes squeezing through tiny blood vessels. The cytoskeleton provides the infrastructure for the intracellular transport along which vesicles and organelles are transported by motor proteins. Last but not least, it provides the cell with the ability of mechanosensing, i.e. response to external mechanical stimuli. This is apparent, for example, in hair cells turning an impinging sound wave into an electrical nerve signal. Recent research has also shown that tissue cells possess a feedback mechanism by which they can sense and respond to the

¹What has been once thought of as a unique feature of eukaryotic cells, has also recently been identified in prokaryotic cells. Homologous proteins in prokaryotic cells were found showing similar functionality to their “relatives” in eukaryotes. (See for example the review by Shih and Rothfield (1).)

1. INTRODUCTION

local matrix stiffness (2) and that this can even direct stem cell lineage specification, as shown by Engler et al. (3).

The mechanical basis for these properties is the cytoskeleton and its components: filamentous biopolymers and a variety of accessory proteins binding to them. Understanding the organization and assembly of this versatile “scaffold” is one of the great challenges of cell biology and biophysics (4).

The investigation of the mechanical behavior of biological matter is related to the field of soft condensed matter in general and rheology in particular. Rheology, as the science of flow and deformation of matter, is the theoretical and experimental approach to characterize the response of a material to an applied stress. In classical large-scale rheometers, bulk properties of viscoelastic materials are probed on a macroscopic length scale and a narrow range of frequencies. A special variant has been developed over the last decades, termed *microrheology*, which comprises several experimental techniques to extend the temporal resolution down to microseconds and capture features on micrometer length scales (5).

The aim of the research described in this thesis was the development of a new optical trapping based microrheology setup, which employs state-of-the-art technology and outperforms existing devices. On the experimental side, the study of *in vitro* model systems mimicking the properties of cytoskeletal networks was the focus of this research, to pave the way for intracellular measurements.

2

Optical trapping

The very core of microrheology experiments with high spatial and temporal resolution is particle tracking and manipulation using an optical trapping setup. In the 1970s, Ashkin and coworkers pioneered the laser-based optical trap in several ground-breaking papers (6, 7, 8). The radiation pressure of coherent light sources has been shown to have the ability to manipulate dielectric particles and even confine them in three dimensions. Since their invention, optical traps found a wide range of applications in many fields, especially in the study of biological systems (9).¹

An optical trap is easily combined with conventional light microscopy. While observing biological specimens, forces of hundreds of piconewtons can be applied to micrometer-sized particles and organelles. The excellent overlap with the dimensions encountered on the cellular level of biological systems makes optical trapping an ideal technology to gain deeper insight into subcellular processes. A very detailed resource letter containing all important contributions to this field over the last decades has been written by Lang and Block (10).

In this chapter, a brief introduction to the theoretical foundation of optical trapping is given, as well as the most important experimental techniques for improved functionality and characterization. The construction of a new optical trapping setup specifically designed for microrheology experiments is described in section 2.5, followed by the characterization of its performance in 2.6.

¹Optical traps in biological contexts are also termed “optical tweezers”.

2. OPTICAL TRAPPING

2.1 Theory

Photons impinging on a dielectric particle will apply a force to them based on their momentum transfer upon scattering. In practice, lenses with high numerical aperture (NA) are used to tightly focus a laser beam, which results in highly convergent rays interacting with particles close to the focus. This gives rise to another force component, usually called the “gradient force”, in contrast to the aforementioned “scattering force”. The physical origin of these forces is exactly the same, i.e. the momentum transfer by deflected photons. The decomposition highlights the direction of the force, which is oriented parallel to the optical axis of the laser for the scattering force and towards the focus for the gradient force respectively. The scattering force tends to push the particle away from the light source and is usually the dominating contribution far from the focus. However, a dipole exposed to an inhomogeneous electric field will experience a force in the direction of the field gradient. If this force component exceeds the scattering force, stable trapping is possible. Very steep gradients are necessary to achieve this, requiring the use of high NA objectives, which are able to produce a diffraction-limited focus.

The theoretical description of optical trapping usually depends on the size of the trapped object. In the regime of Mie-scattering, where the object’s dimension is larger than the wavelength of the trapping light, ray optics can be applied. If a light beam impinges on a spherical object with a refractive index higher than the surrounding, it will undergo refraction and a change of momentum is transferred to the object. The resulting force can be calculated directly (11) and a schematic picture is drawn in figure 2.1.

In the limit of particles much smaller than the wavelength of the trapping laser, i.e. the Rayleigh regime, the approximation of a point-like dipole interacting with the electric field holds. In this case the scattering force is

$$F_{scatter} = \frac{n_m \sigma I}{c}, \quad (2.1)$$

where n_m is the refractive index of the medium, σ is the scattering cross-section of the particle, I denotes the intensity and c the speed of light. Via the scattering cross-section this force depends on the size of the object, the wavelength of the trapping laser and

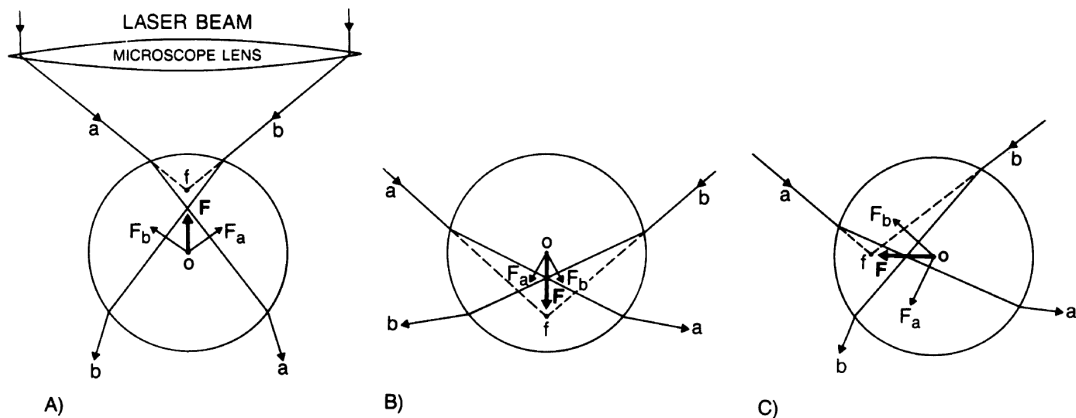


Figure 2.1: Ray optics description of particle trapping - Light coming from a laser is focused by a microscope objective. The rays a and b impinge on a spherical object displaced axially or transversely from the focus and undergo refraction. The sum of the resulting forces F_a and F_b is always directed towards the focus, therefore pulling the object back into focus. Figure adopted and modified from (11).

the ratio of refractive indices between particle and surrounding. The gradient force is given by the Lorentz force acting on the particle:

$$F_{grad} = \frac{\alpha}{2} \nabla \langle E^2 \rangle, \quad (2.2)$$

with the polarizability α of the particle, which again depends on the size of the object and ratio of refractive indices. In practice, the size of the trapped object lies usually in between the above mentioned Mie- and Rayleigh-regimes. This necessitates a more complex description in terms of a generalized Lorenz-Mie theory (12), which is beyond the scope of this introduction.

2.2 Acousto- and electro-optical deflection

In order to move and manipulate particles in a sample, the optical trap has to be positioned precisely in the focal plane. By employing rapid beam-steering, computer-controlled feedback-mechanisms allow position and force clamp experiments (13, 14, 15). Moreover, by rapidly altering the trap position, multiple “time-shared” traps can be realized (16).

In practice, lenses and mirrors can be used to rotate the direction of the trapping laser. Via telescopes these rotations are imaged into the objective’s back-focal-plane

2. OPTICAL TRAPPING

and result in pure lateral movement of the trap in the focal plane. This way the collimation of the trapping laser can be preserved.

For precision beam-steering with a response time in the microsecond-regime, optical deflectors are the devices of choice. In this work, acousto- as well as electro-optical deflectors are employed, and their operating principle is briefly described in the following subsections.

2.2.1 The acousto-optical effect

The diffraction of light at a grating is a well-described phenomenon (17). Diffraction at a grating in a volume of material can be achieved by periodic modulation of, for example, the refractive index n (phase grating). This can be induced in transparent optical crystals by applying an ultrasonic wave with a piezoelectric transducer, resulting in periodic changes of the material's density and hence the index of refraction. Since the speed of light is much faster than the sound velocity v in the crystal, the grating pattern can be considered stationary and a laser beam impinging at the Bragg angle is deflected by this grating into the first diffraction order. The deflection angle is given by:

$$\Delta\theta = \arcsin \frac{\lambda}{n\Lambda} \approx \frac{\lambda}{n\Lambda} = \frac{\lambda f}{nv}, \quad (2.3)$$

with the laser wavelength λ and acoustic wavelength $\Lambda = f/v$. Changing the frequency of the sound wave f results in a modification of the grating constant and thus the diffraction angle. This principle is schematically depicted in figure 2.2.

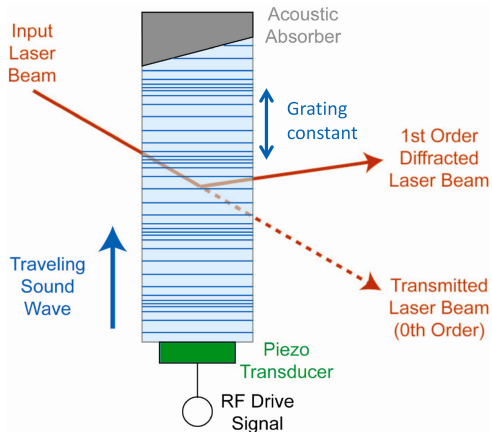


Figure 2.2: Principle of acousto-optical deflection - A radio-frequency signal drives the piezoelectric transducer glued to the acousto-optical crystal. Changes of material density (blue lines) are generated by the ultrasonic wave. A laser beam (orange) is diffracted by this phase grating. Figure adopted and modified from (18).

The response time is limited by the time the acoustic wave needs, to reach and cross the laser spot inside the crystal.

Since the acoustic wave cannot be completely absorbed at the end of the crystal, unwanted backreflections interfere with the counterpropagating wave. This reduces the response time and causes nonlinearities in the deflection angle (19).

2.2.2 The electro-optical effect

The electro-optical or Pockels effect is a nonlinear, quadratic optical effect, which produces birefringence in crystals without inversion symmetry, if subject to a varying or constant electric field (17).

If a linear polarized, monochromatic wave impinges on a nonlinear crystal subject to a static electric field E_{stat} , the solution of the nonlinear wave equation predicts the occurrence of another wave depending on the crystal's orientation, with a phase shift and polarization at 90° to the original beam. Depending on the length of the crystal, elliptically polarized light exits the crystal. The change of polarization can also be described in terms of a change in refractive index of the material. Depending on the symmetry and structure of the crystal, this change can be expressed as:

$$\Delta n \approx -\frac{n^3}{2} r E_{stat}, \quad (2.4)$$

where n is the central refractive index and r the electro-optical tensor, which depends on the crystal's orientation and the polarization of the incoming light.

In a simple geometry two crystals can be glued together, with opposing orientation of their optical axes. This way the change of refractive index encountered by an incident wave is positive in one crystal and negative in the other, yielding a refractive index gradient. This is depicted in figure 2.3. Due to the index grating, the crystal acts as a prism and deflects the beam at an angle:

$$\theta \propto L \Delta n = L n^3 r E_{stat}, \quad (2.5)$$

where L is the length of the crystal.

2. OPTICAL TRAPPING

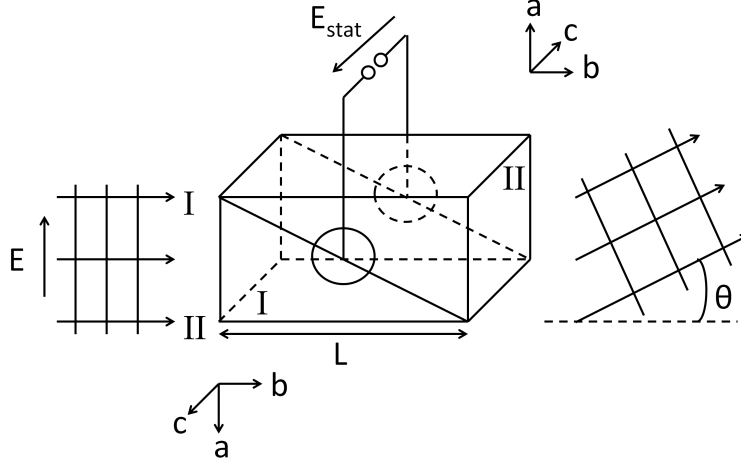


Figure 2.3: Electro-optical beam deflection - Two nonlinear crystals with opposing orientation glued together. The beam *I* experiences a different optical path length than beam *II*, resulting in a deflection of the entire beam by θ . Figure modified and adopted from (17).

2.3 Back-focal-plane interferometry

For quantitative measurements of force and displacement with an optical trap, a position detection scheme has to be employed, which ideally measures with high spatial and temporal resolution. A very convenient way to detect the motion of a particle trapped in the focal volume of an optical trap is to make an interferometric measurement, based on back-focal-plane (BFP) detection (20). In this method, the trapping laser itself is used to detect the bead's motion, instead of, for example, the microscope's camera. An overview of different detection techniques can be found in the review by Neuman and Block (21).

After passing the sample and the trapped object, the laser light is collected by the condenser. Unscattered light and light scattered by the bead interfere, and this leads to intensity shifts in the BFP of the condenser lens. This pattern does not depend on the actual position of the focus in the specimen plane, which allows repositioning of the optical trap during the experiment without any change in the detection.

The interference pattern is imaged onto a segmented photodiode, usually a quadrant photodiode (QPD). This is schematically depicted in figure 2.4. The signals from the quadrants are summed pairwise and the differential signal is calculated from both pairs

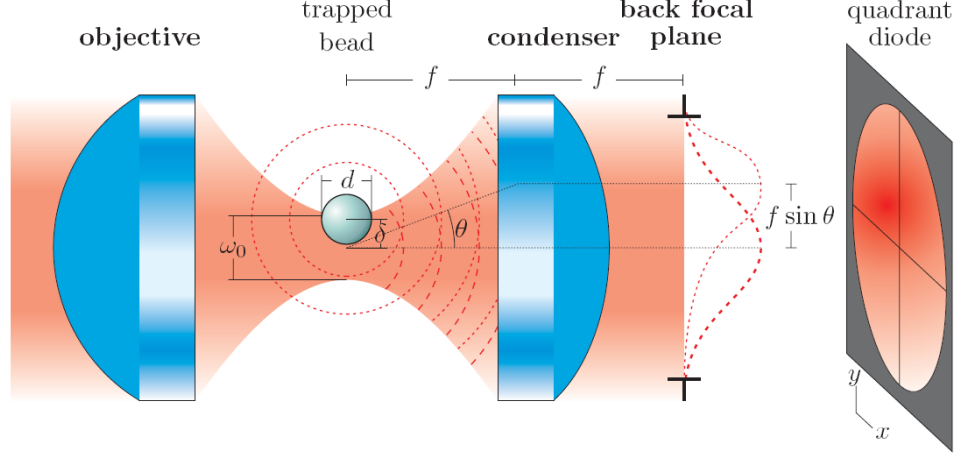


Figure 2.4: Back-focal-plane interferometry - A lateral displacement of a trapped particle from the trap center is shown. Scattered and transmitted light are collected by the condenser and far-field interference results in a shift of the intensity distribution in the back-focal-plane. This plane is imaged onto a quadrant diode, allowing a lateral resolution of the displacement down to the Å-regime. Figure adopted from (22).

in the x- and y-directions. This differential signal is then normalized by the sum signal of the whole QPD (22). A lateral bead displacement x causes an angular intensity change by interference. The resulting detector response for first-order interference has been calculated to be:

$$D = \frac{I_+ - I_-}{I_{sum}} \approx 32\sqrt{\pi} \frac{n_s \alpha}{\lambda_L w^2} e^{-2\left(\frac{\delta}{w}\right)^2} \int_0^{\delta/w} t^2 dt, \quad (2.6)$$

where D is the normalized differential signal. Here, α represents the polarizability of the particle, w is the radius of the focus and λ_L is the laser wavelength. The integral (called the Dawson's function) is closely related to the error function and can be calculated numerically (23). This expression was derived in the approximation of a Rayleigh scatterer, but also agrees with the measured response for larger particles.¹ The typical S-shaped response curve can be measured by scanning the laser across a fixed bead and recording the QPD signal. Figure 2.5 shows the signal from one channel, plotted over the lateral position for a 1 μm bead scanned in two dimensions by the optical trap.

¹An expression similar to 2.6 was found by Pralle et al. (24) for the particle's axial position, allowing particle-tracking in three dimensions. Throughout this thesis, only two-dimensional data has been recorded.

2. OPTICAL TRAPPING

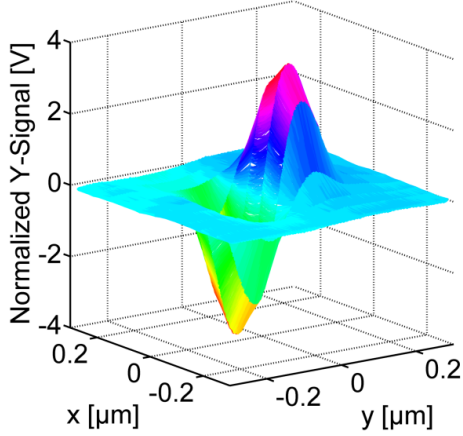


Figure 2.5: 2D-detector response function - Two-dimensional response curve obtained by scanning a fixed 1 μm bead with the optical trap, while recording the y-channel. The step size of the scanning in the x-direction was much wider than for the y-direction.

If the laser is displaced by a known magnitude within the linear regime of the response, the detector signal can be calibrated and converted into physical units of length. This calibration procedure is treated in the following section.

2.4 Calibration of optical traps

The voltage signals from the QPDs have to be converted to a physical unit of length to make a displacement measurement. Also the force of the trap on the bead has to be measured and be accounted for during the data analysis. Several techniques have been developed to facilitate this (21, 25, 26, 27, 28).

The calibration factor $cal = u(t)/v(t)$ in [m/V], as well as the stiffness κ of the trap can be obtained by calculating the power spectral density (PSD) of the position fluctuations for a trapped probe particle in water. From the Langevin-type equation of motion, the theoretically expected form of the PSD is that of a Lorentzian (29):

$$C(\omega) = \frac{2k_bT}{\gamma(\omega_c^2 + \omega^2)}, \quad (2.7)$$

where $\omega_c = \kappa/\gamma$ is the corner frequency and γ is the drag coefficient given by the Stokes formula $\gamma = 6\pi\eta r$, with the particle radius r and the viscosity η of the fluid. Knowing the bead diameter, the solvent viscosity and temperature, one can obtain cal and κ by fitting a Lorentzian to the measured data. This is done by the MATLAB (The MathWorks Inc, Natick, MA, USA) program TweezerCalib 2.1 as published by Hansen et al. (30) and described in (31). The fitting routine based on references (25, 32)

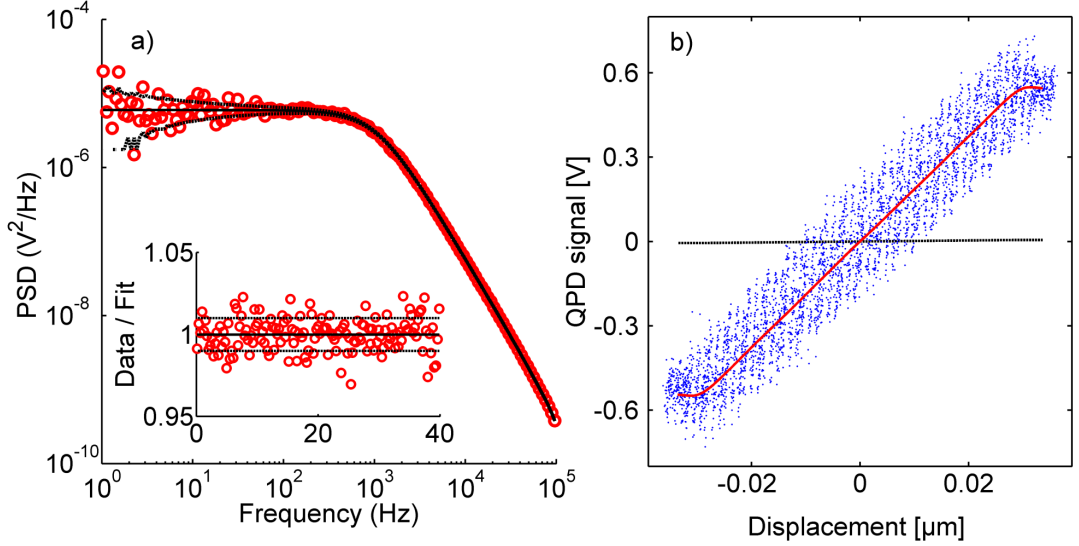


Figure 2.6: Calibration of the optical trap - a) Lorentzian fit (solid line) to the power spectrum obtained from the fluctuations of a $1\ \mu\text{m}$ bead in water (open circles). The inset shows the ratio of measured and theoretical spectrum. Dotted lines indicate \pm one standard deviation. The fit was performed using the TweezerCalib 2.1 Matlab program from (30). The corner frequency yields a trap stiffness of $\kappa = 6.6 \cdot 10^{-5}\ \text{N/m}$, and the calibration factor is computed to be $cal = 5.48 \cdot 10^{-8}\ \text{m/V}$. b) Scatter plot of the raw data of the detector response for rapid laser scanning with the EOD. The amplitude of the scan was $0.3\ \mu\text{m}$, the frequency was $5\ \text{kHz}$. The raw data is averaged and interpolated (solid line) and corrected for the background signal obtained by scanning the laser without a bead (black line). A polynomial fit is performed and the maximal negative slope in the linear regime gives the inverse of the calibration factor, which was found to be $5.25 \cdot 10^{-8}\ \text{m/V}$

accounts for a number of experimental factors, such as hydrodynamic interactions, aliasing, electronic filters and for filtering caused by the QPDs (33). A typical fit of a PSD for a $1\ \mu\text{m}$ bead in water can be seen in figure 2.6a, showing excellent agreement between the measured data and the fit. The corner frequency yields a trap stiffness of $\kappa = 6.6 \cdot 10^{-5}\ \text{N/m}$, and the calibration factor is computed to be $cal = 5.48 \cdot 10^{-8}\ \text{m/V}$.

The derivation of the calibration factor using this method is based on the fluctuation-dissipation theorem (FDT, see chapter 3.2) as well as assumptions on the bead's diameter and the viscosity of the solvent, which is typically strongly temperature dependent. The bead diameter is subject to polydispersity due to the fabrication process. The viscous drag coefficient can be influenced by surfaces in the vicinity, and laser-induced

2. OPTICAL TRAPPING

heating of the solvent can change the local temperature. This method neither works in a viscoelastic environment nor in a nonequilibrium system, where the FDT does not hold.

A method to obtain the calibration factor independently from these parameters has been introduced by Vermeulen et al. (34). The trap laser is rapidly scanned over the trapped bead, such that the bead cannot follow the oscillation. At the same time, the QPD signal is recorded. Knowing the factor between beam displacement and modulation voltage, one can fit the detector's response curve linearly, and the inverse of the maximum slope gives the calibration factor. Figure 2.6b shows the result for the same $1\ \mu\text{m}$ bead as was used above, driven by the EOD. A calibration factor of $cal = 5.25 \cdot 10^{-8}\ \text{m/V}$ was obtained, agreeing to within 5% with the aforementioned value derived by the power spectrum method. Both methods in general agreed to within an experimental error margin of 10% for both AODs and EODs.

2.5 Construction of an optical trapping setup for microrheology

One major goal of this thesis was the construction of a new microrheology setup. The existing setup suffers from low-frequency noise from thermal drift, for example, due to its large dimensions and its aluminum composition.

The new setup was planned to consist of a custom-built inverted microscope, where the objective is pointing upwards at the sample. It was constructed in a compact fashion from a material with a low thermal expansion coefficient. An austenitic stainless steel was chosen (EN steel number 1.4305, X8CrNiS18-9), with a thermal expansion coefficient of $\alpha = 16 \cdot 10^{-6}\ \frac{1}{\text{K}}$. Furthermore, several options and new technologies were implemented into the setup:

- Illumination with high-power light emitting diodes (LED) for differential interference contrast (DIC) microscopy. Bormuth et al. showed that LEDs are a low-cost and easy to align alternative to existing illumination solutions and perform equally well (35).
- Fluorescence wide-field illumination for observing fluorescently labeled biological samples.

2.5 Construction of an optical trapping setup for microrheology

- 3D sample positioning with a high-resolution piezostage.
- Several trapping lasers with different wavelengths, for the elimination of cross-talk during two-particle measurements (36).
- Acousto-optical deflectors (AODs) for beam steering (see chapter 2.2).
- Electro-optical deflectors (EODs) for high-performance beam steering with higher bandwidth (see chapter 2.2). In reference (19), Valentin et al. showed, that EODs offer a greater throughput, reduced variation in transmittance with deflection and increased linearity. Furthermore, their deflection does not depend on the wavelength. This makes it possible to use multiple lasers with different colors in the same setup.

The design of the new setup can roughly be divided into two major parts, described in the following sections:

1. The beam steering optics to manipulate the trapping laser and couple it into the microscope chassis.
2. The microscope, i.e. the chassis, which itself consists of two parts:
 - The bottom part with the objective, the sample holder with 3D-positioning devices, slots for coupling in the trapping lasers, additional optics and a camera for the image acquisition.
 - An upper part containing the condenser, the illumination and the detection optics for back-focal-plane interferometry.

Before starting the design of the setup, a few decisions had already been made concerning the components and optics employed, for example the type of trapping laser, camera and objective, thereby setting the “boundary conditions”.

2.5.1 Design of the beam-steering optics

A schematic layout of the beam-steering optics is shown in figure 2.7. The setup is equipped with two optical traps of perpendicular polarization, which are independently steerable with acousto- and electrooptical deflectors. Three linearly polarized near infrared lasers (Compass, ND:YV04, 1064 nm, 4 W, Coherent Inc., Santa Clara, CA,

2. OPTICAL TRAPPING

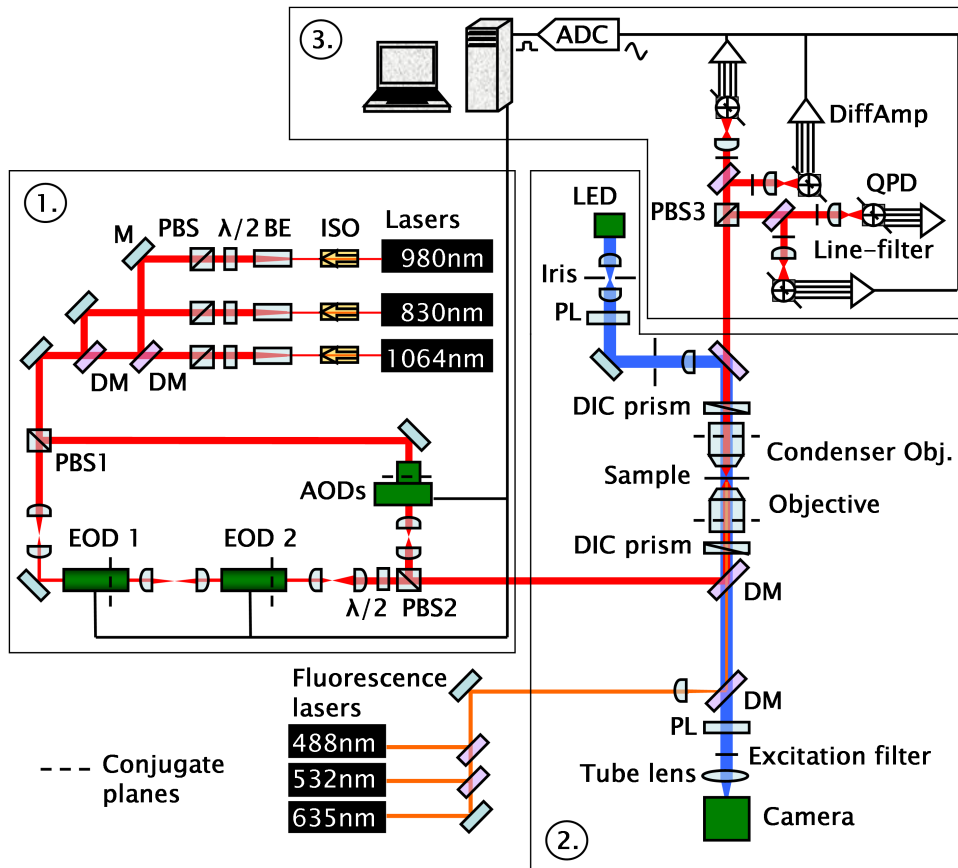


Figure 2.7: Schematic layout of the microrheology setup - The setup can be roughly divided into three parts: (1) The beam steering optics, (2) the microscope including both objectives and the illumination and (3) the detection part. The trapping lasers pass through an optical isolator (ISO), a beam expander (BE), a half-wave plate and a polarizing beam splitter (PBS). PBS1 splits the beam up into two paths, in which the AODs and EODs are placed. The lasers are recombined by PBS2 and coupled into the microscope via a dichroic mirror (DM). After passing the objective, the lasers are split up again by PBS3 and imaged onto the QPDs. DIC-illumination is coupled in from above and fluorescence from below the sample.

2.5 Construction of an optical trapping setup for microrheology

USA; PTG-IQ2C-980-350 laserdiode 980 nm, 210 mW and PTG-IQ1C-830-150, 830 nm, 130 mW, both Laser 2000 GmbH, Wessling, Germany) are used, which are protected against back reflections by optical isolators (IO-5-1064-VHP, IO-5-980-HP and IO-3D-830-VLP, Thorlabs, Newton, NJ, USA). The diameter of all three beams is increased to 4 mm with variable beam expanders (Qioptiq Photonics GmbH & Co KG, München, Germany). A combination of a half-wave plate and a Glan-laser polarizer is used to adjust the intensity while running the laser at high power for increased stability.

The laser beam is then split into two orthogonally polarized beams by a 90° Glan-laser polarizing beam splitter (Artifex Engineering, Emden, Germany; “PBS1” in figure 2.7). By changing the orientation of the polarizers relative to the beam splitter, the ratio of powers in the two beams can thus be altered.

The beam transmitted by PBS1 passes through a pair of electro-optical deflectors (ConOptics Inc., Danbury, CT, USA) for precision beam steering in the lateral direction. To match the small aperture size of the deflectors’ crystals, the beam width is reduced by a pair of telescope lenses. After the first EOD, a second telescope images its deflection plane into the second EOD, oriented at 90° to the first one. Despite the length of the EOD of 12.5 cm, an effective deflection plane could be identified in accordance with the findings in (19). The deflected beam was traced back for several deflection angles (see figure 2.8). By linear fitting the data points, a deflection plane around 59 ± 22 mm behind the exit face could be found. Due to the large error, a different approach was tested as well. The laser was oscillated, and with a one-to-one telescope a specific plane inside of the EOD crystal was imaged onto a quadrant photodiode. By altering the EOD’s position relative to the telescope, a plane with minimal amplitude of the oscillation could be found around 50 ± 5 mm behind the EOD’s exit face.

After the second EOD, a third telescope expands the beam again to overfill the objective’s back aperture, and the deflection planes are imaged into the back-focal plane of the objective. The corresponding conjugate planes are marked with dashed lines in figure 2.7. A multi-order half-wave plate restores the original polarization of the beam, which has been altered by half-wave plates mounted inside of the EODs, since the EODs’ deflection only occurs in the direction of the polarization.

The beam reflected at PBS1 is directed through a pair of acousto-optical deflectors (DTSXY-400, AA optoelectronic, Orsay Cedex, France) and again expanded by another

2. OPTICAL TRAPPING

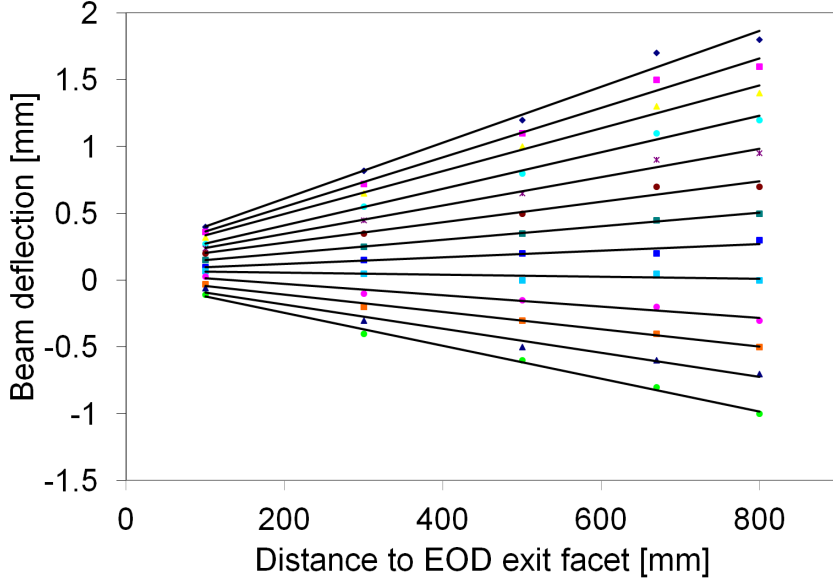


Figure 2.8: Beam deflection by one of the EODs - The laser beam was deflected by the EOD by applying a constant voltage to the driver. The deflection was measured for several voltages at different locations behind the EOD with a beam profiler. A linear fit to the data points revealed a deflection plane at $\approx 59 \pm 22$ mm behind the exit face.

telescope.

Both beams are recombined by the polarizing beam splitter PBS2 and directed towards the microscope. In figure 2.9 a picture of the actual configuration is shown, where the beam lines are highlighted.

2.5.2 Design of the microscope

A brief overview of the design process and the major components of the microscope will be described in this section.

Starting from the already fixed components and their known dimensions and parameters, schemes of the setup were drawn in 2D using computer-aided design (Shark FX v5.0.0, Punch!Software LLC, USA). After checking for the proper distances of the components and requirements for sliders and holders, these schemes were then drawn in 3D (AutoDesk Inventor Pro 2011, Autodesk GmbH, München, Germany). Again these schematics were checked for the optimal dimensions and feasibility of construction. The design of the bottom part is described in the following.

2.5 Construction of an optical trapping setup for microrheology

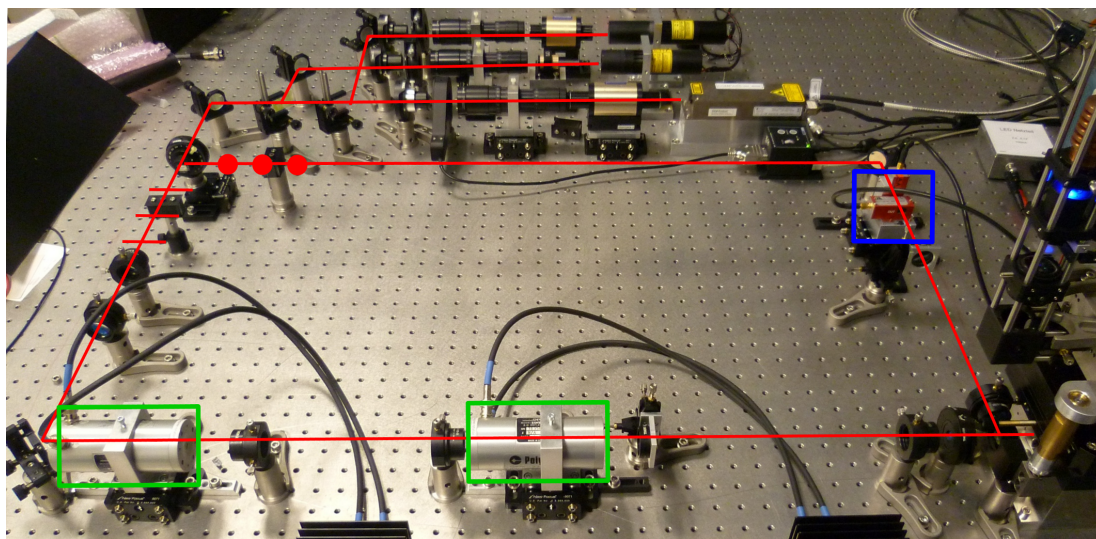


Figure 2.9: Beam steering optics of the setup - The image shows the realization of the schematic layout in figure 2.7 on a vibration-isolated optical table. The trapping lasers shown at the top are combined by dichroic mirrors and then split into two beam paths of parallel (lines) and perpendicular (dots) polarization with respect to the table. The direct beam can be deflected by a pair of EODs (green boxes), while the indirect beam goes through the AODs (blue box). Both beams are then recombined by another PBS and directed into the microscope on the right. During experiments, the beam-steering optics were covered by a box and the beam line was shielded with tubes to minimize air currents.

One of the first decisions made was which objective should be used for focusing the laser beam to form the optical trap. In this setup an oil-immersion, infinity-corrected alpha Plan-Apochromat objective (Carl Zeiss MicroImaging GmbH, Jena, Germany) is employed, with a magnification of 100x and a high numerical aperture of 1.46. With its very good field flattening and achromatic correction, it is especially suited for high-resolution microscopy including fluorescence and DIC, and it offers a transmittance of around 50% in the infrared regime, where the trapping lasers operate (65% @ 830 nm down to 50% @ 1064 nm; (37)).

The so called “infinity space”, the region between the objective and the tube lens (tube lens 25, Carl Zeiss) where the light travels in parallel wavetrains, allows the introduction of auxiliary components, such as DIC-prisms, polarizers or dichroic mirrors, with only a minimal effect on focus and aberration corrections. Despite what the name suggests, the distance between objective and tube lens should not exceed 100 mm, as recommended by the manufacturer, to avoid vignetting and a loss of image quality. This

2. OPTICAL TRAPPING

sets the limitation for the design of the microscopes chassis and the optical components, which are to be implemented.

The following components have to fit into the parallel optical path:

- a DIC-prism (PA 100x/1.46 III, Carl Zeiss),
- the dichroic mirror for coupling in the trapping laser (725 DCSPXR, Chroma Technology Corp., Bellows Falls, VT, USA),
- the dichroic mirror for reflecting the fluorescence illumination into the objective (HC 665 LP, AHF Analysentechnik AG, Tübingen, Germany),
- a 45°-turning mirror for directing the light parallel to the optical table towards the camera,
- a polarizer for DIC,
- emission filters for fluorescence and
- an IR filter to block the back-reflection of the trapping laser from the glass-water interface.

The height at which the trapping laser is coupled into the microscope was set to 75 mm, leaving enough space to place the beam steering optics on the optical table. The laser light is then reflected upwards through the DIC-prism. The prism is oriented parallel or perpendicular respectively to the trapping laser polarization. After that, the beam enters the objective.

Below this, the fluorescence laser can be coupled in at a height of 57 mm. A turning mirror then directs the light parallel to the table at a height of 37 mm through the subsequent flat optics towards the tube lens.

At the focal length of the tube lens (160 mm for Zeiss-optics) a CCD-camera (Cool-Snap EZ, Photometrics, Tucson, AZ, USA) is placed to image the sample.

The sliders that hold the dichroic mirrors in the chassis should be able to be removed reproducibly, without altering their position within the microscope each time. Therefore, most sliders were designed as shown in figure 2.10. A T-shaped layout with the holder in front and an arrester at the end was chosen. To fix the position, small rare-earth magnets were placed on the side, bottom and end of the slider. The

2.5 Construction of an optical trapping setup for microrheology



Figure 2.10: Microscope slider for a dichroic mirror - Example of a typical T-shaped microscope slider. The dichroic mirrors, with a size of $20 \times 20 \times 1$ mm, can be fixed in the holder at the front (this differs from slider to slider depending on its location in the chassis). The drilled holes at the sides hold the rare-earth magnets, whose counterparts are inside the chassis.

counterparts were placed inside the chassis, fixing the position in three dimensions very accurately.

On top of the chassis a custom-built manual xy-stage was placed, consisting of two parallel plates held together by pairs of strong rare-earth magnets at the corners with a slight offset from each other. The plates can be displaced with respect to each other by micrometer screws, while springs prevent any rotational movement. This allows coarse sample movement of ± 1 cm in the lateral direction. Above the manual stage, a piezostage (P561.3CD, $100 \mu\text{m}^3$, 0.8 nm resolution, Physik Instrumente GmbH, Karlsruhe, Germany) provides computer-controlled high-precision sample positioning in three dimensions. The sample holder is located inside the opening of the piezostage. It allows coarse adjustments of the sample height of ± 2.5 mm by ball bearings.

Since two objectives are used, the sample has to consist of two coverslips separated by doublestick tape (Scotch ATG tape 924, $50 \mu\text{m}$ thick, 3M, St. Paul, MN, USA).

The upper part of the microscope chassis includes the detection part and the illumination. The top part is also fabricated in a compact fashion from stainless steel. It rests on a tripod, which can be placed on top of the microscope's bottom part. The custom-built micrometer screws of the tripod allow precise adjustments of the upper part's height and the angular orientation. The detection part can also be moved with respect to the tripod for centering the condenser objective on the optical axis.

The condenser was chosen to be the same objective used for focusing the laser. This ensures similar properties of focusing and detecting the trap laser, and the detection benefits from the superior imaging properties compared to a standard condenser lens.

2. OPTICAL TRAPPING

Here, the infinity-space must contain the following optical elements:

- a DIC-prism,
- a dichroic mirror to couple in the illumination light (HC 665 LP, Semrock Inc., Rochester, NY, USA),
- a polarizing beam splitter “PBS3” (Artifex) to split up the two independently polarized laser traps,
- two dichroic mirrors to reflect the 980 nm and 830 nm lasers into separate detection paths (1000 DCLP, zq 830 RDC, both AHF Analysentechnik AG).

Beyond these optics, NIR-antireflection coated 50 mm achromatic doublets (AC254-050-B, Thorlabs, Newton, NJ, USA) image the back-focal-plane of the condenser objective onto Nd:YAG enhanced silicon quadrant photodiodes under a reverse bias voltage of 160 V (SPOT9-YAG, 10 mm diameter, OSI Optoelectronics, Hawthorne, CA, USA). The lens is placed at a $2f$ -distance from the objective’s BFP, resulting in a one-to-one image on the QPD at the same distance. A total of four different light paths allow simultaneous detection of several optical traps of differing wavelength and polarization. The imaging lens is mounted in a tube, which can be inserted into the chassis’ side ports. With a locking ring their axial position as well as their rotational orientation can be fixed relative to the microscope. This allows the accurate positioning of the QPDs. A flexure adjustment plate (CP1XY, Thorlabs) is used for lateral centering of the QPD with respect to the BFP-image. The QPD housing bears a slot for 1/2” line filters and can be attached to the flexure plate.

A high-power blue LED (LuxeonStar LXHL-MRRD, 1 W, 455 nm, Quadica Developments Inc., Brantford, Canada) is used for Köhler illumination of the sample (35). The illumination optics are mounted into a standard 30 mm cage system (Thorlabs) and can be inserted into the left side port of the microscope. A detailed description of the illumination light path is given in the appendix C.4.2.

In figure 2.11 the CAD drawing of the housing is shown together with an image of the realized setup.

The alignment procedure for the whole setup is described in chapter C of the appendix.

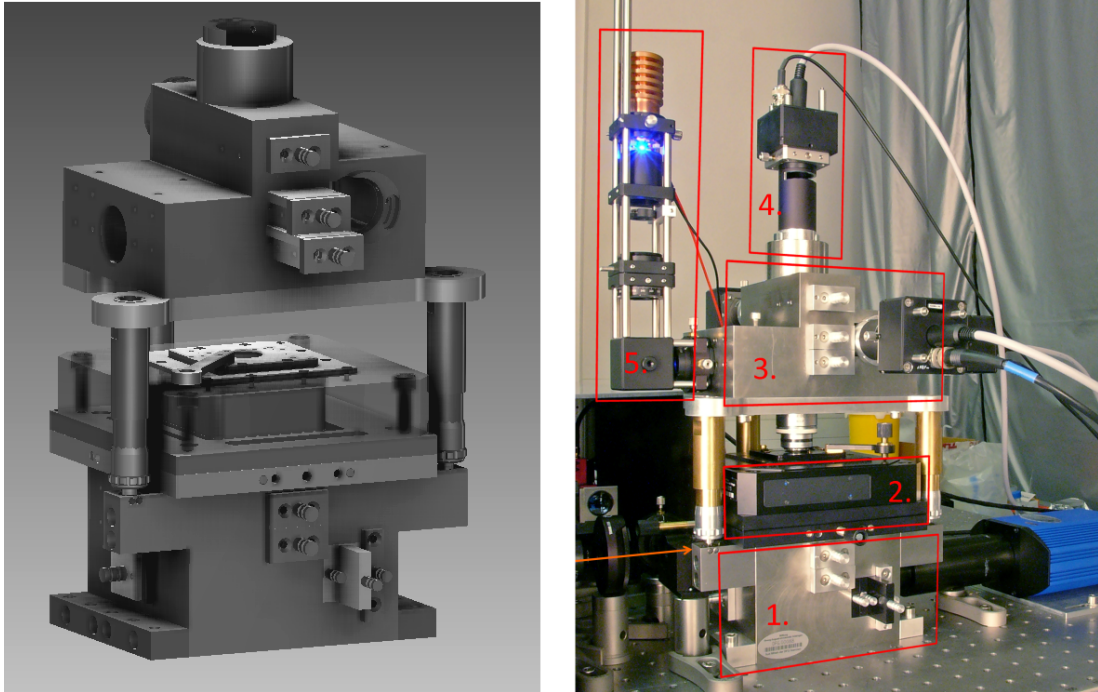


Figure 2.11: Design and realization of the microscope chassis - On the left, the CAD drawing of the chassis is shown, incorporating all sliders and holders. The image on the right shows the realization, where all optical elements have already been aligned. The trapping lasers enter the chassis from the left (orange arrow), the camera is located to the right. The bottom part is highlighted in box (1). On top sits the manual xy- and the piezostage with the sample holder (2), which occlude the objective. The detection part with the condenser objective (3) lies on a tripod. The QPDs stick out of the sideports (4) and the illumination is located at the left side (5).

2.5.3 Data acquisition

Custom-built analog electronics are used to obtain the QPD-signals. The voltages are amplified by low-noise preamplifiers and further amplified and combined by differential amplifiers, yielding signals proportional to the x- and y-positions of the particle in the center of the trap. To account for aliasing, the voltage signals are filtered at the Nyquist-frequency by a custom-made 10th-order Butterworth filter.

The displacement signals are sampled with an FPGA A/D board (NI PXI-7833R, National Instruments, Austin, TX, USA) and processed by custom-written LabVIEW data acquisition software (National Instruments), which is detailed in the diploma thesis of Christoph Pieper (38). The recorded position fluctuation data is processed off-line

2. OPTICAL TRAPPING

in MATLAB. A toolbox for analyzing microrheology data has been written by Felix Zörgiebel and is described in his diploma thesis (39). Its functionality has been further extended in this work (see appendix B).

2.6 Characterization of the microrheology setup

2.6.1 Quantifying noise

When recording position fluctuations, various kinds of environmental noise add to the signal, possibly masking the sought-after characteristics (40). To test the performance of the setup, the QPD signal was recorded for about one hour for two cases: with a $1\ \mu\text{m}$ bead trapped in water and for the trap without a bead. The $1064\ \text{nm}$ laser going through the EODs was used for these measurements. About $3.6 \cdot 10^7$ data points were collected at a sampling frequency of $20\ \text{kHz}$. Figure 2.12 shows the PSDs of both measurements averaged in 100 logarithmically spaced bins. The corner frequency for the trapped bead lies around $1\ \text{kHz}$, above which the spectrum decays with the characteristic power-law exponent of -2 for free diffusion (see equation 2.7 for $\omega \gg \omega_c$). At intermediate frequencies, the plateau indicates the confinement of the bead in the trap. At frequencies below $1\ \text{Hz}$, noise adds to the power spectrum with a typical $1/f$ -characteristic. For comparison, the spectrum without a bead is displayed. The amplitude is several orders of magnitude lower at high frequencies, while below $1\ \text{Hz}$ both spectra display the same noise characteristic.

The noise at low frequencies stems mainly from beam pointing instability of the laser, as indicated by the dotted line in figure 2.12. Here, the laser was centered onto the QPD directly after the first half-wave plate without going through the beam-steering optics and the microscope. The position fluctuations of the laser spot were tracked with the same parameters as above. As can be seen, the power spectrum drastically increases below $1\ \text{Hz}$. The noise performance of the setup at this point is therefore mainly limited by the trapping laser. One way to optimize the beam pointing stability would be the implementation of an active feedback mechanism, as for example described in (41).

Another source of noise is mechanical drift of the sample. To quantify this influence, the laser was positioned over a $1\ \mu\text{m}$ bead fixed to the coverslip and the deflection of the laser over a time interval of one hour was monitored with the QPD. The magnitude

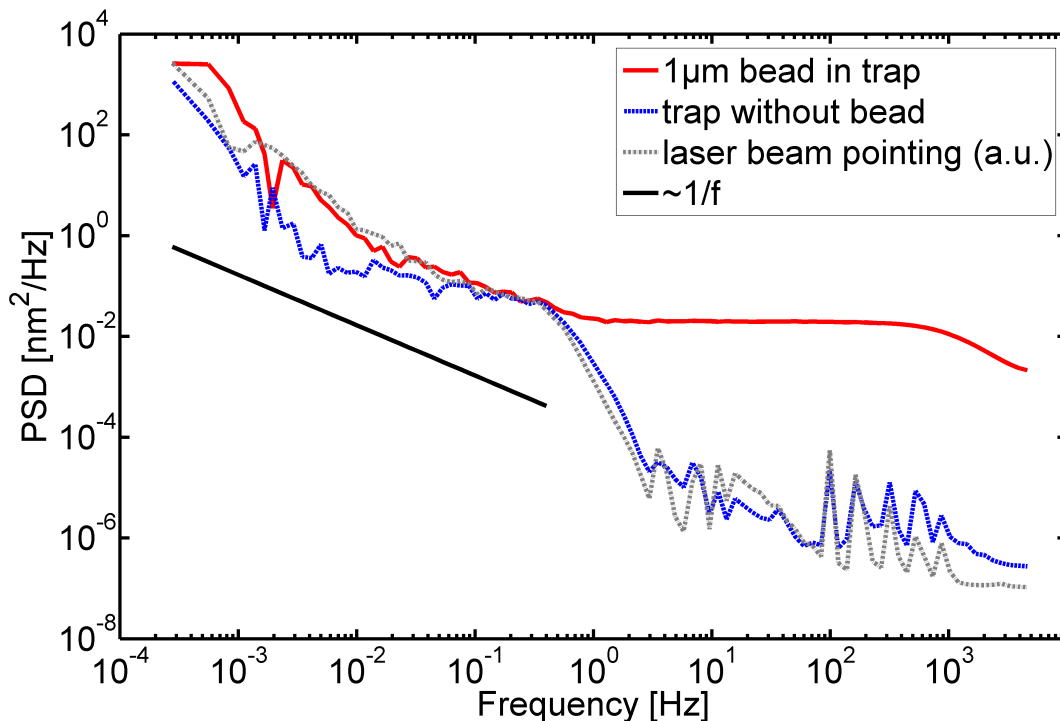


Figure 2.12: Noise measurement - Power spectral density for a $1\ \mu\text{m}$ bead in water measured over 1 hour. The spectrum without a bead is plotted for comparison. The dashed line indicates the beam pointing instability of the laser, displaying a typical $1/f$ characteristic (solid bar).

of this creep is depicted in figure 2.13. A linear fit to the data revealed a sample drift of about $0.7\ \text{nm}/\text{min}$.

2.6.2 Performance of AOD and EOD beam steering

In order to test the alignment and performance of the deflectors, a voltage ramp was applied to them to scan the laser focus over a $1\ \mu\text{m}$ bead, which was fixed on a coverslip while recording the x- and y-signal of the QPD. The signal is then plotted versus the applied ramp signal. The result for the y-signal of the corresponding EOD is shown in figure 2.14a. One can see a part of the typical S-shaped QPD response function, here limited by the maximum deflection of the EOD. The horizontal line shows the background, which was recorded while scanning the laser without a bead in focus. The signal is almost zero, showing the proper imaging of the EOD's deflection plane onto

2. OPTICAL TRAPPING

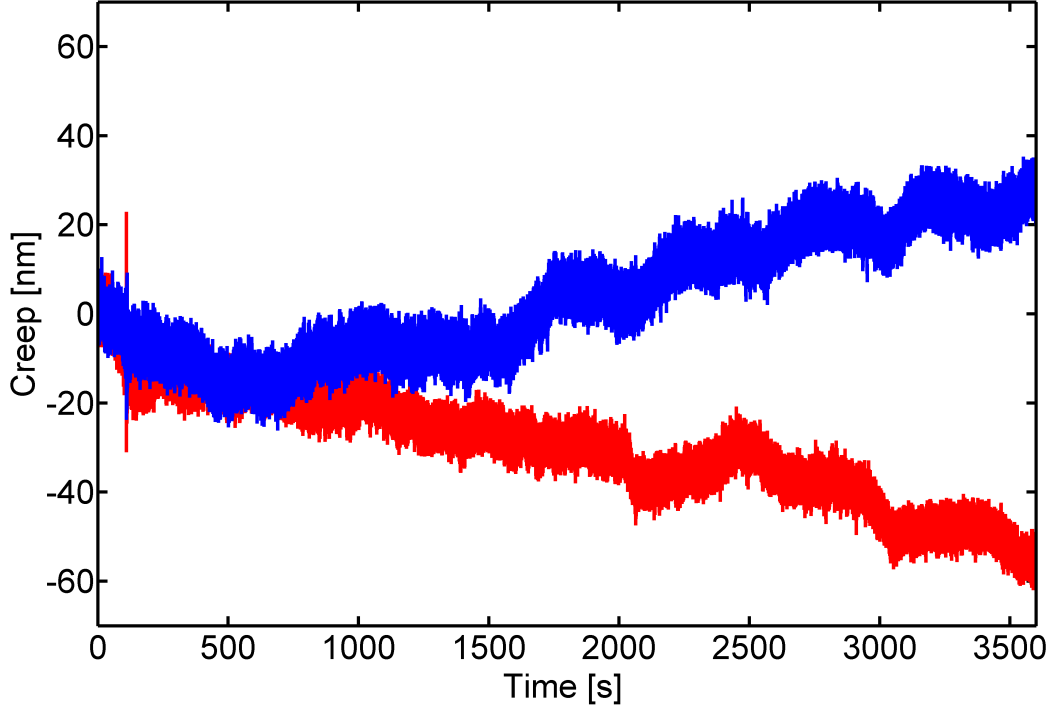


Figure 2.13: Measurement of sample creep - Lateral positions over time of a $1\ \mu\text{m}$ silica bead fixed to the coverslip. The position was measured by placing the bead in the center of the laser focus and record the QPD signal at a sampling rate of 1 kHz for one hour. The sample drifts at about $0.7\ \text{nm}/\text{min}$, based on a linear fit to the y-signal (red).

the QPD. It is important to note, that the deflection of the EOD hardly depends on the laser wavelength, since the reflective index dispersion is almost constant in the accessible range. We confirmed this for all three employed wavelengths by applying a sine-wave to the EOD driver, such that the bead can follow the trap. Using a custom-built feature-finding algorithm (LabVIEW) the bead's trajectory was extracted and fitted numerically. Via the known camera calibration, the amplitude of the displacement in the focal plane can be linked to the amplitude of the voltage applied to the driver. We obtained a calibration factor of $0.21\ \mu\text{m}/\text{V}$, with a deviation of less than 4% between the three wavelengths.

In figure 2.14b the response curve for scanning the bead with the AOD using the same scanning parameters as above is plotted. The response function appears noisier, most likely due to interference between the propagating acoustic wave in the crystal

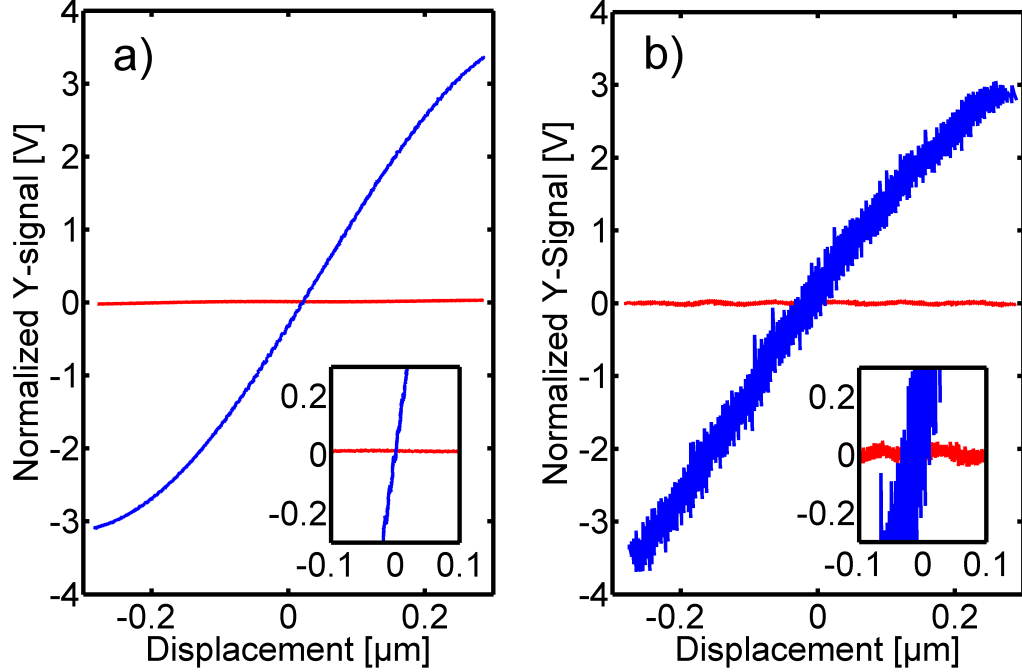


Figure 2.14: QPD response curves - a) The QPD response curve obtained by scanning the laser focus over a $1\ \mu\text{m}$ bead fixed to the coverslip. The amplitude was $0.3\ \mu\text{m}$, the upper limit of the EOD deflection. The horizontal line shows the background, which was recorded while scanning the laser without a bead in focus. The inset shows the linear regime in the center of the S-shaped curve. b) The same for the AOD. The data is noisier showing characteristic spikes, due to interference effects inside the crystal.

and unwanted backreflections at its end, as was also observed in (19).

In an active microrheology experiment (section 3.4.1), the amplitude and phase of the displacement response with respect to the driving signal are measured. This is altered by the characteristic time delay of all instruments in the setup. To account for this, the amplitude and phase delay are measured by oscillating the drive laser with constant amplitude and different frequencies over a probe particle fixed to the coverslip (see also (42)). The particle does not move in response to the oscillations of the driving laser, and the output of the QPD is fed into the lock-in amplifier. Amplitude and phase as a function of frequency are recorded. In figure 2.15 the response function of the setup is plotted over frequency. At lower frequencies the amplitude decreases, because of capacitive coupling of the lock-in amplifier's input signal channel (figure 2.15a).

2. OPTICAL TRAPPING

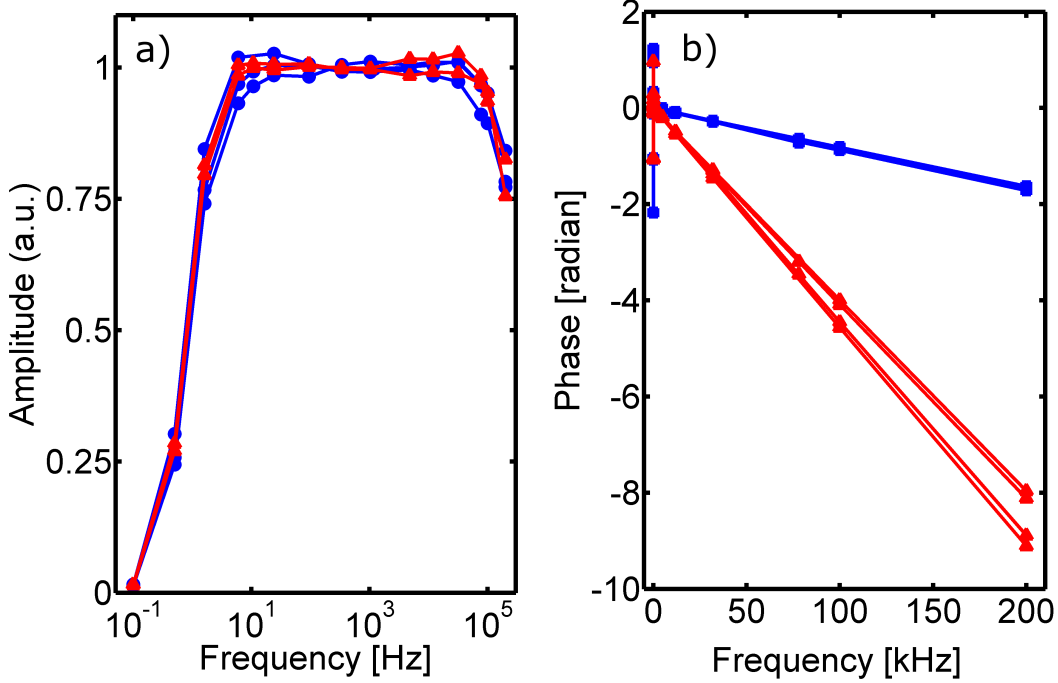


Figure 2.15: System response - System responses of AODs (red) and EODs (blue) obtained by measuring the diffraction of the oscillating drive laser by a bead attached to the coverslip. a) The amplitude of the system response decays at low frequencies due to ac coupling of the signal input of the lock-in amplifier. At high frequencies around 100 kHz, a drop-off of the amplitude is observed due to bandwidth limitations of the electronics. b) The phase delay of the system response is linear with the applied frequency. The delay is higher for the AODs.

This also leads to a significant phase delay in this regime. At higher frequencies the amplitude is mainly constant, with a slight drop-off around 100 kHz, which is close to the bandwidth-limit of the electronics.

The phase delay increases with the oscillation frequency (figure 2.15b). For the EODs this change is linear and quite small. For the AODs a significant increase is observable. This is due to the finite sound velocity of the ultrasonic wave traveling through the AOD crystal. The time it takes until the sound wave reaches the laser position inside the crystal leads to a frequency dependent phase delay. Also, beam distortions occur when the wavelength becomes comparable to the beam diameter. This effect introduces the artifacts observed at high frequencies (42). For the EOD

2.6 Characterization of the microrheology setup

these effects do not occur, since here the beam deflection is introduced by a change in the electric field applied to the crystal, which happens on a much faster timescale. It is important to note, that in an active measurement only the driving laser is affected, while the actual response measurement is performed with the stationary probe laser.

2. OPTICAL TRAPPING

3

Microrheology

3.1 Introduction

If we assume a rigid spherical bead embedded in an incompressible, continuous viscous fluid, it is possible to solve the Navier-Stokes equation in the limit of small Reynolds numbers. The drag force \vec{F} on the particle is related to its velocity \vec{v} by:

$$\vec{F} = \gamma\vec{v} = 6\pi\eta r\vec{v}, \quad (3.1)$$

with the drag coefficient γ , which includes the bead's radius r and the dynamic viscosity η . This is the so-called Stokes' law.

Most biological materials are much more complex, since they not only show fluid-like (viscous) but also solid-like (elastic) behavior. They are “viscoelastic”. Their response to external forces in general depends on the magnitude of the force and also on the timescale. To extract material properties, like the complex shear modulus $G^*(\omega)$, one can examine small embedded beads, since their motion is linked to their environment.

3.2 The fluctuation-dissipation theorem and linear response

Already in the 1930s, Lars Onsager had hypothesized, that the macroscopic relaxation of a system back to equilibrium has the same physical origin as the relaxation of spontaneous fluctuations about equilibrium.

If a general relationship between the relaxation of a macroscopic observable and its fluctuations around equilibrium is to be derived, one has to look at the microscopic evolution of the system. This leads to the fluctuations-dissipation theorem (FDT). The

3. MICRORHEOLOGY

following discussion is based mainly on the lecture notes of F. C. MacKintosh for a course on statistical mechanics of soft matter (43).

If a perturbation is applied to a system in the past, it will be taken to an equilibrium state described by the Hamiltonian H' at time $t = 0$. The perturbing field is then turned off and the systems relaxes back to the equilibrium state H . (The examination of this problem is identical to the perturbation at $t = 0$ and subsequent relaxation to a new equilibrium state.) The relaxation of interest shall be described by a macroscopic observable A . If the perturbing field f is sufficiently small, the situation can be described by linear response theory. In this case the Hamiltonian H obeys:

$$H' = H + \Delta H = H - fA. \quad (3.2)$$

After the field f is turned off, the initial macrostate $\langle A \rangle$ of the system evolves according to the Hamiltonian and a time-evolution operator. The system's time evolution can be expanded in a Volterra series and, keeping only the leading linear term, some calculation (43) leads to the average deviation of A from its equilibrium value at temperature T :

$$\Delta A(t) \cong \frac{1}{k_B T} f \langle \delta A(0) \delta A(t) \rangle_0, \quad (3.3)$$

where $\Delta A(t) = A(t) - \langle A(t) \rangle_0$ and $\langle \rangle_0$ refers to an ensemble average in the unperturbed system, with k_B as the Boltzmann constant. The average $\Delta A(t)$ is the mean over an ensemble of systems with the same perturbation. The expression 3.3 is one formulation of the fluctuation-dissipation theorem, relating the macroscopic evolution of a system driven out of equilibrium to the fluctuations of the system about equilibrium.

The general form of a linear response to a time-dependent perturbation is

$$\Delta A(t) = \int_{-\infty}^{\infty} \chi(t, t') f(t') dt', \quad (3.4)$$

with the response function χ given by

$$\chi(t, t') = \begin{cases} \chi(t - t') & \text{for } t > t' \\ 0 & \text{otherwise} \end{cases}. \quad (3.5)$$

Here, χ is a property of the equilibrium system and does not dependent on f . Thus, it depends only on the time interval between t and t' . Causality implies that the response function is zero for all $t' > t$.

If, in general, the linear coefficient of the perturbation f in equation 3.2 is another observable B , the linear response of the observable A to such a perturbation is given by the response function $\chi_{AB}(t - t')$. Here, f and B are conjugate thermodynamic variables. Analogous to the steps before one can find:

$$\Delta A(t) \cong \frac{1}{k_B T} f \langle \delta B(0) \delta A(t) \rangle_0, \quad (3.6)$$

In this way one can describe, for example, the response of a bead in a fluid to a perturbing external force field f . The system will develop a drift velocity v . In this case the thermodynamically conjugate variable to f is the displacement x of the particle in the direction of the force.

3.3 The shear modulus

In the rheology of complex, viscoelastic media, the behavior is in general described by the shear modulus $G(t)$. If a shear strain $\epsilon(t)$ is applied to the material, it responds with a time dependent shear stress $\sigma(t)$ opposing the deformation. Both are related by the shear modulus:

$$\sigma(t) = \int_{-\infty}^t G(t - t') \dot{\epsilon}(t') dt', \quad (3.7)$$

with the time derivative $\dot{\epsilon}(t')$ of the shear strain. The Laplace transform of the shear modulus

$$G^*(\omega) = i\omega \int_0^{\infty} G(t) e^{-i\omega t} dt \quad (3.8)$$

describes the linear response of the medium to a small, oscillating stress

$$\sigma(\omega) = G^*(\omega) \epsilon(\omega). \quad (3.9)$$

The real part $G'(\omega)$ is called the storage modulus and describes the in-phase, i.e. the elastic, response of the medium, while the imaginary part $G''(\omega)$ is termed the loss modulus and describes the viscous, dissipative response. Both parts are related by the Kramers-Kronig relations.

A particle confined in a viscoelastic medium and subject to an oscillating force f will induce a shear stress field $\sigma \propto f$. This is related to the shear strain field, which is proportional to the bead's displacement, $\epsilon \propto \Delta x$. By applying a known force and measuring the displacement of the particle, it is possible to extract the shear modulus. In the following section it will be shown how this can be done using a bead in an optical trap, by using the linear response described in section 3.2.

3. MICRORHEOLOGY

3.4 A particle confined by a harmonic potential

In microrheology experiments using optical traps, a spherical particle is embedded in a viscoelastic fluid and subject to the potential generated by the trap. The potential can be considered as “harmonic”, i.e. proportional to a spring constant κ , with $U = \frac{1}{2}\kappa x^2$. The equation of motion of the bead can be described by a Langevin equation:

$$m\ddot{x}(t) + \gamma\dot{x}(t) + \kappa x(t) - f(t) - \zeta(t) = 0, \quad (3.10)$$

with the bead’s mass m , the friction coefficient γ , an external force f and the thermal force ζ . Taking the ensemble average, $\langle \zeta \rangle = 0$, and applying a Fourier transform, one gets

$$x(\omega) = \frac{1}{\kappa - m\omega^2 - i\gamma\omega} f(\omega) = \chi(\omega) f(\omega). \quad (3.11)$$

with $\chi = 1/(\kappa - m\omega^2 - i\gamma\omega)$. In the following discussion the inertial term including the mass of the bead is neglected. This is safe for motions of the probe particle up to frequencies where the inertial decay length is larger in magnitude than the object’s size (44).

There are two ways of using equation 3.11 to extract the shear modulus. A so called “active” and a “passive” method, which are described in the following subsections.

3.4.1 Active microrheology

If a known force is applied to a probe coupled to the medium and the displacement is measured, equation 3.11 yields the material’s response function. This can be related to the shear modulus via equation 3.9, assuming that the stress is linear in force and the strain is proportional to the probe’s displacement, as discussed at the end of section 3.3. This is the approach used in classical large-scale rheometers, where for example a cone applies a shear stress to the sample and the strain is measured with an opposing plate.

This can also be performed using an optical trap (42). An external driving force $f(t) = \kappa_1(Ae^{-i\omega t} - x(t))$ is applied to the particle by an optical trap of trap stiffness κ_1 oscillating with a frequency ω and amplitude A . The frequency-dependent displacement response, $x(t) = x(\omega)e^{-i\omega t}$, is measured by a stationary optical trap of stiffness κ_2 . Inserting these variables in equation 3.10 yields equation 3.11. Before the response function can be related to the shear modulus, one subtlety has to be dealt with. The

3.4 A particle confined by a harmonic potential

forces of both optical traps are included in the response function. So, an apparent response function

$$\tilde{\chi}(\omega) = \frac{1}{\kappa_1 + \kappa_2 - i\omega\gamma} \quad (3.12)$$

is obtained. The true material's response function $\chi(\omega) = \frac{1}{-i\omega\gamma(\omega)}$ can be evaluated as (45)

$$\chi(\omega) = \frac{\tilde{\chi}(\omega)}{1 - (\kappa_1 + \kappa_2)\tilde{\chi}(\omega)}. \quad (3.13)$$

Solving the general stress-strain relation under certain boundary conditions yields an effective compliance for the bead's displacement (44):

$$\chi(\omega \rightarrow 0) = \frac{1}{6\pi r G} \left[1 + \frac{\nu - 0.5}{2(\nu - 1)} \right], \quad (3.14)$$

with the bead radius r and the Poisson ratio ν . For a polymer network in a solvent it can be shown that above a certain cross-over frequency, which depends on the ratio of the bead radius and the mesh size, the bead moves as an inclusion in an incompressible continuum viscoelastic medium (44). Hence, $\nu = 1/2$ and one obtains

$$x(\omega) = \frac{1}{6\pi r G} F(\omega) = \chi(\omega) F(\omega), \quad (3.15)$$

which is a generalized version of the Stokes' law 3.1. In practice, an optical trap is oscillated with the reference signal of a lock-in amplifier (Model 7280, Signal Recovery, Oak Ridge, TN, USA), resulting in a force $F(\omega)$, while the displacement of the bead is obtained as the complex quantity $x(\omega)$ by feeding the signal from the quadrant-photodiode back into the lock-in amplifier (see also 2.6.2). This method is called "active microrheology" (AMR).

3.4.2 Passive microrheology

A different method to obtain the complex shear modulus makes use of the fluctuation-dissipation theorem as discussed in section 3.2, since equation 3.11 suggests a linear response. In the time domain this can indeed be written as the convolution:

$$x(t) = \int \chi(t - t') f(t') dt', \quad (3.16)$$

which is analogous to equation 3.4. Before the FDT can be applied here, a subtlety has to be considered. Only for $t > 0$ the response function is non-zero, while the convolution

3. MICRORHEOLOGY

given above is a symmetric function. The function $\chi(t)$ can be decomposed into an even and odd part:

$$\chi(t) = \chi_E(t) + \chi_O(t), \quad (3.17)$$

with $\chi_E(t) = \frac{1}{2}(\chi(t) + \chi(-t))$ and $\chi_O(t) = \frac{1}{2}(\chi(t) - \chi(-t))$. The Fourier transform of the even part is real and symmetric and denoted by $\chi'(\omega)$. The odd part is purely imaginary and odd in ω and is referred to as $i\chi''(\omega)$. Both χ' and χ'' are real functions and

$$\chi(\omega) = \chi'(\omega) + i\chi''(\omega). \quad (3.18)$$

Using the FDT as given in equation 3.6, one obtains:

$$\chi(\omega) = \frac{i\omega}{k_B T} \langle x(\omega)x(-\omega) \rangle. \quad (3.19)$$

The imaginary part is defined for all t and can be written as:

$$\chi''(\omega) = \frac{\omega}{2k_B T} \langle x(\omega)x(\omega) \rangle = \frac{\omega}{2k_B T} \langle |x(\omega)|^2 \rangle. \quad (3.20)$$

This is another way of writing the fluctuation-dissipation theorem, which involves the power-spectral density $C(\omega) = \langle |x(\omega)|^2 \rangle$ of the equilibrium fluctuations. The real part of the complex response function χ can be obtained from the Kramers-Kronig relations:

$$\chi'(\omega) = \frac{1}{\pi} P \int_{-\infty}^{\infty} \frac{\chi''(\omega')}{\omega' - \omega} d\omega', \quad (3.21)$$

where P denotes the Cauchy principal value.¹

The complex response function $\chi(\omega)$ can thus be calculated from the power-spectral density, and, by using the generalized Stokes' law of equation 3.15, the complex shear modulus can be obtained.

In the experiments, the motion of a probe particle is measured using back-focal-plane interferometry. By applying a Fourier transform to the autocorrelation of the position fluctuations, the PSD can be calculated, as stated by the Wiener-Khinchin theorem (23). This method is called “passive microrheology” (PMR), since no active force is applied to the bead as in AMR (section 3.4.1). Instead the “known” thermal force acting on the bead is used to extract the material properties.²

¹In practice this leads to a cut-off at high frequencies, since the integration interval is limited by the frequency bandwidth of the acquisition devices (44).

²Since only one bead has been considered in this section, the two methods will be referred to as one-particle active (1AMR) and one-particle passive microrheology (1PMR) in the following. This is to distinguish them from the two-particle methods introduced in section 3.5.

3.5 Two-particle microrheology

The methods discussed so far only involved a single bead serving as a local probe to determine the viscoelastic properties of the surrounding. But Crocker et al. showed, that these one-particle methods can provide qualitatively different results than conventional bulk rheology (46). In the same publication they present a two-particle method which gives results closer to the bulk properties. Using an analogy from electrostatics, Levine and Lubensky showed in (47, 48), that a single bead indeed only probes the local environment, which might be disturbed by the presence of the bead itself. They also explain how this can be overcome using two beads. If one bead is subject to a force, another bead at a separation large compared to the bead's radius will follow the displacement field produced by the first bead. This does not depend on the local environment of the beads. Therefore, investigating the cross-correlated motion of two beads can yield the material properties of the inter-bead space, which reflect the bulk properties obtained by macrorheology (45, 49).

Two-particle microrheology can again be performed in an active and passive manner, as described in 3.4.1 and 3.4.2. An overview can be found in (42). Here, one particle is located at the position $(u_x^{(1)}, u_y^{(1)})$ and a second at $(u_x^{(2)}, u_y^{(2)})$. The line connecting the beads shall be the x-coordinate, corresponding to parallel (\parallel), and y will denote the perpendicular direction (\perp) to the line connecting the beads. The linear response in this case is described by two independent parameters $\chi_{\parallel}(\omega)$ and $\chi_{\perp}(\omega)$. This corresponds to:

$$u_x^{(1,2)} = \chi_{\parallel}(\omega) F_x^{(2,1)}(\omega), \quad (3.22)$$

$$u_y^{(1,2)} = \chi_{\perp}(\omega) F_y^{(2,1)}(\omega). \quad (3.23)$$

Here, the displacement of one bead is related to the force acting on the other bead, as indicated by the superscripts.

The passive measurement, referred to as 2PMR, again uses the FDT to relate the PSD to the response functions. Here, the power spectra are computed from the cross-correlations

$$C_{\parallel}(\omega) = \int_{-\infty}^{\infty} \langle u_x^{(1)}(t) u_x^{(2)}(0) \rangle e^{i\omega t} dt, \quad (3.24)$$

$$C_{\perp}(\omega) = \int_{-\infty}^{\infty} \langle u_y^{(1)}(t) u_y^{(2)}(0) \rangle e^{i\omega t} dt, \quad (3.25)$$

3. MICRORHEOLOGY

which are related to the imaginary part of the response function by equation 3.20.

In the active measurement (2AMR) an oscillating driving force is applied to one bead, while the displacement of the other bead is measured.

For both methods the influence of the trapping potential has to be corrected for, to obtain the material response. This is more difficult due to the presence of two traps. Some calculations (45) lead to the lengthy expression:

$$\chi_{\parallel,\perp} = \frac{\tilde{\chi}_{\parallel,\perp}}{1 - \kappa_1 \tilde{\chi}_{\parallel,\perp}^{(1)} - \kappa_2 \tilde{\chi}_{\parallel,\perp}^{(2)} + \kappa_1 \kappa_2 \tilde{\chi}_{\parallel,\perp}^{(1)} \tilde{\chi}_{\parallel,\perp}^{(2)} - \kappa_1 \kappa_2 (\tilde{\chi}_{\parallel,\perp})^2}, \quad (3.26)$$

with the apparent single-particle response functions $\tilde{\chi}_{\parallel,\perp}^{(1,2)}$ and the apparent inter-particle response functions $\tilde{\chi}_{\parallel,\perp}$.

The shear modulus is in the two-particle case related to the response functions by a generalization of the Oseen tensor (47, 48)

$$\chi_{\parallel} = \frac{1}{4\pi a G(\omega)}, \quad (3.27)$$

$$\chi_{\perp} = \frac{1}{8\pi a G(\omega)}, \quad (3.28)$$

where a is the distance between the two beads.

3.6 Microrheology measurements in water

In this section, active and passive one-particle microrheology measurements are shown. The experiments were performed on the new microrheology setup described in chapter 2. As a test sample water was chosen, as a simple viscous fluid with a purely imaginary shear modulus of $G(\omega) = -i\eta\omega$. Plain silica beads with a diameter of $1\ \mu\text{m}$ were trapped at a distance of $10\ \mu\text{m}$ from the coverslip. For the active measurement the 980 nm laser was oscillated by the EOD while the 1064 nm laser served as the probe laser (see section 2.5). A frequency sweep was performed up to 200 kHz and, using the generalized Stokes-Einstein equation 3.15, the complex shear modulus was calculated.

For the passive measurement the drive laser was switched off and the pure Brownian fluctuations were monitored with the probe laser. In figure 3.1 the results from both methods are shown. The theoretical value for the imaginary part of the complex shear modulus is plotted as a dashed line. Both active and passive measurements agree well with the expected curve over the whole frequency bandwidth. The elastic part of

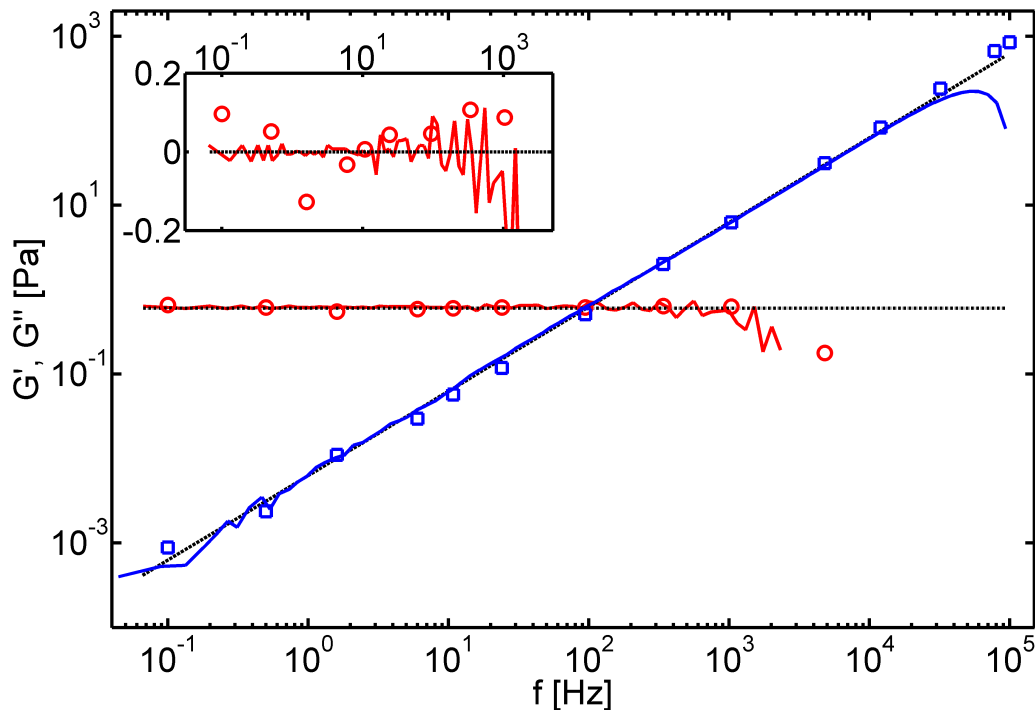


Figure 3.1: Shear modulus for water measured with the new microrheology setup - One-particle active and passive microrheology was performed in water. Real (red dots and line) and imaginary part (blue squares and line) of the complex shear modulus are plotted versus frequency. The theoretical curve for water is shown for comparison. The horizontal dotted line at ≈ 0.6 Pa indicates the elastic modulus as calculated from the trap stiffness, which was $\kappa = 5.7 \cdot 10^{-6}$ N/m. The inset shows the real part after correcting for the trap influence. The data is distributed around zero.

the shear modulus shows the influence of the optical trap at lower frequencies. It is constant and proportional to the trap stiffness κ :

$$G'_{trap} = \frac{\kappa}{6\pi r}, \quad (3.29)$$

with r the radius of the bead (dash-dotted line in figure 3.1). After subtracting this contribution, the real part of the shear modulus vanishes as expected for a purely viscous fluid (see inset of figure 3.1).

3. MICRORHEOLOGY

4

Composite networks

Understanding the mechanical properties of cells and their cytoskeleton remains challenging due to the heterogeneous and highly dynamic structure. Top-down approaches targeting single cells with optical tweezers or optical stretchers have recently been used to get a general overview of the cell's mechanical properties (50, 51, 52).

Investigating model systems in a bottom-up *in vitro* experiment addresses the problem from the side of the system's constituents. Reconstituted networks of the basic components can give a better understanding of their underlying mechanical properties. By slowly increasing the complexity of the model system while carefully measuring its properties at each step, one can try to build a minimal model for the cytoskeleton exhibiting similar characteristics compared to *in vivo* networks. So far, such models have been constructed using networks of F-actin and have been shown to reproduce nonlinear viscoelastic properties similar to those exhibited by cells (53, 54, 55). Cross-linked and prestressed networks have been investigated (54, 56) and in reference (57) a nonequilibrium network with myosin II motors was shown to exhibit contractile and adaptational properties similar to cytoskeletal networks.

The next steps in these approaches will be to include microtubules and intermediate filaments into the reconstituted networks. Rodriguez et al. proposed regulatory and structural interactions between microtubules and F-actin, which comprise several mechanochemical activity modules (58). Brangwynne and coworkers have shown the mechanical coupling of microtubules to the surrounding cytoskeletal network *in vivo* (59). The first microrheology measurements on microtubule and microtubule-actin composite network have been performed by Pelletier et al. (60) using video microrhe-

4. COMPOSITE NETWORKS

ology. For the composite network they observed a viscoelastic behavior between that of pure F-actin and microtubules respectively. Furthermore, they found evidence for a local compressibility introduced by the addition of microtubules to the F-actin network. Recently, Lin et al. have investigated the effect of introducing a small concentration of microtubules into a network of cross-linked F-actin, which led to a qualitative change in its nonlinear elastic properties (61). This work was accompanied by a theoretical publication by Bai et al. (62), who used a finite-element model to study the effect of adding a low density of rigid filaments to a network of softer semiflexible filaments, with respect to the affine to non-affine transitions of these networks.

As can be seen from the aforementioned publications, the mechanical properties of composite networks show remarkably distinct features compared to networks consisting only of one constituent. Different mechanical properties that are not found in simpler types of materials can emerge and can add new facets to the picture of cytoskeletal networks.

The following section 4.1 will introduce some of the major components of the cytoskeleton that this work focuses on: the microtubules, filamentous actin (F-actin) and motor proteins. An introduction into the “Mechanics of motor proteins and the cytoskeleton” is given in the book by Howard (63) on which this section is based.

In section 4.2, high-bandwidth microrheological measurements in a variety of model systems are described. Simple microtubule networks are described in subsection 4.2.1, a nonequilibrium system of microtubules together with motor proteins in 4.2.2, composite networks consisting of microtubules and F-actin with and without cross-linkers in 4.2.3 and 4.2.4, and finally a nonequilibrium system involving microtubules and F-actin as well as microtubule-associated motor proteins in 4.2.5.¹

¹All measurements described in this chapter were performed using the existing microrheology setup (see for example (22) for details), since the construction of the new setup was not yet finished.

4.1 Biopolymers and motor proteins

4.1.1 Microtubules

Microtubules are hollow cylindrical structures with an outer diameter of 25 nm, an inner diameter of about 18 nm and lengths of up to several tens of micrometers. They form polymers of $\alpha\beta$ -tubulin heterodimers, which are globular proteins with a mass of about 55 kDa. The α - and β -subunits have a similar atomic structure and are joined together by a noncovalent bond. Each subunit contains a binding site for the nucleotides Guanosine-5'-triphosphate (GTP), Guanosine diphosphate (GDP) and Mg^{2+} ions, which regulate polymerization and depolymerization. The dimers associate in a head-to-tail fashion and form a protofilament. These polymerize laterally to form a sheet that closes to the final tube-like structure. A small offset between neighboring protofilaments gives rise to a helical structure consisting of typically 13 protofilaments. This is shown in figure 4.1.

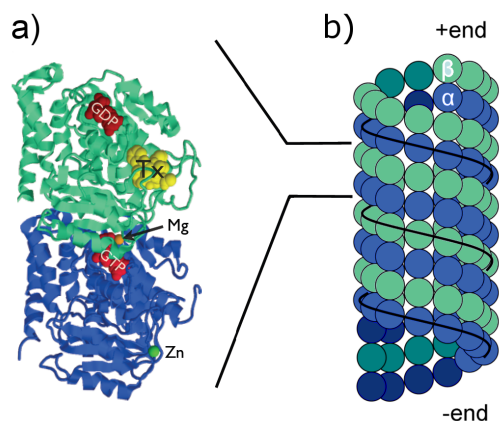


Figure 4.1: Microtubule structure - a) Protein structure of an $\alpha\beta$ -tubulin heterodimer, with MgGTP at α -subunit and GDP at β -subunit. The molecule shown in yellow is paclitaxel, used to stabilize the microtubule. Zinc (green) is employed to induce tubulin sheets imaged by X-ray crystallography (64). b) The dimers form protofilaments, that associate with a small shift. After 13 filaments the total offset equals the length of 3 monomers, resulting in the 3-start helix. The polarity arises from the asymmetry of the dimers. GTP is only hydrolyzed at the β -subunit, which therefore is the fast-growing (plus-)end. (Figure adopted from (39).)

The coexistence of polymerization and depolymerization is referred to as the “dynamic instability” of microtubules, and the filaments can switch between phases of growth and shrinkage. The transitions between both phases are termed “catastrophe” and “rescue” respectively. A different behavior involves a net growth of the microtubule at one end balanced by a shrinkage at the other, so called “treadmilling”. A detailed model of these dynamical properties from the experimental evidence so far is

4. COMPOSITE NETWORKS

given in (63). The regulating mechanisms *in vivo* and the precise chemical cycle are still poorly understood. A review about recent advances in this field is given by Jordan and Wilson (65). This study mainly deals with microtubule targeting anticancer drugs. A specific substance also employed in this work is paclitaxel, a drug belonging to the group of taxanes, extracted from the Pacific Yew tree, *Taxus brevifolia*.¹ Paclitaxel binds to and stabilizes microtubules, making it a mitotic inhibitor used in chemotherapy. The binding site of paclitaxel is known from electron crystallography to be in the beta-subunit. It is supposed to induce a conformational change in the tubulin, thereby increasing the affinity for the neighboring subunits (65). The rate of microtubule shortening reduces by about 50%, if one paclitaxel molecule is bound per several hundred tubulin subunits in a microtubule. Paclitaxel has also been used in this study to stabilize polymerized microtubules *in vitro* (see appendix A.1).

An important quantity for biopolymers such as microtubules is their stiffness, i.e. their ability to resist bending forces. This property is usually described in terms of the persistence length l_p . It is defined as the length over which the tangent angle becomes uncorrelated:

$$\langle \theta_{3D}(s) \rangle = \exp\left(-\frac{s}{l_p}\right). \quad (4.1)$$

This means, that the time average over the three dimensional tangent angle θ_{3D} decreases exponentially as the contour length s increases (63). It can also be expressed in terms of the flexural rigidity EI : $l_p = \frac{EI}{k_B T}$.

The persistence length for microtubules has been measured by filament tracking to be on the order of a few millimeters (66), while their overall length is on the order of a few tens of micrometers *in vivo*. Pampaloni et al. observed a dependence of the persistence length of microtubules on their contour length (67), also seen by Brangwynne and coworkers (68). But this observation was close to the noise limit and has to be treated carefully.

If the persistence length is much shorter than the contour length of a filament, $l \gg l_p$, it is called flexible. If $l_p \ll l$, a filament behaves as a rigid rod. Most biopolymers have a persistence length on the order of their contour length and are therefore called “semiflexible”.

¹Upon discovery the substance was named taxol. After commercial development the generic name was changed to paclitaxel and Taxol[®] became a trademark. The trademark is still commonly used throughout the literature, when referring to paclitaxel.

Semiflexible polymers in cells form networks with $a \ll \xi \lesssim l_p$, with monomer size a and a characteristic mesh size ξ . An estimate for the mesh size of a microtubule network has been given by Schmidt et al. (69) based on simple geometrical arguments. For a network of homogeneously distributed rigid rods on a cubic lattice, the total filament length per unit volume can be written as the ratio of the tubulin mass per unit volume and the mass of tubulin monomers per unit length c_T/ρ_L . In a mesh volume ξ^3 , the filament length per volume is then 3ξ , which yields a mesh size of:

$$\xi = \sqrt{\frac{3\rho_L}{c_T}} \approx \frac{0.89}{\sqrt{c_T}}, \quad (4.2)$$

with $[\xi] = \mu\text{m}$ and $[c_T] = \text{mg/ml}$. The last approximation has been obtained by inserting the corresponding values for the tubulin mass per volume in a microtubule (i.e. 13 tubulin monomers with 55 kDa and 5 nm each). This relation has also been verified by confocal microscopy (70).

Networks of such semiflexible polymers display unusual properties and cannot be adequately described by models valid for flexible or rod-like systems. Several theoretical studies have developed models for the dynamic shear modulus $G(\omega)$ of entangled or crosslinked networks of semiflexible polymers (27, 71, 72, 73). For the high-frequency behavior, which can be investigated by optical trapping microrheology, Gittes and MacKintosh calculated the shear modulus to be

$$G(\omega) = \frac{\rho\kappa^{\frac{5}{4}}}{15k_B T} (-2i\gamma\omega)^{\frac{3}{4}} - i\omega\eta, \quad (4.3)$$

with the filament density ρ and the transverse drag coefficient γ , (27). It shows a characteristic scaling regime of $\omega^{3/4}$, as was observed in experimental studies (74). This holds up to a certain frequency $\omega_{visc} \propto \rho^4$ above which equation 4.3 crosses over to viscous behavior $\sim \omega$. For the networks investigated here, this is expected to occur at frequencies above 100 MHz, which is currently inaccessible to optical trapping experiments, due to the limited response time of the electronics. This relationship has been used throughout this study for comparing the experimental results with the theoretical expectation.

4.1.2 Actin filaments

Actin filaments, also called microfilaments, are helical structures composed of globular actin monomers (G-actin, 45 kDa molecular mass) with a diameter of $d \approx 6$ nm. It

4. COMPOSITE NETWORKS

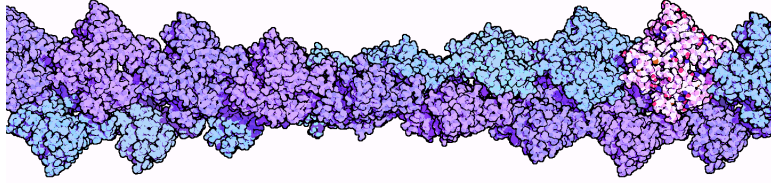


Figure 4.2: Structure of actin filaments - Each microfilament consists of two helical, interlaced strands of G-actin subunits (color coded on the right). Image adopted and modified from RCB protein data bank (75)

contains a nucleotide binding site for Adenosine-5'-triphosphate (ATP), or Adenosine diphosphate (ADP) and Mg^{2+} ions. The filament can either be viewed as a one-start left-handed helix or a two-start right-handed helix, which is more common in the literature (see figure 4.2). Like tubulin, the actin monomer is asymmetric, leading to a polarity of the actin filaments.

In vitro, actin polymerizes by self-assembly of three G-actin monomers. Actin with a bound ATP then binds itself to the plus-end and the ATP is hydrolyzed. ADP-bound actin dissociates slowly from the minus end and the free actin monomer releases its ADP-molecule. Subsequently it binds another ATP and the whole complex can again be incorporated into the filament. The actin filaments elongate approximately ten times faster at the plus end than at the minus ends. Depending on the concentration of the unpolymerized G-actin, a steady-state is reached at which the growth rate at one end matches the shrinkage at the other (treadmilling). *In vivo*, this process is significantly enhanced by associated proteins regulating growth and shrinkage of the filaments. Actin treadmilling plays an important role in polymerization-driven motility of cells, e.g. fibroblasts or keratocytes (63).

Actin filaments have a persistence length of approximately $17 \mu\text{m}$ (66, 68) and contour lengths of up to $20 \mu\text{m}$. They are semiflexible filaments, which affects the mechanical properties of F-actin networks. Due to their high aspect ratio, l_p/d , F-actin becomes sterically entangled at very small volume fractions. The mesh size of filamentous actin ξ can be related to the G-actin concentration c_A , analogous to equation 4.2 by the following approximation:

$$\xi \approx \frac{0.3}{\sqrt{c_A}}. \quad (4.4)$$

This relation was confirmed in (69) by studying the diffusion of latex beads in F-actin.



Figure 4.3: Cloning of the tetrameric chimera DK4mer - The motor domain and the neck-linker of the *Xenopus laevis* Eg5 have been replaced by the corresponding domains of the *Drosophila melanogaster* Kinesin-1 heavy chain. Due to their size, the motor proteins have been expressed in *Spodoptera frugiperda* (SF-9) cells. Illustration adopted from (77).

4.1.3 Motor proteins

Changes in morphology, directed motion and active transport in cells would not be possible without the generation of forces and conversion of chemical to mechanical energy. In all living organisms this is accomplished by molecular machines or motors. Motor proteins are enzymes that convert chemical energy released by the hydrolysis of ATP into mechanical work, thereby moving along specific substrates. Details concerning this mechanochemical cycle, its molecular basis and the physical properties of motor proteins can be found in (63).

Cytoskeletal motor proteins make use of the “infrastructure” provided by the biopolymer network inside cells. One can distinguish two different kinds of motor proteins, based on the substrate they are moving on: Actin-associated motors, such as myosin, move along F-actin microfilaments. Tubulin-associated motors, such as dynein and kinesin, move along microtubules. Another characteristic is the directionality of the motors, which utilizes the asymmetry inherent in the filaments, as discussed in the previous sections. Plus-end and minus-end directed motors are categorized, depending on the direction that the motors advance along the filaments. Recent research has also shown the ability of some motors to change their directionality depending on the environmental conditions (76).

The motor protein employed in this study is a tetrameric chimera first described in the diploma thesis of Christina Thiede (77). The motor domain and the neck-linker

4. COMPOSITE NETWORKS

of the *Xenopus laevis* Eg5 have been replaced by the corresponding domains of the *Drosophila melanogaster* Kinesin-1 heavy chain. In this way, a homo-tetrameric motor protein, called “DK4mer”, has been constructed, which is depicted in figure 4.3. The DK4mer is a processive motor with the ability to slide two microtubules apart. It runs at a velocity of about 500 nm/s and shows a very high run length of up to 14 μm , depending on the ambient conditions, which is a more than a 6-fold increase compared to wildtype Kinesin-1. The enhanced run length together with the long dwell time on microtubules make the DK4mer a good model system to study motor protein effects on an *in vitro* cytoskeletal network.

4.2 Microrheology of cytoskeletal model systems

4.2.1 Single-component networks of microtubules

Networks consisting of paclitaxel-stabilized microtubules polymerized from 2 mg/ml tubulin at 37°C in the presence of GTP and MgCl_2 were investigated. The protocol can be found in appendix A.1.

The mesh size of such a network can be approximated by using equation 4.2, yielding about 0.6 μm . Large beads with a diameter of 4.74 μm were used to be well above the mesh size.

Active and passive one- and two-bead microrheology were used to investigate these networks. For the one-particle measurement several individual beads were trapped at least 10 μm away from the surface. The position fluctuations were recorded typically for 30 s with a sampling frequency of 195 kHz and the complex shear modulus was computed according to the procedure described in section 3.4.2.

The results for several different samples prepared in the same manner are displayed in figure 4.4, where the real and imaginary part of the complex shear modulus are plotted versus frequency. For the real part, large variations among the different measurements are observed. The low frequency regime is noisy, due to the limited number of data points and a typical ambiguity due to trap correction, performed in water after the measurements. Deviations of the trap stiffness due to the viscoelastic surrounding, as well as bead polydispersity, can introduce errors into the obtained shear modulus. At high frequencies the effect of the finite frequency cut-off of the Kramers-Kronig integral

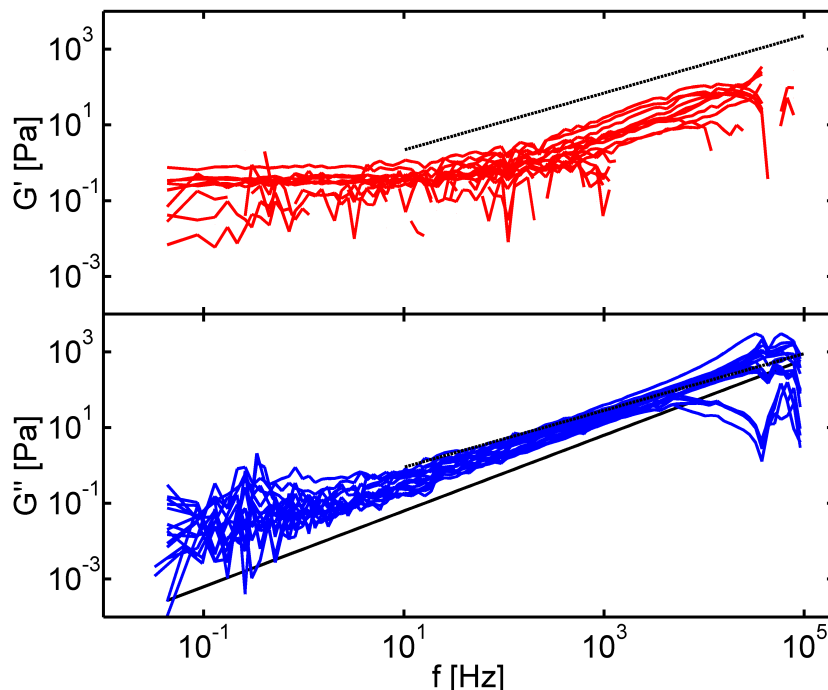


Figure 4.4: Shear modulus of a microtubule network obtained from 1PMR - Real and imaginary part as obtained from several passive 1-particle measurements in a network of microtubules polymerized from 2 mg/ml tubulin. The dashed lines indicate the theoretical prediction of equation 4.3. For the loss modulus also the curve for water, $G'' = -i\eta f$, is plotted.

can be seen (as mentioned in 3.4.2). The theoretical prediction of equation 4.3, is plotted for comparison. Here, the persistence length was chosen to be 2 mm, the filament density was estimated to be $\rho = 1.3 \cdot 10^{11} \text{ m}^{-2}$ following (70) and the drag coefficient is computed to be $\gamma = 1.7 \cdot 10^{-3} \text{ Pas}$, assuming a rigid rod $10 \mu\text{m}$ away from the surface as in (63, 68). This model is valid for frequencies higher than the relaxation time of the longest wavelength mode, which depends on the length of the filaments, which is not known. Assuming $10 \mu\text{m}$, the theory should be valid above frequencies of 10 Hz. The observed power-law reflects the expected $\sim f^{3/4}$ behavior, but the magnitude of the shear modulus however is smaller than the predicted value. This might be due to the assumptions made above for computing the shear modulus G . The loss modulus G'' also shows noisy behavior in the low frequency part, but is more reproducible at intermediate frequencies. At high frequencies around 40 kHz characteristic peaks

4. COMPOSITE NETWORKS

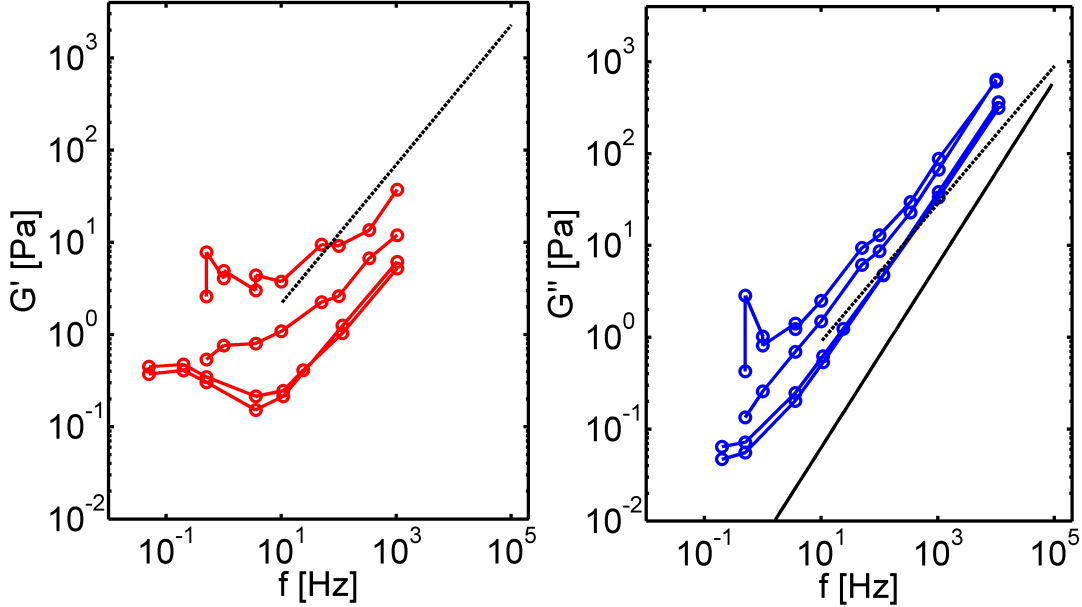


Figure 4.5: Shear modulus of a microtubule network obtained from 1AMR - Storage and loss modulus versus frequency are plotted. G' exhibits some ambiguity. For frequencies above 1 kHz the computed modulus dropped below zero, maybe due to an improper correction of the system response. G'' shows a better reproducibility, but scales with a power-law higher than expected for a semiflexible filament network (dashed lines). $G'' = -i\eta f$ is plotted for comparison (solid line).

occur, which could be traced back to the acousto-optical deflector, but whose origin is unknown. Their magnitude differs from sample to sample, which might be due to changes in the alignment from everyday optimization of the setup. The magnitude fits the theoretical expectation, but here the power-law shows a deviation. The measured loss modulus displays a power-law $\sim f$. This may hint at the existence of a depletion layer around the beads and the limitation of 1PMR in probing only the volume in the proximity of the beads, as similar effects were observed in (46, 53). In the same samples, several active measurements using the same beads as for the passive method were performed. The beads were oscillated with an amplitude of 100 nm using the acousto-optical deflector driven by the lock-in amplifier (section 3.4.1). A frequency sweep was then performed in the range of 0.1 to 100 kHz. The results for all measurements are displayed in figure 4.5. A behavior similar to 1PMR can be seen, with a slight difference in the magnitude of the complex shear modulus. Above 1 kHz the values of the storage

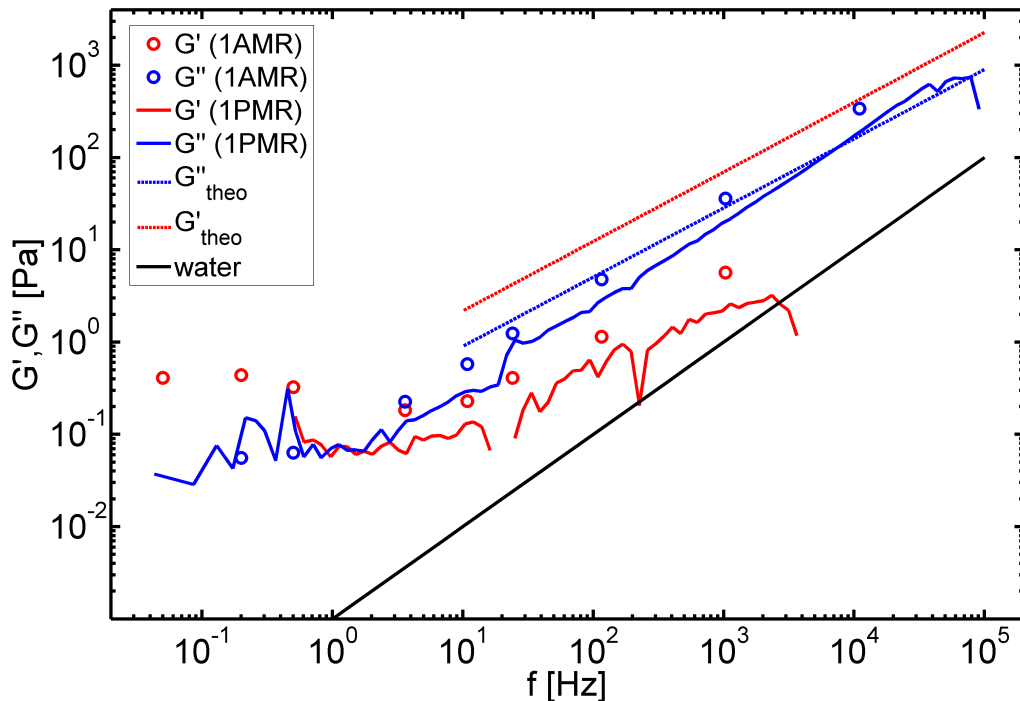


Figure 4.6: Comparison of active and passive measurements - Averaged values for the complex shear modulus were computed from the one-particle data. The lines show the passive, the circles the active measurements; red stands for the real, blue for the imaginary part of G . A slight offset between active and passive method is visible. The measured moduli deviate from the high frequency prediction of eq. 4.3 (dotted lines). At low frequencies the results are comparable to values given in the literature (53, 60). The dotted lines display the theoretical prediction.

modulus drop below zero. This might be due to the correction of the system response as described in section 2.6.2. At high frequencies, the system response in general is likely to show an ambiguity (42), which can lead to an “over-correction” in this regime.

For a better comparison the results from 1- and 2PMR were averaged and again plotted over frequency.¹ As can be seen in figure 4.6 for both real and imaginary part of the complex shear there is a slight offset between 1PMR and 1AMR for unknown

¹Throughout the microrheology literature no error bars are displayed when computing absolute numbers of the material properties. This is partly due to the large variation inherent in the investigation of biological samples, but also the influence of error-prone parameters going into the calculation, e.g. the trap stiffness with errors of up to 30% or a priori unknown values of the bead size or the local temperature.

4. COMPOSITE NETWORKS

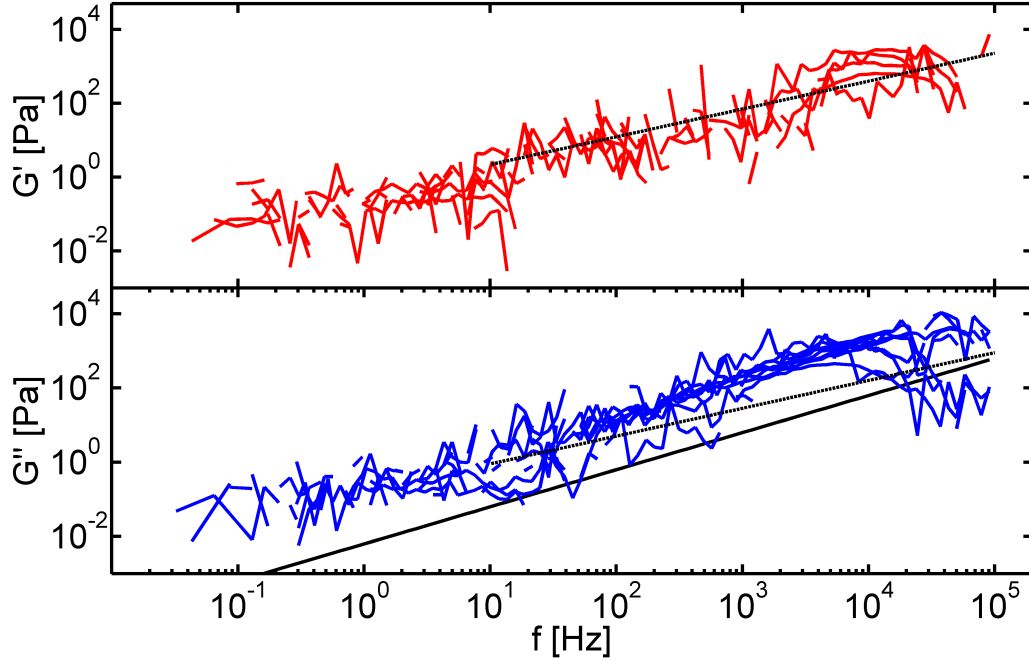


Figure 4.7: Two-particle passive data - The storage and loss modulus are shown for all two-particle passive measurements. Only the cross-correlation of the bead motion parallel to the connection axis was computed. The data is noisy over the whole frequency bandwidth. Theory curves (dotted lines) are again plotted as in the figures before.

reasons. Before and after each active measurement, the passive experiments were performed to assure no significant changes in the sample occurred during the time of the measurement. The calibration factor for both methods is the same, as well as the trap stiffness. A calibration factor for the AOD displacement goes into the calculation of the force on the bead. This calibration is performed in water and may be different for another, non-viscous medium. The elastic modulus obtained from 1PMR is noisy and drops below zero at several points. The 1AMR data shows the onset of an elastic plateau at frequencies below 10 Hz with a magnitude of about 0.5 Pa, which is in agreement with prior results from video-microrheology as given in (60, 70). Since there is some discrepancy between the measured shear modulus and the theoretical prediction and it is known that 1PMR results can yield values differing from the bulk properties, two-particle measurements were performed in the same networks. The distance between beads was around 10 - 15 μm , i.e. 2 - 3 times the bead diameter. One bead was oscillated with a 1064 nm laser using an AOD, while the correlated motion

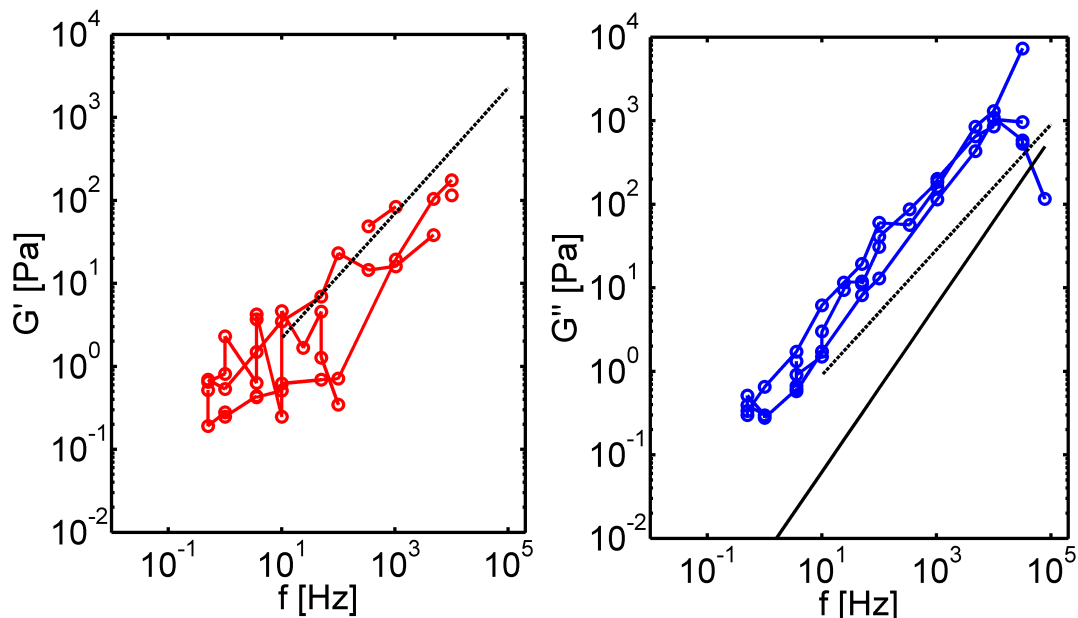


Figure 4.8: Two-particle active data - The elastic response G' shows scattered data points. Several data points for one frequency indicate repeated measurements, showing a lack of reproducibility. G'' is comparable for all measurements, but deviates from the theoretical expectation (dotted line). The shear modulus for water is plotted for comparison (black solid line).

of the second bead was probed with a 830 nm laser. One can in principle compare the cross-correlated motion of beads parallel and perpendicular to the connection axis. As the lock-in amplifier could not lock to the reference signal for the perpendicular case, the oscillation was only applied parallel to the axis connecting the beads. Accordingly, only the cross-correlation in that direction was computed from the two-particle passive data. Figure 4.7 shows the results for all 2PMR experiments. Again the theoretical prediction is plotted for comparison, showing a somewhat different picture than the one-particle data. Here, the real part agrees better with the theoretical curve, while the imaginary part is above the expected value, showing again a frequency scaling closer to one. The corresponding active two-particle measurements are shown in figure 4.8, displaying a similar behavior.

All measurements were averaged and plotted together with the results obtained from the one-particle experiments, as depicted in figure 4.9. The elastic part G'' as computed from the 2PMR data is too noisy to make any meaningful statements. In

4. COMPOSITE NETWORKS

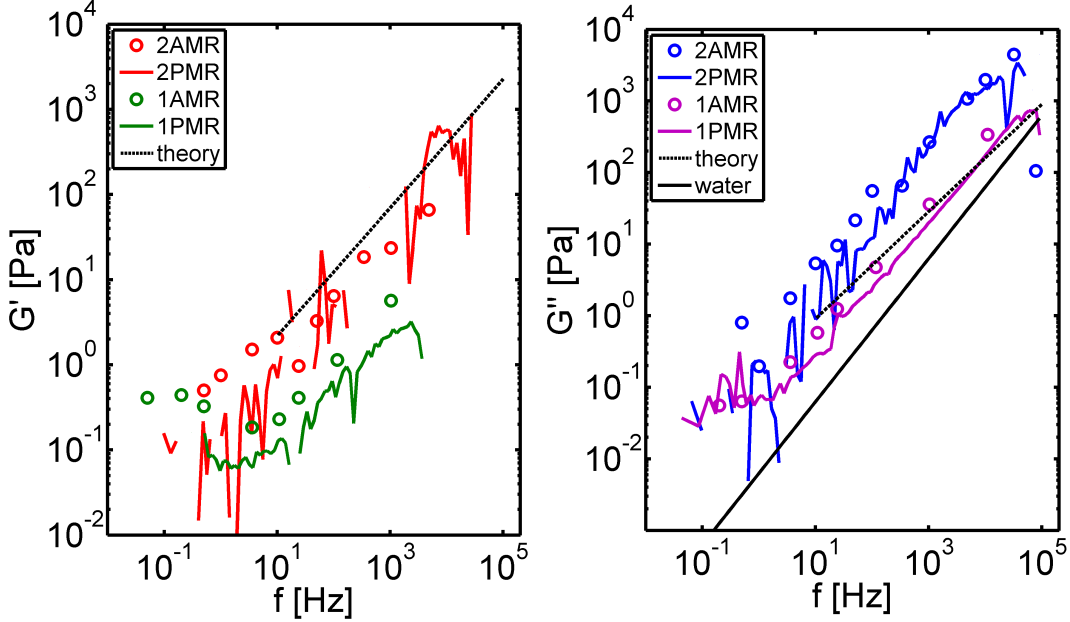


Figure 4.9: Comparison of one- and two-particle experiments - The elastic modulus as obtained from the two-particle passive data (red solid line) is subject to excessive noise. The active data (red circles) are close to the theory curve (black dotted line). The values obtained from 1A- and 1PMR (green line and circles) are about an order of magnitude lower. G'' shows a similar relation. The frequency scaling is closer to pure viscous behavior.

contrast, the 2AMR data agrees better with the theoretical prediction than the one-particle data. The two-particle results for the imaginary part are less noisy at least at high frequencies, but are significantly higher than the theoretical curve. As already pointed out, the power-law displays a more viscous behavior than is expected. For the 2AMR data the viscous part is somewhat closer to $\sim f^{0.8}$, which better fits expectation.

Finally, the effect of the tubulin concentration on the material properties of the network were investigated. As the two-particle method was limited by noise, only 1PMR and 1AMR were performed. Microtubule networks were prepared from three different concentrations of tubulin, 0.7, 2.0, and 2.7 mg/ml and the results for the complex shear modulus are shown in figure 4.10. For the elastic modulus there is a large offset between 1AMR and 1PMR for the highest concentration. The active data displays an increasing elasticity from 0.01, to 0.5 up to 2.5 Pa at frequencies below 10 Hz and the passive data seems to collapse onto a comparable value. The viscous part

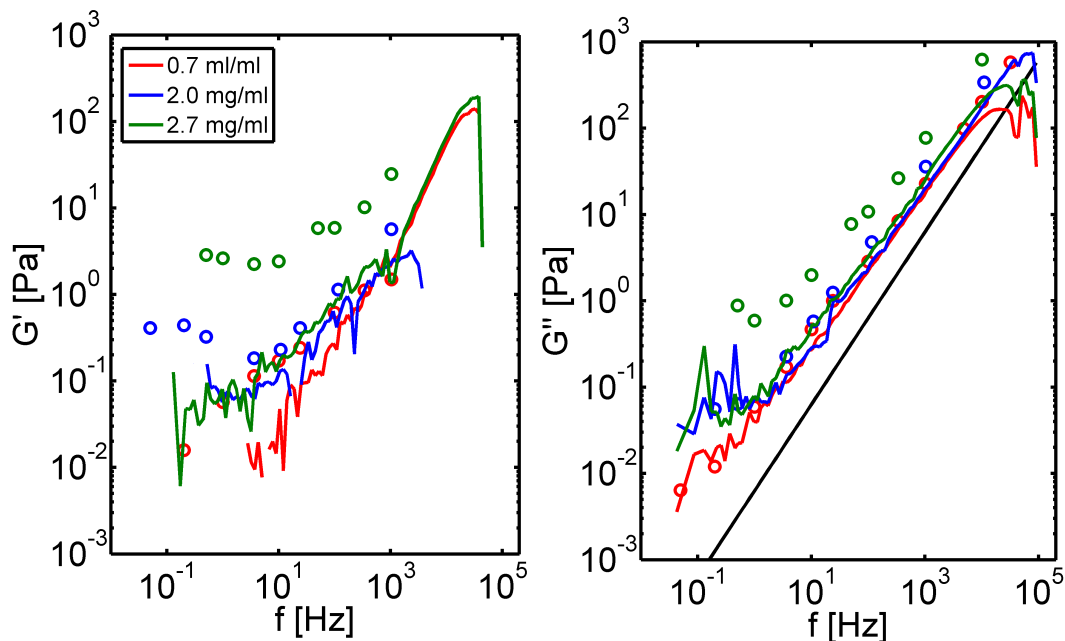


Figure 4.10: Shear moduli for different tubulin concentrations - The one-particle approach was chosen for three concentrations of tubulin as given in the legend. The circles show the active measurement, which displays an offset from the passive method, especially for the highest concentration. An increase in the elastic response is visible as expected for higher filament density. The viscous response is comparable for all three concentrations.

however is comparable for all three concentrations, despite a small offset between active and passive measurement observable for the highest concentration. The proximity to a viscous-like scaling suggests that the beads might inhabit a small cavity and therefore the material response is dominated by the solvent.

4.2.2 Nonequilibrium networks of microtubules and DK4mer

So far, networks of microtubules in equilibrium have been investigated. As the next step, a microtubule-associated motor protein, the tetrameric chimera DK4mer described in section 4.1.3, was added. The motor protein is able to bind to, and thereby cross-link, two microtubules and drive them apart in an antiparallel fashion. The ATPase activity of the protein drives the system out of thermodynamic equilibrium. Therefore, rich dynamics and a violation of the fluctuation-dissipation theorem is expected for this kind of model system, as was observed in F-actin networks driven by

4. COMPOSITE NETWORKS

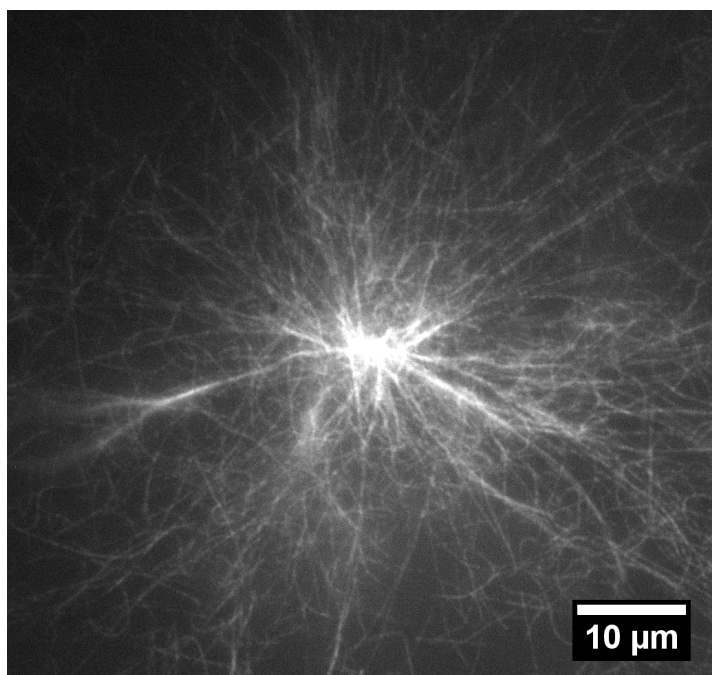


Figure 4.11: Microtubule aster - Fluorescence image of rhodamin-labeled microtubules self-organized into an aster by the motor protein chimera DK4mer.

myosin motors (42, 57). The motor proteins were added to a polymerized network of fluorescently labeled microtubules together with ATP, MgCl_2 and $4.74 \mu\text{m}$ beads, according to the protocol listed in appendix A.3. The samples were first investigated with fluorescence microscopy for any sign of motor activity. A general feature which could be observed, was the self-organization of the microtubules into star-like patterns or asters. A typical image is depicted in figure 4.11. This behavior has also been observed by Nédélec et al. (78), where several kinesin K401-bio dimers were joined by streptavidin-biotin bonds, and in (79), where several multimeric motor constructs were studied, accompanied by numerical simulations of the pattern formation. Within a few minutes the motor proteins accumulate, forcing the microtubules into a pattern similar to the bipolar spindle formed during cell mitosis and meiosis. Indeed this process might play a key role in the assembly of the spindle apparatus during cell division (80).

Investigating these networks using microrheology is challenging due to the large inhomogeneity of the samples. As can be seen in the DIC-image in figure 4.12, the probe particles accumulate in the center of the asters, making the measurement of a single bead difficult.

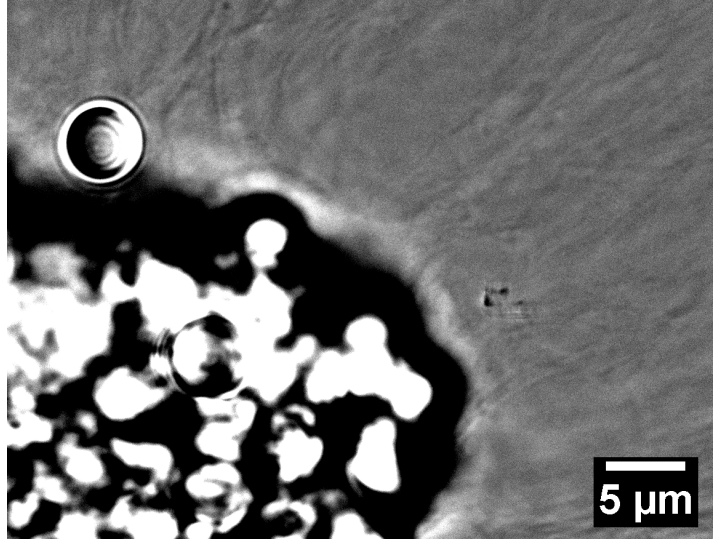


Figure 4.12: Bead aggregate in a nonequilibrium network - DIC-image of $4.74\ \mu\text{m}$ beads aggregating at the center of a microtubule aster. Bundles of microtubules are visible pointing away from the center in a star-like pattern. Separated beads at the periphery like the one shown here were chosen for microrheology measurements.

The system appears very dynamic with the beads experiencing large forces. An active measurement takes at least half an hour to perform, due to the time it takes the lock-in amplifier to lock onto the reference signal and average the output value over a time period corresponding to the oscillation frequency. This time span increases with decreasing frequency, where the motor activity is expected to take place (57).

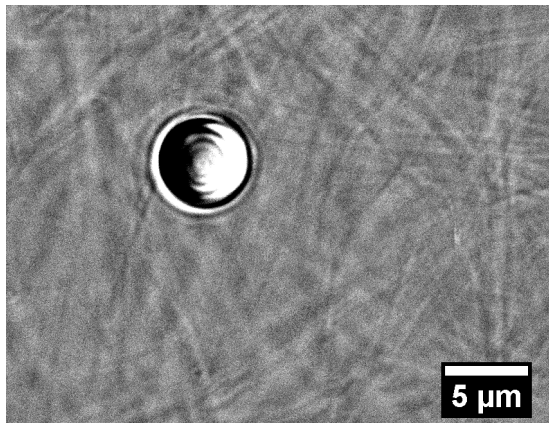


Figure 4.13: Nonequilibrium network at lower motor concentration - The motor protein concentration was lowered by a factor of 2.5 compared to the situation depicted in figure 4.12. A more homogeneous distribution of microtubules is apparent, improving the conditions for microrheology measurements.

No measurement can be performed if the bead is pulled out of the focus by the motors. Therefore, beads at the periphery of the asters have to be chosen, which do not

4. COMPOSITE NETWORKS

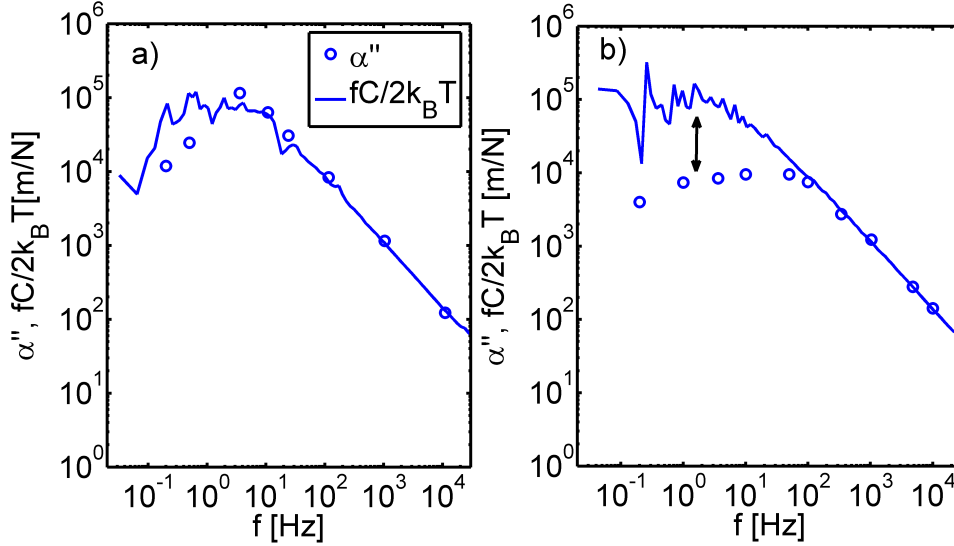


Figure 4.14: Response of a microtubule network with and without DK4mer - The imaginary part of the complex response function $\alpha''(f)$ as measured by 1AMR (open circles) compared to the normalized power spectrum $fC(f)/(2k_B T)$ obtained from 1PMR (line). In the equilibrium network in a) both methods agree. In the nonequilibrium network in b) the normalized power spectrum shows an increased magnitude compared to $\alpha''(f)$ below 10 Hz. This is due to the presence of active fluctuations by the motor proteins, violating the FDT. The network is also much stiffer as indicated by the lower magnitude of $\alpha''(f)$.

move or move very slowly. It turned out that no significant difference between 1PMR and 1AMR could be seen. This could mean, that the areas chosen for measurement were completely depleted of motor proteins.

Nevertheless, by lowering the motor concentration by a factor of 2.5 it was possible to get stable networks without large inhomogeneities, but still a fraction of active movement. A detail of such a network is shown in figure 4.13. The imaginary part of complex response function $\alpha''(f)$ was calculated from the 1AMR data. Switching off the driving laser, the position fluctuations of the bead were recorded and the normalized power spectrum $fC(f)/(2k_B T)$ was calculated, which is related to $\alpha''(f)$ in equilibrium (eq. 3.20). In figure 4.14 both values are plotted over frequency. For the equilibrium network as shown on the left, both methods agree over the whole frequency range. In the presence of motor proteins, a deviation between 1PMR and 1AMR at frequencies below 10 Hz becomes apparent (shown in b) in figure 4.14). These additional

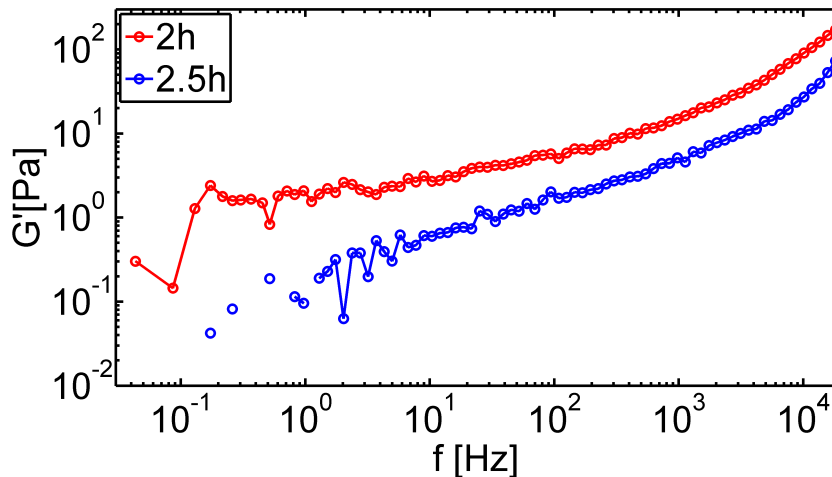


Figure 4.15: Network stiffening - Repeated measurement of the elastic modulus of the network. Between two (red) and two and a half hours (blue) after sample preparation an increase in network stiffness can be observed. (Where the connecting line is interrupted, the values drop below zero.)

fluctuations showing up in the power spectrum can be interpreted as the nonequilibrium fluctuations introduced by the active force generation of the motor proteins.

Along with the motor activity an increased stiffening of the sample could be observed, as was also seen in (57) and theoretically predicted in (81). Before and after each 1AMR measurement several passive measurements were carried out. In some cases the sample properties drastically changed over time. In figure 4.15 the storage modulus is plotted over frequency for a measurement carried out two hours after sample preparation, compared to a measurement half an hour later. The stiffness increased about a factor of three in this short time frame. Care has to be taken when interpreting the data of such rapidly changing samples. This applies especially to the long-lasting active measurement, where a significant change in the sample properties over time can introduce a time-dependence between the individual measurement points. To avoid such artifacts, a frequency measured at the beginning of the experiment was measured again at the end.

Nevertheless, a large variation in the data was observed, as is depicted in figure 4.16, where the complex shear modulus for all active measurements is plotted. Due to the inhomogeneity of the samples and due to the fact that stiffness varies with time, in particular the elastic modulus scatters over two orders of magnitude. To get at least

4. COMPOSITE NETWORKS

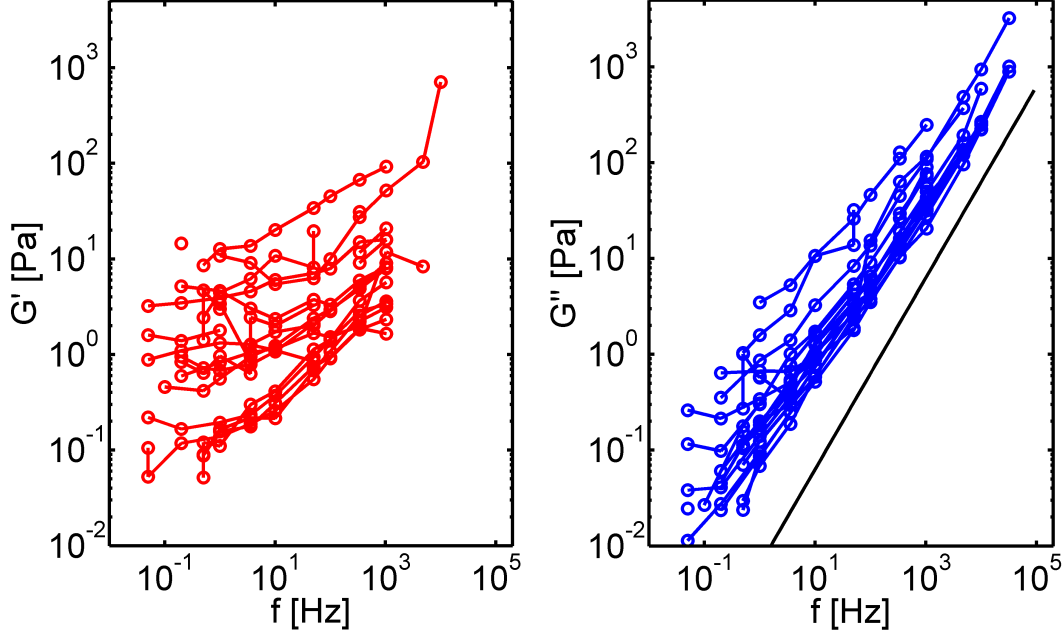


Figure 4.16: Variation of the shear modulus for all measured samples - Real and imaginary part of the complex shear modulus as obtained from 1AMR are plotted. The storage modulus shows a drastic scattering of the data, representing the inhomogeneity of the samples. The loss modulus has a better reproducibility. The line for water is shown in black.

a qualitative comparison to the equilibrium microtubule networks, the results for all measurements were again averaged. The shear modulus was also computed from the passive measurements. Here, it is important to note that due to the violation of the FDT, the power spectrum is not linked to the complex response function anymore. Thus, for low frequencies the obtained values cannot directly be interpreted as the complex shear modulus of the material surrounding the bead.

The mean shear moduli obtained from 1AMR and 1PMR for the microtubule networks with and without motor proteins are shown in figure 4.17. The storage modulus for the nonequilibrium network is up to an order of magnitude higher than that of the network without motors. The imaginary part is comparable in magnitude, but the power-law behaviors are different. In the high frequency regime between 100 Hz and 15 kHz of the nonequilibrium network, a fit with an allometric function $y = ax^b$ was performed on the 1PMR data. A power-law of $\sim f^{0.76}$ can be observed. This agrees

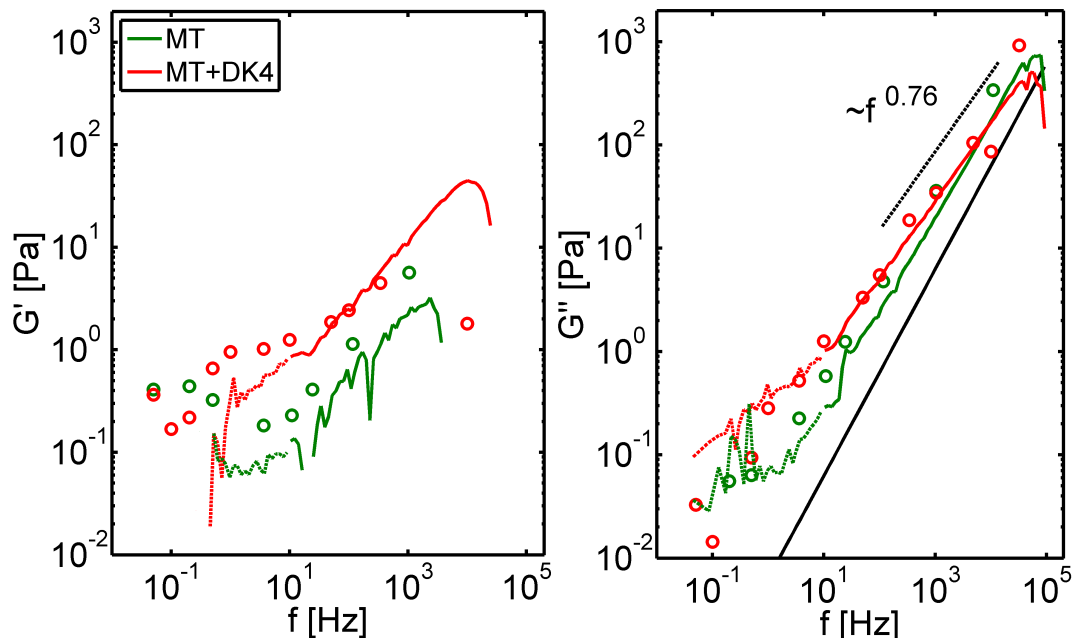


Figure 4.17: Comparison of equilibrium and nonequilibrium network - The shear modulus for networks with (red) and without (green) motor proteins is compared. Due to the violation of the FDT the 1PMR data below 10 Hz does not reflect the true shear modulus of the network; the data is therefore only displayed as dotted lines. The elastic modulus of the nonequilibrium network is stiffer than the network without motors, with an ambiguity at very low frequencies. The loss modulus for the equilibrium network scales with about f^1 , while the network with motor proteins shows a dependency of $f^{0.76}$. This value was obtained by fitting an allometric function to the 1PMR data in the range of 100 Hz to 15 kHz. The fit is shown as the black dotted line, which was offset for clarity.

with the expected value of 0.75 for a network of semiflexible filaments. The cross-linking through the motor proteins has likely prevented the formation of a depletion layer around the beads, as might have happened in the network without motors.

4.2.3 Composite networks of microtubules and F-actin

So far networks consisting solely of microtubules have been examined. The cytoskeleton in cells is actually a composite of microtubules, F-actin and intermediate filaments. To construct a better model system, F-actin was added to the microtubule network. Polymerized microtubules and G-actin, together with 4.74 μm beads, were mixed and actin polymerization buffer added. The actin polymerized around the microtubules

4. COMPOSITE NETWORKS

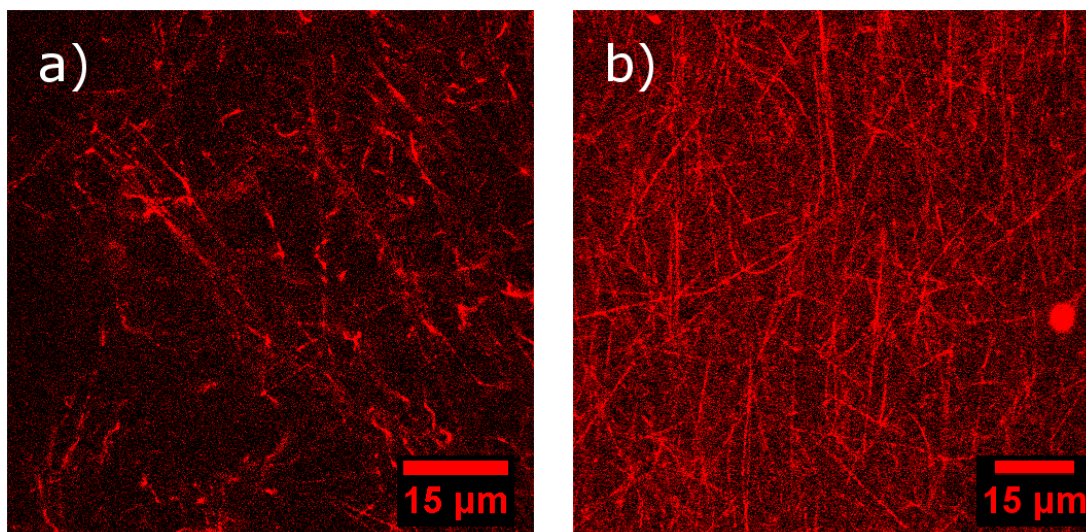


Figure 4.18: Confocal images of microtubule and composite networks - In a) a microtubule network polymerized from 0.7 mg/ml tubulin is shown. The rhodamin-labeled microtubules appear highly curved, which is probably due to the low scan speed of 50 Hz by 4 averages per line scan. In the composite network depicted in b) the microtubules' shape is very straight and does not change much over time. The scan speed in this case had to be reduced to 10 Hz, corresponding to image acquisition time of about 3 min. The actin is unlabeled and not visible. All images were taken with a Leica TCS SP5 X.

at room temperature, to form a composite network containing 0.7 mg/ml tubulin and 0.6 mg/ml G-actin (see the protocol in appendix A.4). In figure 4.18 confocal images of fluorescently labeled microtubules are shown in a pure microtubule and a composite network. The microtubules in the single-component network (figure 4.18a) are very dynamic due to the low filament density. The microtubules appear to be highly curved, which is likely to be an artifact arising from the low scan speed. In the composite network the microtubules are very straight and tightly confined inside the F-actin network (figure 4.18b). The scan speed was 5 times lower compared to the situation in a), emphasizing the reduced mobility of the microtubules.

Active and passive one- and two-particle microrheology measurements were carried out in the composite networks. As an example, the results for all active one-particle measurements are shown in figure 4.19. The data show better reproducibility than the microtubule experiments. This is most likely the effect of the small mesh size of F-actin, which is about 0.4 μm according to equation 4.4. This prevents large fluctuations of

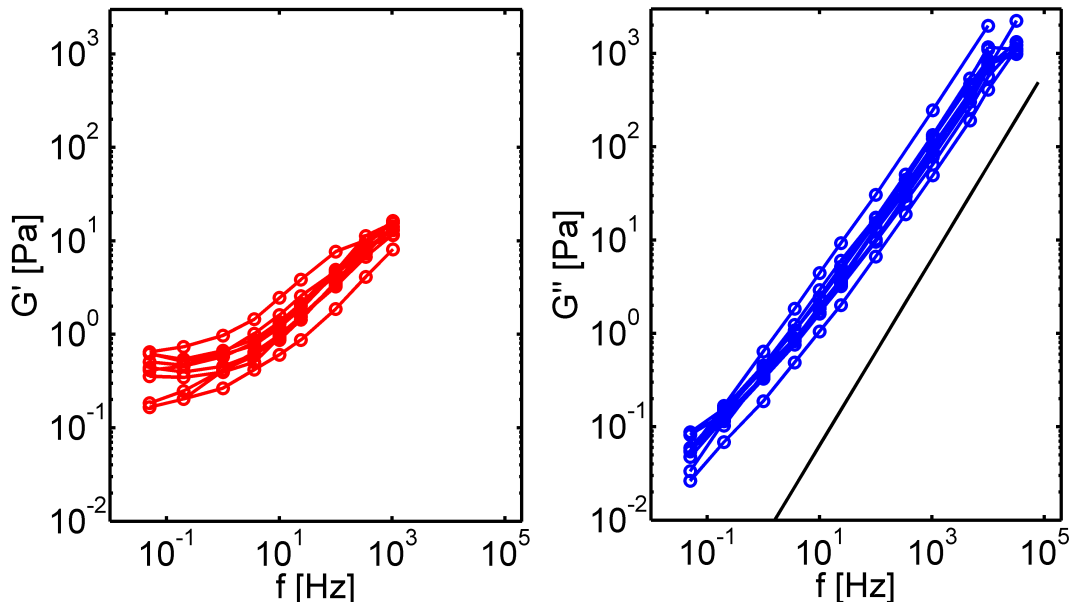


Figure 4.19: One-particle active measurement in the composite network - The complex shear modulus is plotted over frequency for all active one-bead measurements performed on the composite. The data exhibits a narrower distribution compared to the single-component networks of microtubules.

the bead position during the measurement, which can thereby be better centered in the focus of the optical trap and monitored with greater accuracy. Also, the filament density in the composite networks might be more homogeneous than in the microtubule networks, as suggested by the confocal images (figure 4.18).

The averaged results for 1- and 2-particle AMR and PMR are depicted in figure 4.20. The two-particle data again are noisy. For the elastic modulus between 10 Hz and 1 kHz both active and passive two-particle data is higher in magnitude than the one-bead data. Below that regime, the active data drops below the values obtained from the one-particle method, which is unexpected. Pelletier et al. (60) do not see such a cross-over. In this low frequency regime the noise limitation of our method compared to long-term video-microrheology could be the reason for this ambiguity.

For the viscous part of the shear modulus a clearer picture can be drawn. While the imaginary part of the 2PMR data is again subject to a lot of noise and deviates significantly from the 2AMR data below 10 Hz, both active and the one-particle

4. COMPOSITE NETWORKS

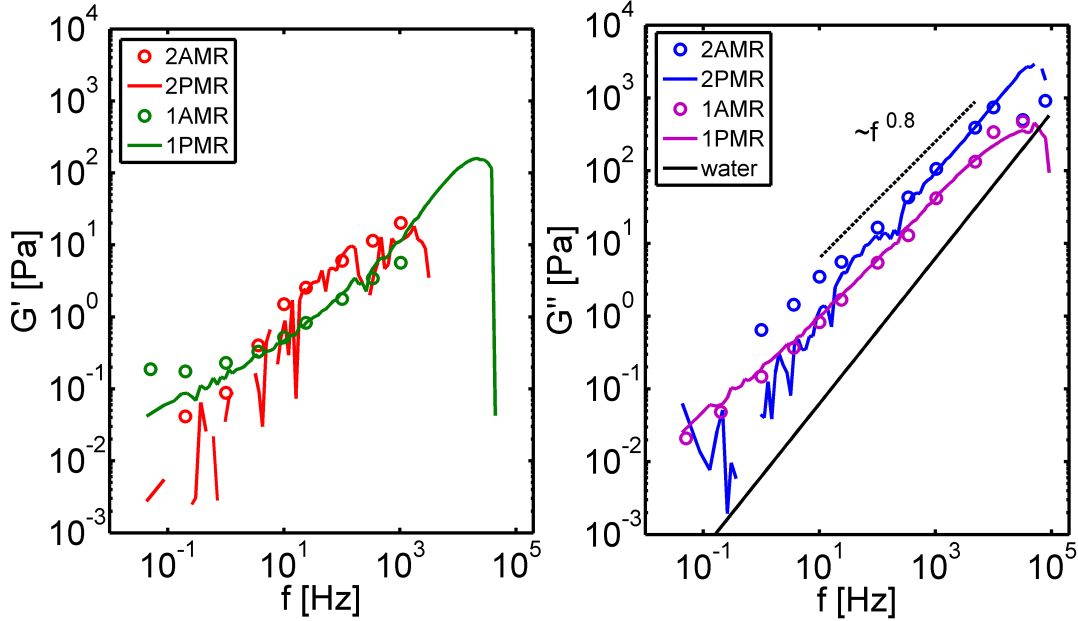


Figure 4.20: Comparison of shear moduli obtained by one- and two-particle data - Between 10 Hz and 1 kHz both 2AMR and 2PMR data is higher in magnitude compared to 1PMR. At low frequencies the active data drops below the values obtained by the one-particle method. $G''(f)$ from 2PMR is noisy and deviates significantly from 2AMR below 10 Hz. The active data and 1PMR however show the same characteristic. The two-particle data is higher in magnitude, while the power-law agrees for all three methods. The data was fitted in the range of 10 Hz to 10 kHz, yielding a power-law of $f^{0.80 \pm 0.01}$, as indicated by the black bar.

passive measurement show a similar mechanical behavior for the composite. In the high-frequency regime, all three methods yield a power-law of $f^{0.80 \pm 0.01}$, obtained by fitting the data in the range of 10 Hz to 10 kHz. This is within 10% of the expectation for a semiflexible filament network and agrees with the findings in (60).

The results obtained so far can be compared to the shear modulus measured for single-component networks consisting only of microtubules or F-actin respectively. In both cases the respective other filament type was replaced by buffer, yielding the same monomer concentration as for the composite. For these cases one-particle measurements have been carried out and the results are shown in figure 4.21. For the storage modulus a deviation between 1AMR and 1PMR can be observed especially at low frequencies, which makes the interpretation of the data difficult. The microtubule networks are less

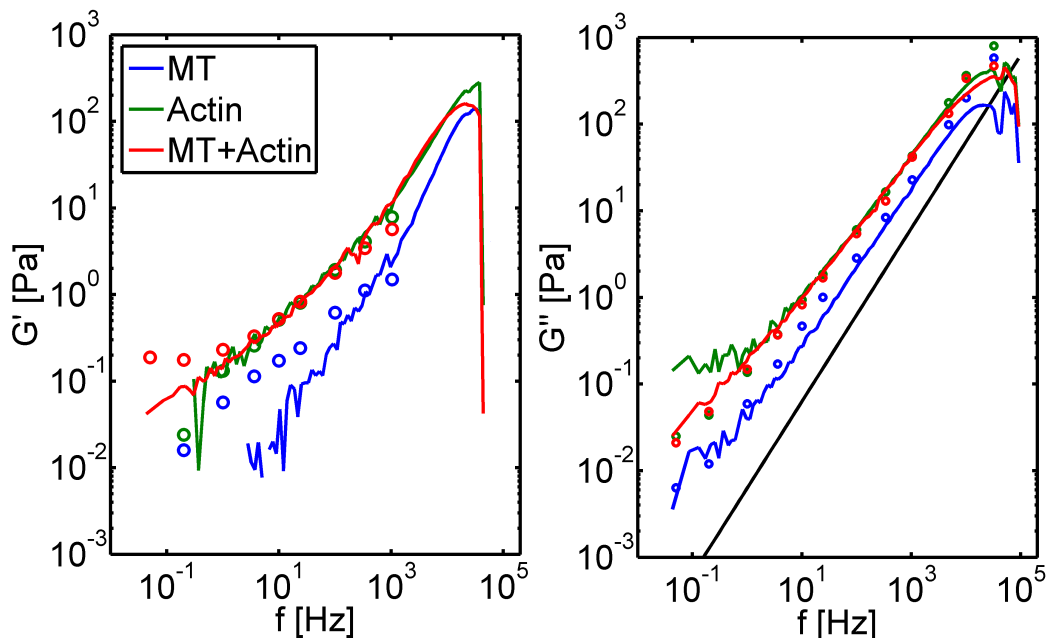


Figure 4.21: Composite versus single-component networks - The shear modulus for the composite network displays similar mechanical properties compared to the F-actin network. Deviations at low frequencies are observed between 1AMR and 1PMR. At high frequencies the finite frequency cutoff of the Kramers-Kronig integral can be seen in G' for the 1PMR data. The viscous part is less noisy, again showing a similar behavior of composite and F-actin, scaling with a power-law close to $f^{0.75}$, while the microtubule solution approaches a more viscous scaling behavior.

rigid than the F-actin and composite networks, which exhibit an elastic modulus of the same order. In (60) the composite was slightly less rigid than the actin network, which might also be the case for the samples studied here, but cannot safely be concluded from the data due to the ambiguity at low frequencies. Also the concentration of actin used in (60) was a factor of two higher; the tubulin concentration exceeded the actin concentration by another factor of three.

The loss modulus again shows more coherent characteristics. Despite an offset between 1AMR and 1PMR in the case of F-actin, the data is less noisy and easier to compare. For the microtubules, $G''(f)$ is significantly lower in magnitude than for F-actin and the composite, and the power law once more approaches a value close to one. The composite and the F-actin network show a very similar behavior over a

4. COMPOSITE NETWORKS

broad range of frequencies from 10 Hz to 10 kHz. Both show the expected power-law dependence close to $G''(f) \sim f^{3/4}$.

4.2.4 Composite networks with cross-linkers

In cytoskeletal networks proteins associated with the different classes of filaments play an important role in the mechanical properties of cells. Several studies on actin-associated proteins show their large influence on the behavior of the network (see for example (54)). The addition of physiological cross-linkers leads to additional complexity, due to their inherent dynamical properties, i.e. continuous binding and unbinding. Recent experimental and theoretical studies investigate the properties of F-actin networks including such transient cross-linkers (see for example (82) and (83)).

In this section, the effect of adding a static cross-linker to composite networks consisting of F-actin and microtubules is studied. For simplicity, microtubules were cross-linked by incorporating biotinylated tubulin in a ratio of 1:10 and neutravidin was added together with the G-actin (see A.4 in the appendix). A DIC-image of such a network is displayed in figure 4.22. Bundles of cross-linked microtubules are visible

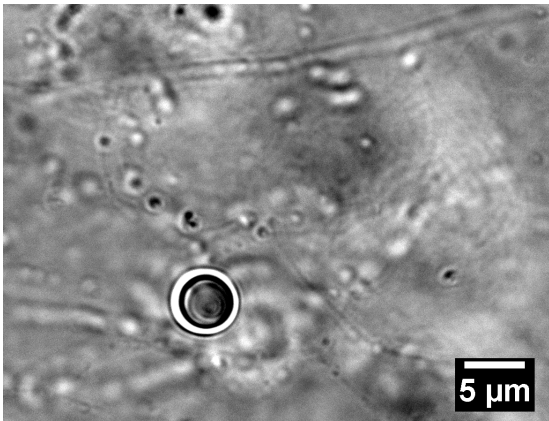


Figure 4.22: Composite network with cross-linked microtubules - Biotinylated tubulin was incorporated into the microtubules. Together with the G-actin and beads, neutravidin was added, resulting in composite networks with cross-linked microtubules. A lot of debris was observed in all samples, which could be fractions of microtubules or unpolymerized tubulin attaching to the biotinylated microtubules.

together with a lot of debris. This might be unpolymerized tubulin or short pieces of microtubules attaching and aggregating at the biotin-sites of the microtubules.

1AMR and 1PMR were performed in the cross-linked network, which otherwise was prepared identically to the composite network described in the previous section. The complex shear modulus is compared to the results for the non-cross-linked networks in figure 4.23. The cross-linked network is about a factor of two stiffer than the non-cross-linked network, as can be seen from the real part of the shear modulus. Otherwise, the

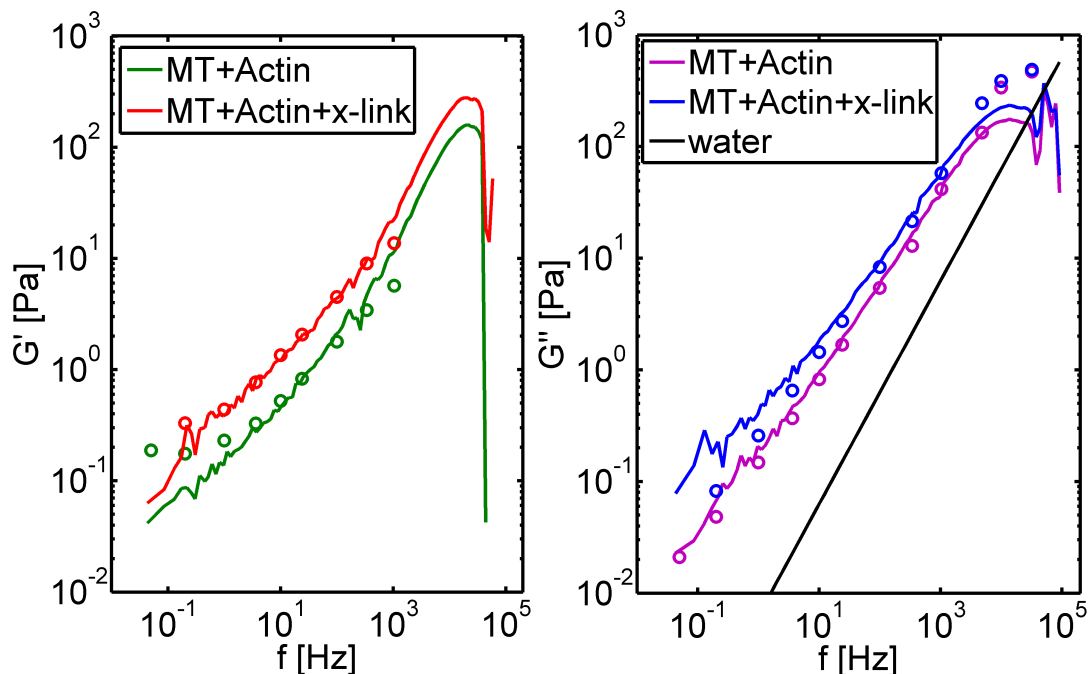


Figure 4.23: Shear moduli for composite networks with and without cross-links - The storage modulus of the cross-linked network (shown as green lines and circles) is about two times stiffer than the non-cross-linked network. The same applies to the viscous part of the shear modulus. At low frequencies deviations between 1AMR and 1PMR are apparent.

network shows similar mechanic behavior. The loss modulus is also about two times higher for the cross-linked network. The active measurements for both systems agree in terms of their power-law behavior of $\approx f^{0.75}$. For the passive method there is a slight deviation at lower frequencies, probably due to noise and the small number of data points.

4.2.5 Nonequilibrium composite networks

The composite network described in the previous section does not have any active force generators. To extend this model to a nonequilibrium system, the motor protein chimera DK4mer was added, which associates to the microtubules.

Concentrations of tubulin and G-actin were the same as in section 4.2.3 and again $4.74 \mu\text{m}$ beads were employed. The DK4mer protein was added together with ATP and MgCl_2 . The protocol is listed in appendix A.4. Due to the aforementioned noise

4. COMPOSITE NETWORKS

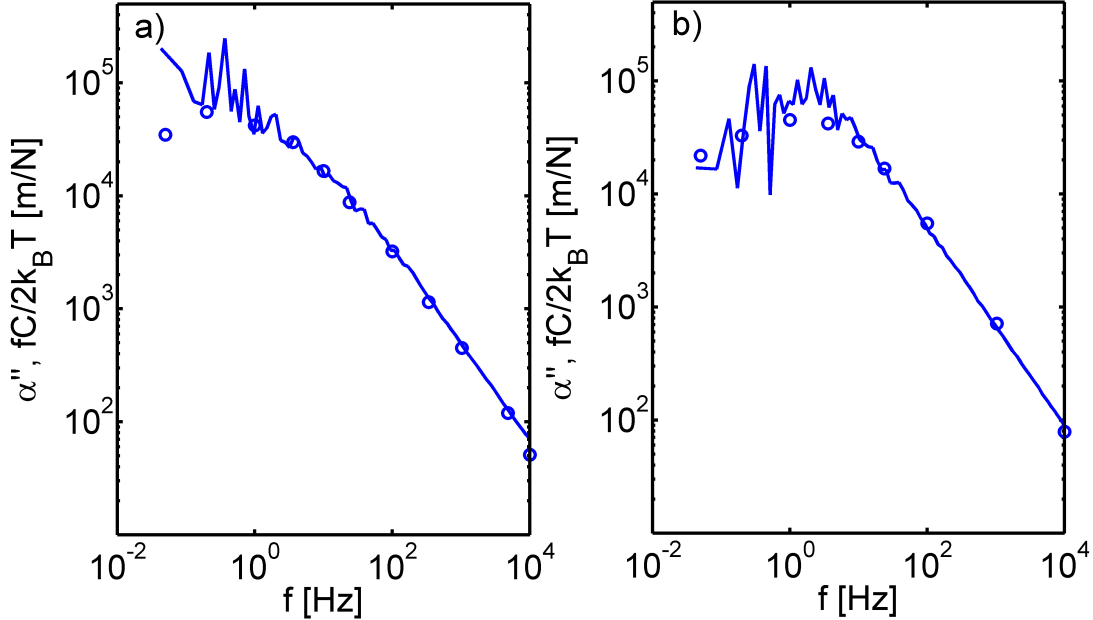


Figure 4.24: Response function of composite with and without motors - In a) the result for the response of the equilibrium composite is plotted. The imaginary part obtained by 1AMR (open circles) agrees with the normalized power spectrum $fC(f)/(2k_B T)$ obtained from 1PMR (line). b) In the network incorporating motor proteins, no deviation between active and passive microrheology could be observed.

limitation of two-particle measurements, only one-particle measurements were carried out.

The imaginary part of the complex response function $\alpha''(f)$ was compared to the normalized power spectrum. A typical result is depicted in figure 4.24. On the left side the results for the equilibrium system are plotted, showing an agreement between active and passive. In b) the system with motor proteins is shown. Here as well, no differences between both methods can be seen, indicating no active fluctuations present, which otherwise would be captured by the 1PMR method. Several reasons may have led to this result:

- The motor is not active in the chosen buffer conditions.
- There is not enough ATP for the motor to become active. The F-actin might have used up all ATP during polymerization or later on by treadmilling.

4.2 Microrheology of cytoskeletal model systems

- The microtubules are too far apart, so that the motor cannot attach and cross-link two microtubules.
- Due to the tight confinement of the microtubules within the F-actin surrounding, the active forces generated by the motors are too small to influence the network properties or their signature is hidden within the low frequency noise.

The activity of the motor protein chimera with respect to the buffer conditions is still under investigation. ATP and MgCl₂ concentrations were chosen to achieve saturating conditions (77). The ATP concentration in the sample was about 4 mMol. The actual ATP turnover rate in our *in vitro* system is unknown. In physiological environments it is usually on the order of $\sim \mu\text{Mol}/(1\text{-sec})$ (63). In our sample chamber with roughly 10 μl , the decrease of ATP concentration is estimated to be on the order of a few μMol per hour. The turnover rate *in vitro* therefore would have to be a thousand times faster to yield a complete ATP depletion within the time frame of our measurements. Nevertheless, it cannot be ruled out that the complex buffer conditions in these composites influence the functionality of the motor.

The material properties of the network itself could hint at the influence of the motor protein. In the case of a completely non-functional motor, the material properties should not differ from those of the equilibrium system discussed in section 4.2.3. From the data of the active measurement the complex shear modulus was computed. In figure 4.25 the storage modulus is plotted versus frequency for the composite in equilibrium and two nonequilibrium networks with varying motor concentration. In the low frequency regime the onset of an elastic plateau can be seen. $G'(f)$ for the networks with motors is higher in magnitude than for the system without DK4mer. Also a higher motor concentration yields an increased stiffness of the sample. At around 100 Hz there seems to be a crossover between the two networks with varying motor concentration. The reason for this is unknown and might be an artifact. Above 1 kHz the data usually drops below zero, which could be the result of the system response correction. Nevertheless, it can be concluded that the motor indeed changes the network properties and must not be considered non-functional. This does not necessarily mean that the motor is actively generating forces. It could also just bind to and cross-link microtubules, which would lead to a stiffer but static network.

4. COMPOSITE NETWORKS

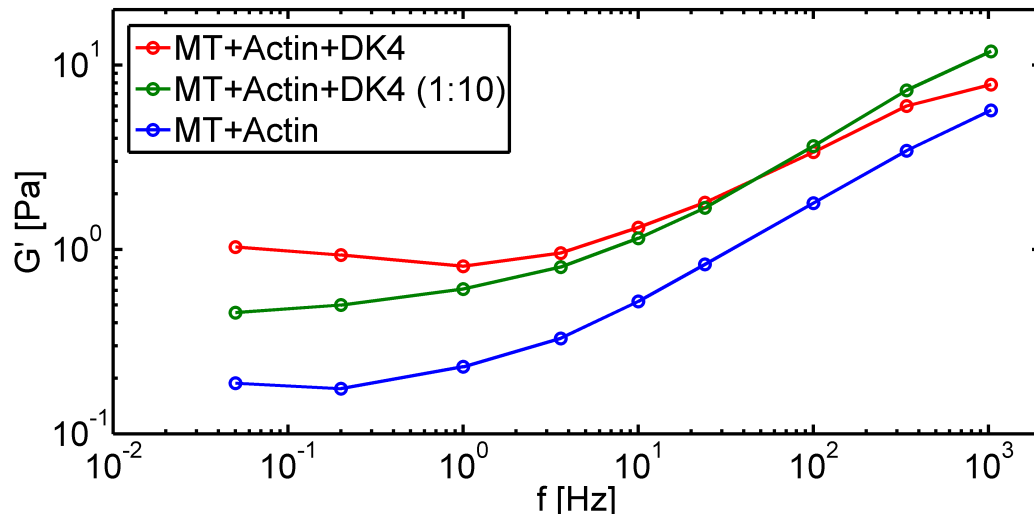


Figure 4.25: Stiffening of the composite in the presence of motor proteins - The storage modulus is plotted versus frequency as obtained from 1AMR. The equilibrium composite exhibits the lowest values for $G'(f)$, with a plateau value of around 0.2 Pa. The composite incorporating DK4mer is about five times stiffer. Decreasing the motor concentration by a factor of ten, yields an intermediate stiffness of about 0.4 Pa at low frequencies.

To investigate the influence of the microtubule density, networks with a higher ratio of tubulin compared to G-actin were prepared. The final concentration of tubulin was set to 1 mg/ml, while the G-actin concentration was lowered to 0.3 mg/ml. Again active and passive one-particle measurements were performed. In only one out of nine different samples prepared in the same manner a deviation between 1AMR and 1PMR was observed. This result is not shown because of the lack of reproducibility. This effect may have also been introduced by small drift in the sample due to, for instance, an imperfect sealing leading to solvent evaporation.

4.3 Discussion and outlook

The experiments presented in this chapter are considered to be preliminary work on the way to a nonequilibrium composite of microtubules, F-actin and motor proteins, mimicking the mechanical properties of cytoskeletal networks. Basic features of semi-flexible polymer networks as a function of monomer concentration were investigated,

in conjunction with the influence of associated motor proteins and cross-linkers.

In section 4.2.1 networks consisting only of microtubules were studied and compared to theoretical predictions. Large variations were observed between the results for samples prepared according to the same protocol. This applies to all networks studied. The two-particle method especially suffers from large variations due to the low signal to noise ratio. In several cases there was an offset between active and passive measurement, whose origin is unknown. This behavior is not observed in simple viscous fluids, in which all the methods have been tested. The magnitude of the response is in both cases obtained from the calibration factor, transforming the data from the measured voltage into a physical unit. This factor was identical for both methods. The correction of the trap stiffness is subject to a systematic error, since it depends on the a priori unknown material properties. But this only influences the measurements at low frequencies, where the motion of the trapped bead is restricted by the trapping potential. The amplitude of the oscillation applied to the bead during the active measurement could influence the data. If the amplitude is too high, a nonlinear response from the material could be obtained. The amplitude for all measurements presented here was a factor of about 50 lower than the bead diameter and is consistent with the amplitude used in prior studies (42). Nevertheless, the influence of the oscillation amplitude on the obtained shear modulus is a parameter which needs further investigation.

The loss modulus of the microtubule networks also displayed a more viscous-like behavior than expected, which is probably due to the formation of a depletion zone around the beads. The two-particle method has been invented to circumvent this problem, since the cross-correlated motion of two beads depends on the material properties of the inter-bead spacing and is therefore expected to be closer to the bulk properties (48). Since the two-particle data is particularly noisy, the results are inconclusive. This effect might be reduced by introducing cross-linkers to stiffen the network.

The addition of motor proteins supports this hypothesis, as described in section 4.2.2, where a cross-linking of the networks by the motors resulted in a power-law behavior close to the theoretical expectation at high frequencies. Additionally, nonthermal fluctuations due to the active force generation of the motor proteins became apparent, manifested in a violation of the FDT. The nonequilibrium networks also showed self-organizational behavior. This led to a very inhomogeneous sample, making a quantitative analysis difficult. Here, addition of static cross-linkers in future experiments could

4. COMPOSITE NETWORKS

prevent superprecipitation, while still allowing the motors to generate forces and apply tensile stress to the filaments.

Composite networks incorporating microtubules and F-actin were prepared and studied using all available methods. Again the two-particle data showed a poor signal-to-noise ratio. The network displayed the typical properties of a semiflexible network. The comparison with single-component networks of microtubules and F-actin respectively revealed material properties similar to those of F-actin networks, suggesting a dominating contribution of the actin filaments to the overall network architecture.

Finally, the nonequilibrium composite did not reveal whether the motor proteins were active or not. A slight stiffening was observed, which suggest at least a passive cross-linking of the network. Since the microtubules in these networks are more tightly confined and also fixed in their orientation with respect to each other, the forces the motors can exert, as well as their run length could be drastically decreased. Therefore, the contribution of the motors' force fluctuations could be very small compared to the dominating thermal fluctuations. Moreover, a closer investigation of the buffer conditions is necessary in future experiments. The ionic strength of the solution has to be carefully adjusted, as well as the supply of ATP. ATP-regenerating systems like phosphocreatine could be used to stabilize the ATP concentration (see for example the supplement of (57)). Microfluidic devices could also be incorporated to yield stable buffer conditions or investigate the influence of environmental changes.

5

Stiff-filament microrheology

The mechanics of cells is dominated by the material properties of the cytoskeleton, which is a very complex protein scaffold consisting of different filaments and accessory proteins (as discussed in section 4.1).

Measuring the cell's mechanics, however still remains challenging. As is described in chapter 3, microrheology can be used to track the motion of micron-sized tracer beads in order to probe the viscoelastic material properties of the surrounding medium.

When applying this technology to networks composed of semiflexible polymers and the cytoskeleton, it has become clear that the micrometer-sized probe particle inevitably introduces a perturbation into the local orientation and assembly of the surrounding network by steric or chemical interactions. If the bead occupies a cavity, the measured material properties can severely deviate from the bulk properties of the surrounding, since the strain field around the particle decays on the length scale of its radius (44, 46). The direct interpretation of conventional microrheology in such systems, which relies on the homogeneous distribution of materials, is therefore not appropriate. Therefore, two-particle microrheology has been invented and has been shown to yield the viscoelastic properties of the material between the two beads (46, 47, 53, 84, 85).

Nevertheless, the insertion of comparatively large particles into the interior of the cell can lead to non-/specific interactions with subcellular structures and significantly alter its mechanics.

To circumvent these problems, a different approach has been developed. Instead of using colloidal particles, one can take advantage of long rigid filaments with a diameter smaller than the mesh size of the surrounding network, which serves as a local probe to

5. STIFF-FILAMENT MICRORHEOLOGY

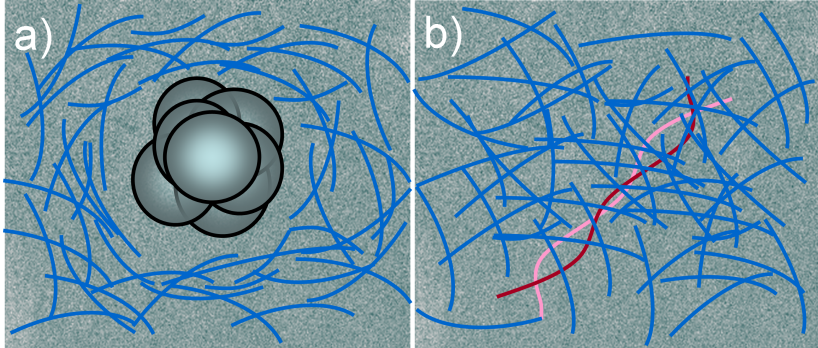


Figure 5.1: Bead versus stiff filament microrheology - In a), standard microrheology using an embedded tracer bead is depicted. b) A long rigid filament serves as a local probe. Its thermal fluctuations are influenced by the surrounding material (indicated as blue lines). Due to the filament's small diameter, perturbations of the network are reduced.

measure the viscoelastic properties of the medium. By analyzing the shape fluctuations of these filaments the material properties of the surrounding can be extracted. A schematic picture is depicted in figure 5.1.

F. C. MacKintosh proposed using microtubules, which have several of the necessary properties for this methodology (86). They have a high aspect ratio with a diameter of only 25 nm but a typical length of tens of microns, which also exceeds the typical mesh size of cytoskeletal networks. With a persistence length on the order of millimeters compared to this length they can be considered as rigid rods (section 4.1.1). Nevertheless, they can exhibit large bending fluctuations. In cells, large buckling of individual microtubules can be observed as shown by Brangwynne et al. (59). They have also investigated their bending dynamics in a non-equilibrium in vitro system (87). As early as 1998, Caspi and coworkers performed video tracking of single microtubules labeled with 300 nm silica beads in an entangled network (88) and obtained their mean square displacement, as well as measured anomalous diffusion with a power-law exponent of $3/4$ due to thermally driven undulations of a single filament. However, the spatial and temporal resolution of video microscopy is limited: finer spatial resolution requires more photons to be counted, i.e. a lower frame rate, whereas high-speed cameras yield a poor positional resolution.

The following section 5.1 shows that the local dynamics of a single spot on a microtubule is sufficient to extract the whole filament's movement, which can then be related to the complex shear modulus of the surrounding. This allows high-resolution

microrheology with an optical trap and the measurement of shear moduli with a frequency bandwidth that is tremendously larger than what is accessible using video tracking of whole filaments.

First results for reconstituted F-actin networks with embedded microtubules have been performed and detailed in the diploma thesis of Felix Zörgiebel (39). The results of further investigations with a variety of filaments of different length are shown in the subsequent section, 5.2.

5.1 Filament bending modes

The equation of motion for the transverse displacement $u(x, t)$ of a rigid rod can be expressed as follows:

$$\kappa \frac{\partial^4}{\partial x^4} u(x, t) + \int_0^\infty \alpha(t - t') u(x, t') dt' - \xi(x, t) - f(t) = 0. \quad (5.1)$$

The first term gives the force per unit length needed to bend a rod with a rigidity of κ perpendicular to the filament axis. The position along the filament contour is denoted by x . The filament is also subject to an external force f and a thermal force ξ . The variable α denotes the viscoelastic memory function for the force at time t due to the displacement of the rod at time t_0 . Inertia is ignored in this equation as well as hydrodynamic interactions between spatially distinct parts of the rod. For a rigid rod it is assumed, that α is a function of time only. For a network of filamentous actin $\alpha \propto \Delta t^{3/4}$ is expected (27).

In Fourier space this equation becomes

$$\kappa q^4 \tilde{u}(q, \omega) + \tilde{\alpha}(\omega) \tilde{u}(q, \omega) - \tilde{\xi}(q, \omega) - \tilde{f}(q, \omega). \quad (5.2)$$

This can be rewritten as a linear response equation

$$\tilde{u} = \tilde{\chi}(q, \omega) \tilde{f}, \quad \text{with} \quad \tilde{\chi}(q, \omega) = \frac{1}{\kappa q^4 + \tilde{\alpha}(\omega)}, \quad (5.3)$$

for the ensemble averaged displacement, where $\langle \tilde{\xi} \rangle_{q, \omega} = 0$. For a homogeneous, incompressible and isotropic medium, α and the shear modulus are related by the drag coefficient of the probe:

$$\tilde{\alpha}(\omega) = \frac{\gamma}{\eta L} G(\omega), \quad (5.4)$$

5. STIFF-FILAMENT MICRORHEOLOGY

with η the solvent viscosity, γ the translational friction coefficient and a filament length of L .

For a straight circular cylinder of radius R with a high aspect ratio $p = L/2R$, the drag coefficient perpendicular to the axis can be expressed as (89):

$$\gamma = \frac{4\pi\eta L}{\ln(\lambda/(2R)) + 0.84}, \quad (5.5)$$

where λ is a characteristic length scale of the bending (i.e., the dominant wavelength). For microtubules in cells Brangwynne and coworkers observed $\lambda = 3 \mu\text{m}$ (59) and with $R = 12.5 \text{ nm}$ this yields $\tilde{\alpha} \approx 2.2G$. The lack of q -dependence is valid provided that $u \ll \lambda$.

The fluctuation-dissipation theorem relates the power spectrum of an observable subject to thermal fluctuations to the imaginary part of the linear response function $\tilde{\chi}(\omega)$ of the system (equation 3.20).

The power spectrum of a whole filament can be calculated as

$$\tilde{C}(q, \omega) = \int_{-\infty}^{\infty} \int_{-\infty}^{\infty} \langle u(x, t)u(0, 0) \rangle e^{-i(qx - \omega t)} dx dt, \quad (5.6)$$

which then is related to the response function via the FDT:

$$\tilde{C}(q, \omega) = \frac{2k_B T}{\omega} \text{Im} [\tilde{\chi}(q, \omega)]. \quad (5.7)$$

The power spectrum of only one point $x = 0$ along the rod is obtained by integrating over all q :

$$\tilde{C}(\omega) = \frac{2k_B T}{\omega} \text{Im} \left[\frac{1}{2\pi} \int_{-\infty}^{\infty} \tilde{\chi}(q, \omega) dq \right]. \quad (5.8)$$

Using 5.3 the integral can be written as

$$\frac{1}{2\pi} \int_{-\infty}^{\infty} \tilde{\chi}(q, \omega) dq = \frac{1}{2\pi} \int_{-\infty}^{\infty} \frac{1}{\kappa q^4 + \tilde{\alpha}(\omega)} dq. \quad (5.9)$$

With the substitution $\zeta^4 = \kappa q^4/|G|$, where $G = |G|e^{-i\phi}$, one can evaluate the integral

$$\frac{1}{2\pi} \int_{-\infty}^{\infty} \tilde{\chi}(q, \omega) dq = \frac{1}{2\pi^4 \sqrt{\kappa} |G|^3} \int_{-\infty}^{\infty} \frac{1}{\zeta^4 + e^{-i\phi}} d\zeta = \frac{1}{2^4 \sqrt{4\kappa}} G^{-3/4}, \quad (5.10)$$

using the physical limits $\phi \in [0, \pi/2]$ for an elastic to a purely viscous medium. For a viscoelastic medium with $G \sim \omega^z$, $\phi = z\pi/2$ and the power spectrum scales as

$$\tilde{C} \sim \omega^{-\frac{3}{4}z-1}, \quad (5.11)$$

corresponding to transverse motion characterized by a mean-square displacement of $\text{MSD} \sim t^{9/16}$ in a semiflexible polymer gel.

Thus, the imaginary part of 5.10 is obtained by calculating the power spectrum of the movement of a single spot on the rigid rod. The real part can then be calculated via the Kramers-Kronig relation (eq. 3.21) and the complex shear modulus of the surrounding medium is obtained.

5.2 Results

Globular actin with a concentration of 0.34 mg/ml was used to form an entangled network of filamentous actin, in which sparsely distributed microtubules with an attached gold bead were embedded. The exact protocol can be found in the appendix A.5. Fixing a bead to the filament might change the dynamical properties of the system. But since their diameter of 40 nm is less than two times the microtubules diameter and 300 nm beads were successfully employed in (88), the influence should be negligible.

The beads were visible in DIC-mode, however the microtubules were difficult to resolve. To get a valid estimate of the filament's length and exclude those attached to another filament, the microtubules were also observed in fluorescence mode employing rhodamin-labeled tubulin. Microtubules which were significantly smaller than 10 μm , exhibited a large tilt with respect to the focal plane or with the bead attached close to the end, were excluded from measurement.

To avoid large forces on the beads, which could cause defects in the network, the trap was not turned on until the beads were positioned to focus position in the focal plane. The laser power was lowered to give a trap stiffness on the order of a few hundred femtonewton per nanometer. This was done to reduce the influence of the trapping potential which is not included in the theoretical description from section 5.1. Attempts at calculating a generalized Langevin equation including a harmonic potential have recently been proposed by Bullerjahn et al. (90).

A total of 17 microtubules with 21 gold beads were tracked using back-focal-plane interferometry (see section 2.3). Some microtubules happened to have several beads attached to them at different positions. Most of the microtubules had a length between 10 and 35 μm ; the shortest was 8 μm , the longest 75 μm . Three million data points per channel (x and y) were recorded at a sampling frequency of 195 kHz, corresponding

5. STIFF-FILAMENT MICRORHEOLOGY

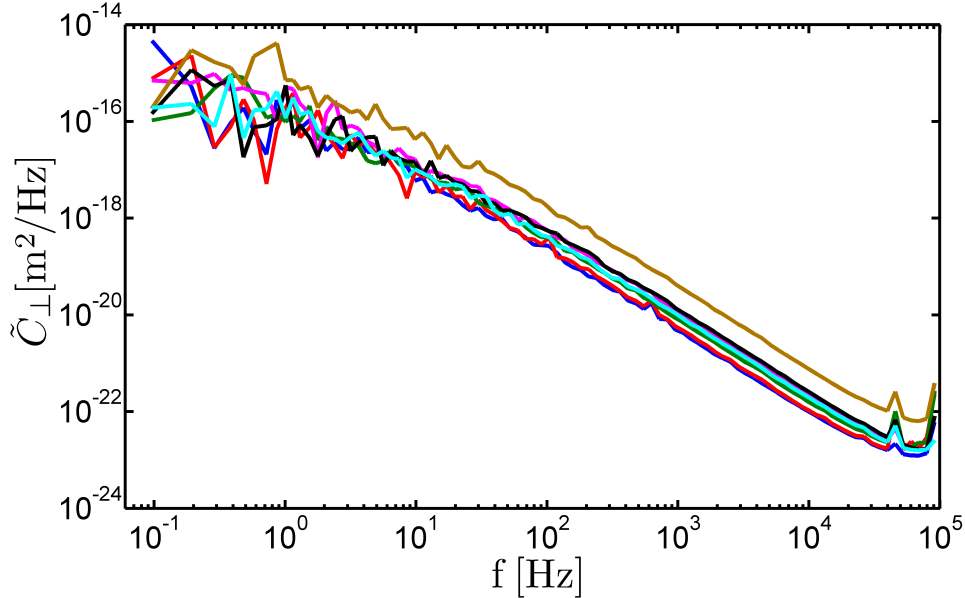


Figure 5.2: Example of power spectra for one microtubule - Calculated power spectral densities of a 21 μm microtubule. The position fluctuations of the tracer bead were measured seven times. The power law behavior is reproducible and only a small variation in the amplitude occurs.

to a measurement time of about 15 seconds. This short time interval was chosen to avoid large scale movements of the filament-bead system, with which it might leave the linear regime of the trapping potential or completely drop out of the laser focus. 59 independent measurements were taken altogether. All experiments were performed at room temperature ($T = (21 \pm 1)^\circ\text{C}$).

To match the coordinate system of the QPD, the recorded x/y-data was rotated according to the angle determined from the fluorescence images of the microtubules. This way, the movement of the bead parallel and perpendicular to the filament’s axis was saved in separate measurement channels. The data was then transformed from voltage to length by multiplying with the according calibration factor obtained “offline” by trapping several gold-beads in water at a height above the coverslip corresponding to that of the measurement (see also section 2.4 for details on the trap calibration procedure). The power spectral density for each channel was then calculated numerically and logarithmically binned.

An example of 7 repeated measurements on a bead attached to a microtubule with

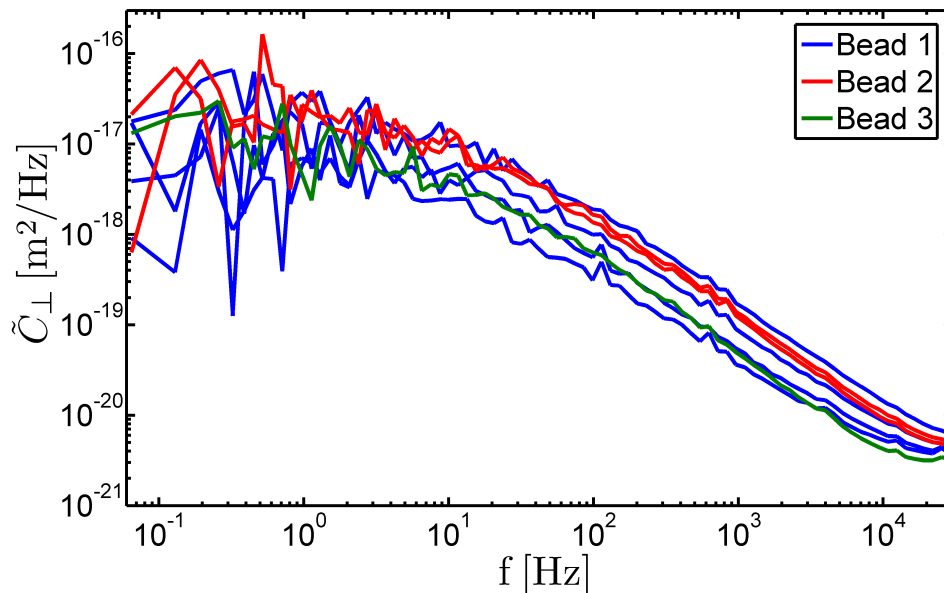


Figure 5.3: Power spectra for different beads on the same microtubule - Three beads on a $34\ \mu\text{m}$ microtubule separated by several micrometer where repeatedly measured. The power-law is comparable, but the amplitude shows larger variation.

$L = (21 \pm 2)\ \mu\text{m}$ is shown in figure 5.2, where the power spectral density is plotted versus frequency. Below 10 Hz the PSD is noisy due to the short measurement time and there are therefore few data points in this regime. The bead also exhibits large excursions of up to 200 nm peak-to-peak inside the trapping focus. Up to about 30 kHz the PSD scales very reproducibly with a power law f^{-z} . At higher frequencies characteristic peaks show up which could later be traced back to the acousto-optical deflector in the beam path. The data is therefore only shown up to that frequency in the following plots. There is some ambiguity in the amplitude of the PSD, probably also due to the large fluctuations of the bead in the trap.

There are also variations between measurements of different beads on the same microtubule. Figure 5.3 displays the results for three different beads separated by several micrometers on a $(34 \pm 2)\ \mu\text{m}$ microtubule. The measurements for the different beads, but also those for the same bead again, show variations in amplitude for the reasons mentioned before. Polydispersity of bead diameter could also play a role.

When analyzing the information present in the power spectrum, care has to be taken concerning the different frequency regimes. For a filament with finite length,

5. STIFF-FILAMENT MICRORHEOLOGY

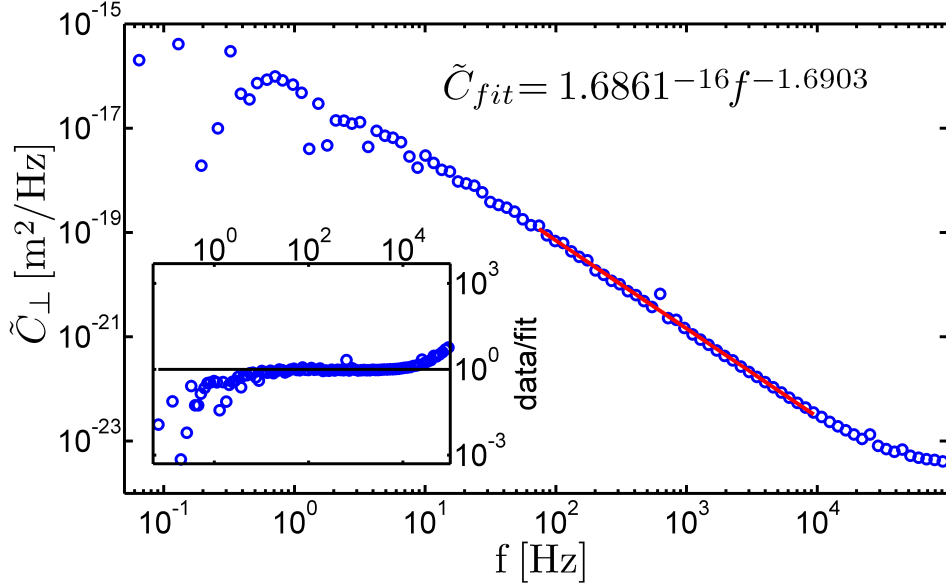


Figure 5.4: Least squares fit of a power spectrum - After calculating the PSD, a linear fit is performed in a log-log plot. The fitting range is indicated by the red bar, ranging from 50 Hz to 10 kHz, where the PSD follows a power-law. The inset shows the quotient of data and fit.

bending only occurs on time scales shorter than the relaxation time of the bending mode with the longest wavelength.

The relaxation time can be approximated by (66):

$$\tau_n \cong \frac{\gamma}{\kappa q_n^4}, \quad (5.12)$$

where κ is the rigidity, $q_n = \frac{\pi(n+1/2)}{L}$, $n \in \mathbb{N}$, are the mode wavelengths and γ is the perpendicular drag coefficient as given by equation 5.5, which depends on the filament length. The theoretical prediction is therefore only valid for frequencies higher than f_1 . Brangwynne et al. found a persistence length of between 1.5 and 2.8 mm for microtubules between 18 and 66 μm (68), with a slight dependency on the filament's length, which could also be explained by the noise-limitation. Using an average of 2 mm and calculating the bending rigidity as $\kappa = l_p k_B T$, the cross-over frequency lies between 217.6 Hz for the shortest and 0.1 Hz for the longest investigated filament.

This frequency dependence will affect the Kramers-Kronig relation in obtaining the real part of the complex response function. Also the contribution of the optical

trap at low frequencies cannot be neglected. Hence, to obtain the shear modulus of F-actin, another approach is selected. The shear modulus is assumed to be of the form $G = A(-i\omega)^z$ for a viscoelastic material. This corresponds to a power spectral density of $\tilde{C} = B\omega^m$. Using equation 5.10 the constant B can be calculated to

$$B_{\perp} = \frac{k_B T \sin(\frac{3\pi}{8}z)}{\sqrt[4]{4\kappa}} A^{-\frac{3}{4}}, \quad (5.13)$$

for the power spectrum of the motion perpendicular to the filament axis. The exponent m becomes

$$m_{\perp} = -\frac{3}{4}z - 1. \quad (5.14)$$

Both constants were obtained from the measured spectra by fitting a linear function in a log-log plot in a least squares manner. An example is shown in figure 5.4.

Below f_1 , the filament's motion should be dominated by viscous drag. The ratio of the power spectral densities parallel and perpendicular to the filament axis reduces to the ratio of the drag coefficients of a rigid rod, whereas for high frequencies one would expect a power-law behavior (39, 89):

$$\frac{\tilde{C}_{\parallel}}{\tilde{C}_{\perp}} \approx \text{const} \approx 1.7 \quad \text{for } f < f_1, \quad (5.15)$$

$$\frac{\tilde{C}_{\parallel}}{\tilde{C}_{\perp}} \propto \omega^{-z/4} \quad \text{for } f > f_1. \quad (5.16)$$

The ratio of the power spectra for all measured microtubules is plotted in figure 5.5. For better clarity the filaments have been roughly grouped and color-coded according to their length around 10, 20 and 30 μm . Each line is the average over all measurements performed on the corresponding microtubule.

For frequencies below 10 Hz the spectra are dominated by noise and no clear statement can be made about the behavior in this regime. The expected cross-over can therefore not be verified. At higher frequencies the ratio is mostly constant in the logarithmic plot. Only the longest microtubule displays an increase up to around 2 kHz. Concerning the amplitude, there is no clear trend observable, only a slightly higher variance with increasing filament length.

The values for the constants of proportionality for the PSD ratio $\frac{\tilde{C}_{\parallel}}{\tilde{C}_{\perp}} = \frac{B_{\parallel}}{B_{\perp}}\omega^{m_{\parallel}-m_{\perp}}$ are listed in table 5.1. As can be seen the exponents of the parallel and perpendicular power spectrum are nearly equal. All values show large errors. For F-actin $z = 3/4$ and

5. STIFF-FILAMENT MICRORHEOLOGY

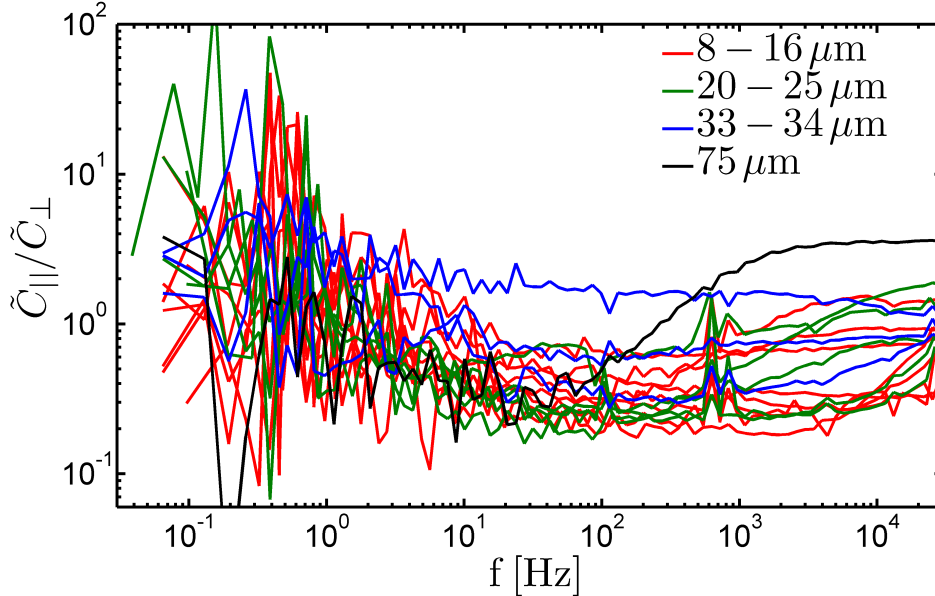


Figure 5.5: Ratio of parallel and perpendicular power spectra - The ratio was computed and plotted for all measured microtubules. For clarity the microtubules were grouped and color-coded into intervals of length around 10 (red), 20 (green) and 30 μm (blue), as shown in the legend. The longest microtubule with $L = 75\mu\text{m}$ is shown in black. The ratio is roughly constant over the whole frequency range for most of the measured microtubules.

therefore $\frac{\tilde{C}_{\parallel}}{\tilde{C}_{\perp}} \propto \omega^{-3/16}$ is expected. This is not fulfilled for microtubules around 10 μm and even for the longer ones there is a deviation of more than 60 %.

By averaging all values for B_{\perp} and m_{\perp} obtained from the fitted power spectra, the constants A and z of the complex shear modulus were calculated. Using equation 4.3 and ignoring the high frequency part, the theoretical expected shear modulus can be calculated. The bending rigidity of F-actin is $\kappa = 6.88 \cdot 10^{-26} \text{ Nm}^2$ (68), the filament density is $\rho = 1.29 \cdot 10^{13} \text{ m}^{-2}$ (27) and the drag coefficient $\gamma = 2.3 \cdot 10^{-3} \text{ Ns/m}^2$. This leads to

$$G_{theo}(\omega) = A(-i\omega^z) \approx 0.13(-i\omega)^{0.75}. \quad (5.17)$$

From the measurement we obtain

$$G_{meas}(\omega) \approx (23.6 \pm 35.4)(-i\omega)^{(0.92 \pm 0.11)}. \quad (5.18)$$

The amplitude is about 200 times higher than expected showing a large error bigger than the mean value and exceeding the physical range. The exponent deviates

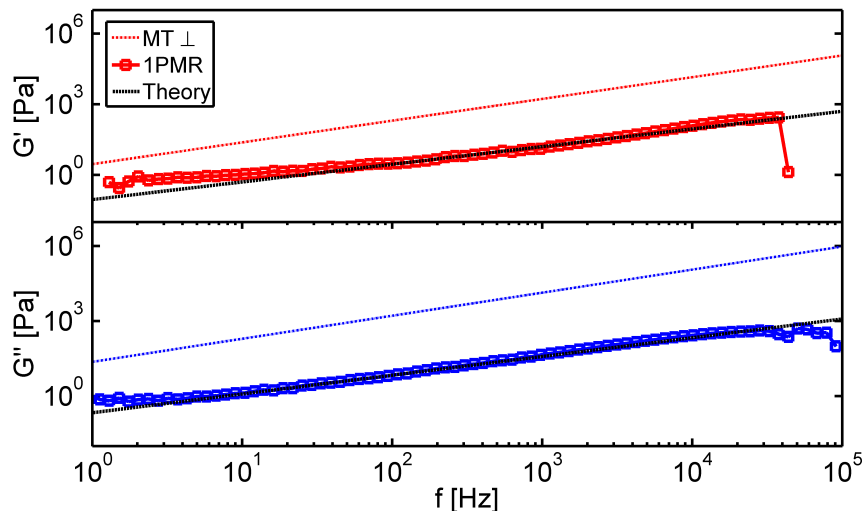


Figure 5.6: Shear modulus of F-actin - The black dotted line indicates the theoretical progression of the shear modulus as computed by 4.3. The dotted curves show the real (red) and imaginary part (blue) of the shear modulus obtained by fitting the power spectra of the gold beads' fluctuations perpendicular to the microtubule axis. For comparison a 1PMR measurement using $1\ \mu\text{m}$ silica beads is shown as circles.

about 20% from the theoretical value, whereas the standard deviation is only 12%.

This result is plotted in figure 5.6 together with a standard particle microrheology measurement for comparison. Only the longest microtubule with $L = 75\ \mu\text{m}$ delivered results close to the expectation: $A \approx 0.66\ \text{Pas}^{3/4}$ and $m \approx 0.74$.

MT length [μm]	B_{\parallel}/B_{\perp}	$m_{\parallel} - m_{\perp}$
8-16	0.73 ± 2.22	0.01 ± 0.16
20-25	0.41 ± 0.92	0.12 ± 0.21
33-34	0.34 ± 0.56	0.11 ± 0.15

Table 5.1: Ratio of power spectra - The constants of proportionality of the power spectral density ratios. Rows show the lengths in which the microtubules were grouped. The average was taken between 50 Hz and 10 kHz for each group.

5.3 Discussion

The measured values for the complex shear modulus of the solution of F-actin used in the experiments deviate considerably from the theoretical expectation, and also the small difference between the PSDs parallel and perpendicular to the filament's axis is puzzling. First of all, the prefactor A is much higher than expected and has a large error. Several reasons could account for this:

During the experiments it was impossible to ensure that the beads were exactly in the focus of the trap. Analyzing the raw data indeed shows large-scale fluctuations in x and y , and presumably this also applies to the z -coordinate, which was not recorded. This means that the diode's response to the attached bead's displacement could be different from the response that is measured for the particles in water during the calibration. Polydispersity of the bead size could also lead to errors either during the calibration or the measurement. The gold beads employed had a relatively broad size distribution in the range of 20 to 60 nm. Rotational movement of the filament and the attached gold bead relative to the microtubule's axis is also possible. A rotational motion around the axis of an otherwise stationary filament would appear as a lateral movement in the projection scheme of the two-dimensional detection system. Therefore, a significant cross-talk could occur, which would lead to an overestimation of the bead's, and therefore the filament's, fluctuations. This could also explain the deviations in the power-law exponent. Lastly, local inhomogeneities in the F-actin concentration cannot be ruled out.

The measured exponent of the shear modulus' frequency dependence is more difficult to explain. In reference (88) the correct value has been obtained using a similar approach. Using a tracer attached to the filament should therefore be sufficient to observe the filament's motion and not introduce any artifacts. The measured frequency range was limited to 10 Hz in their experiments. In this regime our data is too noisy to extract the exponent in a meaningful way. For higher frequencies one would still expect the same power-law behavior. The onset of viscous behavior with $G \propto \omega$ as implicit in equation 4.3 should not occur in the kHz regime. The frequency ω_{visc} at which both terms in equation 4.3 become equal can be calculated as:

$$\omega_{visc} = \frac{8\rho^4\kappa^5\gamma^3}{(15k_B T\eta)^4}. \quad (5.19)$$

This does depend on the bending rigidity κ and therefore the persistence length of F-actin, which has been experimentally verified (see for example (66, 68, 91, 92)) and has a value of $l_p \approx 17 \mu\text{m}$. The drag coefficient was estimated to be $\gamma = 2.3 \cdot 10^{-3} \text{Ns/m}^2$ in (27), and the density of filament length scales linearly with the concentration, with $\rho = 3.8 \cdot 10^{13} \text{m}^{-2}$ for 1 mg/ml of polymerized F-actin (93). For the 0.34 mg/ml solution used in the experiments we obtain $\omega_{visc} \approx 3.1 \cdot 10^8 \text{Hz}$. This is depicted in figure 5.7, where the viscous part of the shear modulus is plotted for different concentrations. Even if a ten times lower concentration of F-actin is assumed, due to incomplete polymerization for instance, the viscous cross-over occurs at $3.1 \cdot 10^4 \text{Hz}$, still at the far end of our measurement. At this or at lower concentrations no entangled network could be formed, in contrast to the observation of tightly confined microtubules during the experiments.

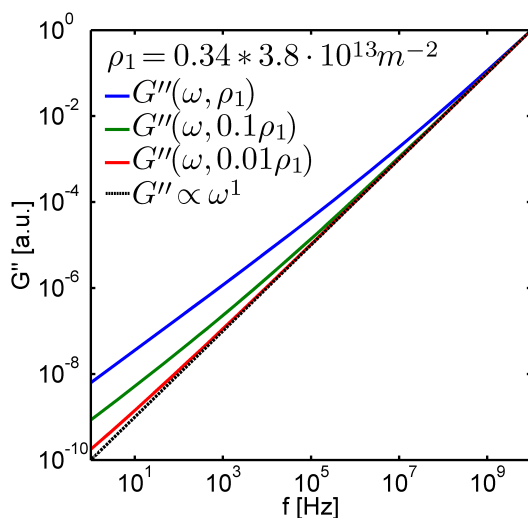


Figure 5.7: Viscous cross-over - The theoretical expectation for the loss modulus of F-actin is plotted for several concentrations. The black dotted line indicates pure viscous scaling $\propto \omega$. For the concentration used in the experiments, $c_{exp} = 0.34 \text{ mg/ml}$, G'' shows a cross-over in the MHz regime (blue line). The cross-over occurs in the kHz regime for a $10\times$ lower concentration (green line) and again a factor of 10^4 lower for $0.01 \cdot c_{exp}$ (blue line). All lines are plotted to collapse at $G'' = 1$.

Another crucial point is the attachment of the gold bead to the microtubule. If the bead's movement were to largely decouple from that of the filament, only the bead's response to the surrounding would be measured. Due to its small size, smaller than the mesh size of F-actin, this would most likely approach the solvent's viscosity. Nevertheless, the biotin-streptavidin bond is one of the strongest non-covalent bonds in nature (94) and has a linker length of only 2.5 nm (95). This is not expected to behave as a weak and flexible bond damping the transfer of the filament's fluctuations to the tracer bead.

5. STIFF-FILAMENT MICRORHEOLOGY

The influence of rotational motion has already been mentioned. A movement of the tracer bead around the filament would lead to an overestimation of the bead's and thereby the filament's fluctuations. Such a motion cannot be ruled out and was difficult to resolve in the microscope. But there is no estimate of the time scale on which such a behavior could occur and its influence on the power spectrum.

A further factor is the length of the measured microtubules. The theoretical description as presented in section 5.1 assumes infinitely long filaments. But in principle the real filament's response should not drastically deviate from the expectation as long as it exceeds the typical mesh size of the surrounding network (about 500 nm for the used concentration of F-actin (eq. 4.4)). Nevertheless, the measured filaments had a length of only a few tens of μm and the longest filament actually displayed the expected behavior. Caspi et al. used microtubules with length of more than a hundred micrometers (88), hence an influence from the filament length must be considered.

5.4 Conclusions and outlook

The use of long rigid filaments as local probes up to now does not yield the expected results for the material properties of the surrounding. In future, further experiments have to be performed to explore the applicability of this method. Investigating the length dependence of the results should be one of the first tests. To reduce the large scale fluctuations of the tracer bead, a higher trap stiffness can be employed, but then this influence has to be taken into account in the theoretical description, for example along the lines of (90). Otherwise some feedback mechanism has to be implemented into the trapping setup to keep the bead's position close to the center of the trap. This would allow longer measurements and the behavior on a broader time scale could be analyzed. Another parameter that should be investigated, is the concentration of G-actin and the resulting filament density after polymerization.

To use this method intracellularly, the origin of the observed discrepancies has to be determined. Also some technical issues remain challenging. The gold beads have to be introduced into the cells and then attached only to microtubules. Tracing the beads' motion in the crowded environment of a cell could also be difficult, as microtubules in a cell not only have a broad distribution in length, but also constantly assemble and disassemble. Last but not least the cell is a nonequilibrium system where the FDT does

not hold. Hence the passive observation of the tracer movement has to be accompanied by an active measurement which takes much longer to perform.

To develop this method into a full-fledged microrheology technique, these obstacles have to be overcome.

5. STIFF-FILAMENT MICRORHEOLOGY

6

Intracellular measurements

The measurements described so far have been performed in reconstituted networks *in vitro*. The results of such model system have to be compared to experiments performed inside of cells to determine their validity.

In the following sections, first results from an intracellular measurement are described, which was performed using the new microrheology setup. COS-cells were studied with one-particle active and passive microrheology (see appendix A.6).

6.1 Measurements in COS-cells

COS-cells were spread on a fibronectin-coated coverslip and 200 nm silica beads were injected into about 40 cells. Three different cells with beads were found in the sample. A typical image is shown in figure 6.1. Close to the cell nucleus, the density of beads was higher compared to the rim. The beads appeared about two times larger than in water. This might either be due to layers of lipid surrounding the beads, the refractive index difference between the beads and the cytoplasm, or that the observed objects were actually intracellular organelles like lipid vesicles. Cells without beads could not be observed due to the limited range of the positioning stages. The cells spread over a large area, resulting in a thickness of only a few micrometers. Several beads underwent active transport, i.e. sudden movements of a few micrometer in a straight line. The beads otherwise exhibited fluctuations around a roughly constant position. The observation of active transport ensured that the beads in this focal plane were actually inside the cell and not lying on top of or below of it.

6. INTRACELLULAR MEASUREMENTS

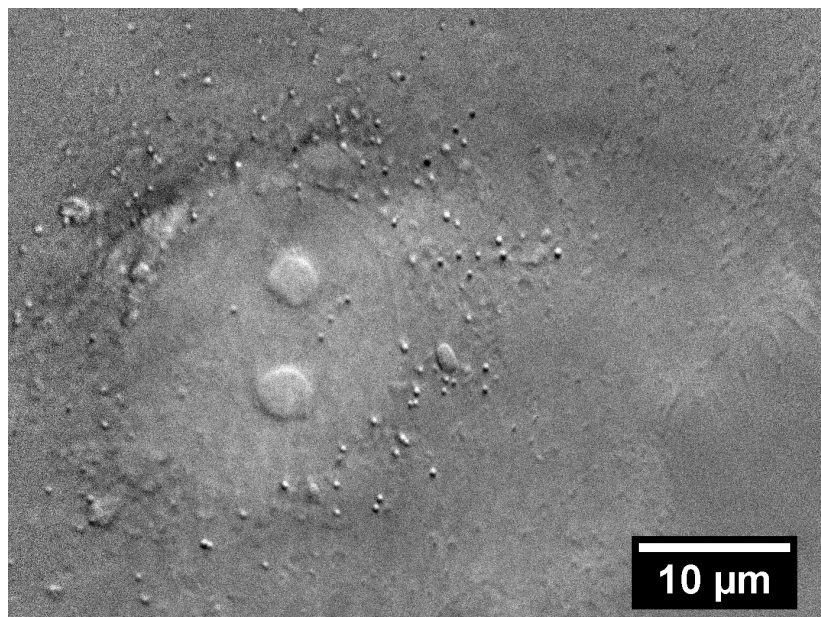


Figure 6.1: Microscope image of a COS-cell with injected beads - The cell spreads over the whole field of view (about $40 \times 55 \mu\text{m}$). The cell contour is visible in the lower right, the cell nucleus to left of the center. Spherical objects of varying size are distributed over the cell, with a slightly higher density around the nucleus. The cell's thickness was about $4 \mu\text{m}$.

A total of nine different beads in two different cells were measured using 1PMR. On six of them an active measurement was performed as well. The trap stiffness was kept low so as not to apply too much stress on the beads' surrounding. To account for the unknown material properties and the polydispersity of the bead diameter, the scanning-calibration procedure described in section 2.4 was applied for both probe and drive laser.

6.2 Results

The QPD-signal of the beads was in general very weak, due to the small index difference between silica and the cytoplasm. Because of the low trapping power, the beads might not have been in focus or in the linear regime of the trapping potential. This lead to large variations in the measured data. The scanning-calibration did not yield the proper response curve needed to obtain the calibration factor. This is probably due to the difficulty of positioning the small beads in focus and the low signal-to-noise

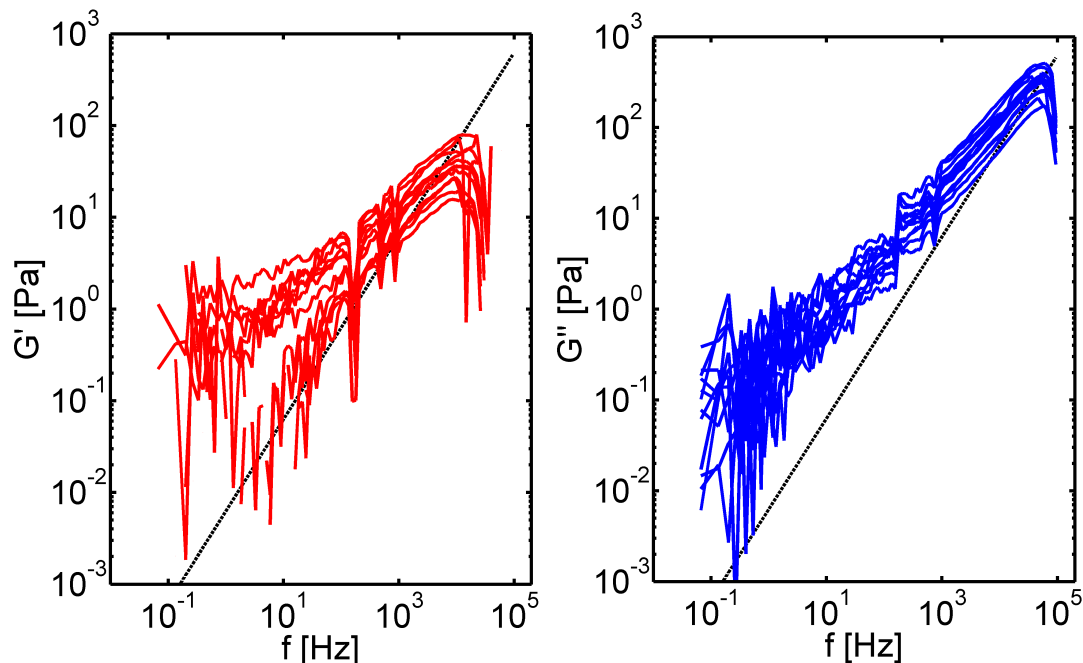


Figure 6.2: Intracellular shear moduli obtained from 1PMR - The shear modulus was calculated from the position fluctuations of several beads at different locations inside the cell. Due to the systematic errors introduced by the calibration procedure and the varying bead size, the data shows poor reproducibility. The viscous part scales with a power-law of about $\sim f^{0.7}$, as obtained from a fit to the high-frequency part (data not shown).

ratio. Therefore, a calibration on several beads in water was performed to obtain an average calibration factor. This also gave the trap stiffness, which cannot be obtained for the beads inside the cell. The absolute values derived by using these parameters may therefore deviate systematically from the correct values inside the cell.

The complex shear modulus for all individual 1PMR measurements is plotted in figure 6.2. As expected from the error-prone calibration parameters, the data varies over several orders of magnitude and can only be interpreted qualitatively. The storage modulus in particular shows the effect of an erroneous trap correction at low frequencies, besides the possible violation of the FDT in the nonequilibrium environment. Several peaks in the spectra indicate external noise, whose origin could not be found during the limited time segment of the measurement. All measurements display a power-law of about $\sim f^{0.7}$. This is close to the expected value for a semiflexible polymer network.

6. INTRACELLULAR MEASUREMENTS

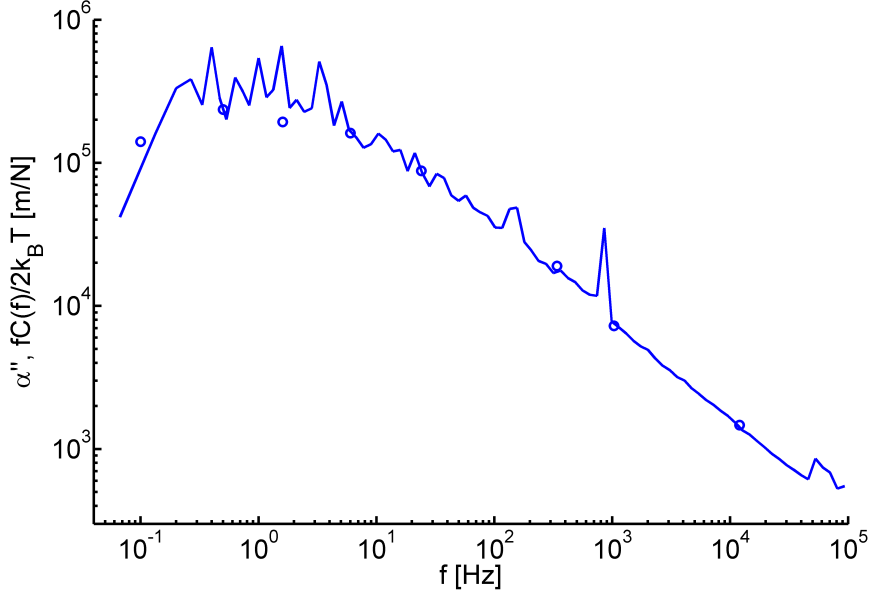


Figure 6.3: Imaginary part of the intracellular complex response function - Active and passive measurement performed on an injected bead agree over the whole frequency bandwidth. No deviations at low frequencies are apparent.

The imaginary parts of the complex response function as obtained from 1PMR and 1AMR were compared and analyzed for signs of athermal fluctuations. For none of the six active measurements could a deviation between 1AMR and 1PMR be observed, or the noise at low frequencies was too large to make any reasonable statement. A typical example is shown in figure 6.3. This result is somewhat unexpected, since the cell is a nonequilibrium system and signs of active force generation were seen in terms of active transport of beads. The force generation of the cell might be quite small due to the large spread on the coverslip. Therefore nonthermal fluctuations might be hidden in the noise limit.

6.3 Discussion and outlook

The results so far are only preliminary, and the experiments served, among other things, as a test to find the optimal parameters for future measurements. The bead size is quite small, making it difficult to position them in the focus. 500 μm beads should be used in the future. Also the beads' material should have a higher index compared to the

surrounding, to increase the QPD-signal over the background noise. Polystyrene beads could be employed, but they are more difficult to trap in water, which is necessary for the determination of the trap stiffness.

A higher trap stiffness could be used for the driving laser to keep the beads close to the linear regime of the trap and achieve a better signal-to-noise ratio, but this might also introduce defects into the cytoskeleton.

The cell substrate should also be changed to prevent massive spreading of the cells. When reproducible measurements are achieved, the cell's material properties at different locations in the cytoskeleton can be compared. In the long term, the cells' response to different drugs targeting the cytoskeleton could also be investigated.

6. INTRACELLULAR MEASUREMENTS

7

Summary and outlook

The intriguing mechanical properties of complex fluids like cytoskeletal networks were the focus of this thesis. The challenge has been tackled from two sides.

On the technological side, a new compact, versatile microrheology setup has been constructed, employing state-of-the-art technologies like electro-optical deflectors. The setup is a multi-purpose device specifically designed for high-bandwidth one- and two-particle active and passive microrheology. The accessible frequency range was extended to 200 kHz and is currently limited by the EOD-drivers and the acquisition electronics. In principle, bandwidths of up to 1 MHz are possible in the future. Three different wavelength can be chosen to create two laser traps, which are independently steerable with high precision. DIC- and fluorescence illumination are both possible for imaging biological samples.

In the future, the handling of the setup will be improved to make the alignment easier. An active force- and position feedback could also be implemented, and the computer-control will be extended to allow an automated calibration procedure during the experiments. To reduce the noise limit to even lower frequencies, a more stable laser source has to be used and/or an active mechanism to reduce beam pointing instability must be implemented.

On the experimental side a variety of cytoskeletal networks has been investigated. Starting from simple single-component networks and going to composites made of F-actin and microtubules, their shear moduli have been calculated and compared. Adding motor proteins to microtubules resulted in self-organized structures and a violation of the fluctuation-dissipation theorem in the experiments. These preliminary

7. SUMMARY AND OUTLOOK

results are the basis for further investigations of networks of various compositions. The influence of parameters like the bead size, bead distance in two-particle experiments as well as the comparison to conventional microrheology could be studied in subsequent experiments.

The basis for a new experimental technique using stiff filaments as local probes to study the viscoelasticity of semiflexible polymer networks has been laid out. So far, the method suffers from technical limitations, which have yet to be overcome. In the future, the potential of the method for intracellular measurements has to be evaluated.

A preliminary test experiment using COS-cells has been performed and gave qualitative results about the material properties of the cytoskeleton. In the long term the response of cells to different environmental conditions can be studied with all the available microrheology techniques. This will yield further insight into the complex behavior of cellular materials.

Appendix A

Biochemical protocols

A.1 Microtubule preparation

Tubulin was prepared from porcine brain and fractions were biotinylated or labeled with rhodamin according to standard protocols. Aliquoted stocks were stored at -80°C and thawed just before sample preparation.

Tubulin was polymerized at a concentration of 4 mg/ml in the presence of BRB80 buffer (80 mM K-PIPES, 1 mM MgCl_2 , 1 mM EDTA, pH 6.8), together with 1 mM GTP, DMSO (5% of volume) and MgCl_2 (10 mM) for about 15 min at 37°C . For fluorescence images rhodamin labeled tubulin was incorporated in a ratio of 1/4 with unlabeled tubulin. Polymerized microtubules were diluted into BRB80 buffer to the desired concentration, containing paclitaxel to 1% of volume. Anti-bleach reagents (10 μM glucose, 2 mM MgCl_2 , 0.1 mg/ml glucose-oxidase, 80 μM catalase, 10 mM DTT) together with 4.74 μm plain silica beads (Bangs Laboratories, Inc., Fishers, IN, USA) were added and the solution was gently mixed. In case of cross-linking, biotinylated tubulin was added to one tenth of the tubulin concentration.

A.2 Actin preparation

Actin was prepared from chicken skeletal muscle according to standard protocols and stored at -80°C in G-buffer (2 mM Tris-Cl, 0.2 mM CaCl_2 , 0.5 mM DTT, 0.2 mM ATP, pH 7.5).

G-actin was diluted into F-buffer (1 mM Na_2ATP , 2 mM HEPES, 1 mM EGTA, 2 mM MgCl_2 , 50 mM KCl) to the desired concentration. Beads were added and the

A. BIOCHEMICAL PROTOCOLS

solution was directly infused into the sample chamber. Polymerization took place at room temperature for about 30 minutes.

A.3 Microtubules and DK4mer

Microtubules were prepared according to the recipe in A.1. Due to the small yield of the purification of the DK4mer, the concentration could not be measured. It was however roughly estimated to 100 $\mu\text{g}/\text{ml}$ from gel electrophoresis.

The motor proteins were added to the microtubule solution, first at 5% volume fraction, later 2%. 4 mM ATP and 4 mM MgCl_2 were added, corresponding to saturating conditions for the motor's velocity (77).

A.4 Preparation of composite networks

For the composite network, G-actin and F-buffer, together with beads, were added to the polymerized microtubules. The microtubule solution was chosen to yield either 0.67 or 1 mg/ml. F-buffer was added to a volume fraction of 1:6 of the final solution. Actin was diluted into this solution to yield either 0.57 or 0.28 mg/ml. A volume fraction of one seventh was reserved for beads, cross-linkers and, in case of active networks, for motor proteins and additional ATP and MgCl_2 , which were diluted into BRB80.

For the nonequilibrium network, motor proteins were added to a final concentration of 0.2 $\mu\text{g}/\text{ml}$ or 0.02 $\mu\text{g}/\text{ml}$ respectively. ATP was added to 4 mM and MgCl_2 to 7 mM (including the ATP and MgCl_2 already present in the F-buffer). For cross-linked networks neutravidin was added to a final concentration of 0.1 mg/ml.

A.5 Labeling of microtubules with gold beads

To measure the motion of one point along a microtubule with the optical trap, a small gold bead has to be bound to the filament. This is achieved by a biotin-streptavidin bond. This bead should be placed roughly in the middle of the microtubule to reduce the influence of boundary effects occurring at the ends of the filament. Bundling of several microtubules around one bead is also undesirable. Therefore, only a small fraction of the microtubule is to be labeled with biotin. The other parts should be made of fluorescently or unlabeled tubulin.

Biotinylated and rhodamin labeled tubulin was first polymerized at a concentration of 1.6 mg/ml in a ratio of 4:1 in the presence of 0.8 μ M GMPCPP at 37° C for 15 minutes, yielding small seeds for further polymerization. A 1:1 mixture of rhodamin and unlabeled tubulin at a concentration of 1 mg/ml was then added and polymerizing in the presence of 1 mM GTP and MgCl₂ for 25 minutes. The polymerized microtubules were stabilized with 10 μ M paclitaxel.

A.5.1 Embedding labeled microtubules in F-actin

The final actin solution containing sparsely distributed microtubules (440 ng/ml tubulin) were polymerized from 0.34 mg/ml G-actin at room temperature in actin polymerization buffer (1 mM Na₂ATP, 2 mM HEPES, 1 mM EGTA, 2 mM MgCl₂, 50 mM KCl). Streptavidin-coated gold beads (40 nm diameter, BioAssay Works, Ijamsville, MD, USA), anti-bleach reagents (10 mM DTT, 4 mM MgCl₂, 20 mM glucose, 0.1 mg/ml GOx, 80 μ g/ml catalase) were added. The solution was gently mixed to ensure a homogeneous distribution of microtubules in the network. Actin polymerization sets in directly after mixing, thereby drastically slowing down the mobility of microtubules. The gold beads, due to their size smaller than the typical mesh size of the entangled F-actin solution, were able to diffusive through the network, eventually attaching to the biotin-site of an embedded microtubule. Measurements were performed between one and two hours after sample preparation.

A.6 Cell culture

COS-7 fibroblast cells derived from kidney cells of the African green monkey were obtained from the Leibniz-Institut - Deutsche Sammlung von Mikroorganismen und Zellkulturen (DSMZ) GmbH, Braunschweig, reference number ACC 60.

The cells were cultivated in Dulbecco's modified Eagle's medium (DMEM) with 1000 mg/L glucose, L-glutamine, and sodium bicarbonate (D6046; Sigma-Aldrich, St. Louis, MO, USA), 1% Penicillin/Streptomycin (17-602E; Lonza Group Ltd., Basel, Switzerland) and 10% FBS (F2442; Sigma-Aldrich).

200 nm plain silica beads (PSi-0.2; Kisker Biotech GmbH & Co. KG) were injected using a microinjector (FemtoJet express; Eppendorf AG, Hamburg, Germany).

A. BIOCHEMICAL PROTOCOLS

Appendix B

MATLAB-programs

This section contains a list of MATLAB-programs which have been written to extend the functionality of the Microrheology Toolbox first programmed in the diploma thesis of Felix Zörgiebel (39).

For a detailed description of each function's structure, in- and output requirements and predefined values, have a look at the comments at the beginning and throughout the corresponding m-file.

Most of the programs have been designed to be used without specific knowledge of the MATLAB-syntax. User inputs are requested via the MATLAB command window and warnings are displayed whenever specific requirements have to be fulfilled.

Functions for data analysis and manipulation:

- **A2G1AMR.m** Computes complex shear modulus from apparent response function with correction of trap effect from one-particle active data set. Calls CalibActive.m for correction of system response.
- **A2G2AMR.m** Computes complex shear modulus directly from two-particle active data set. The trap correction is done by using the one-particle passive data from a two-particle passive measurement. This is not recommended in case of non-equilibrium systems.
- **A2G2PMR_wo_trapcorr.m** Variation of A2G2PMR.m which computes the complex shear modulus directly from the apparent response function without trap correction. Calls G_2PMR_wo_trapcorr.m.

B. MATLAB-PROGRAMS

- **CalibActive.m** Imports data from an active microrheology measurement with the Rheology_new4.vi. Calibrates data with system response measurements and computes response function.
- **cutchannels.m** Reads RAW-files (binary file, big-endian ordering, signed 16 bit integers, see read_rawfile.mat) collected with the Chico-Board and allows for deleting a specific channel with unwanted data. A new RAW-file is saved with the extension “_mod” to the original file name.
- **G_2PMR_wo_trapcorr.m** Calibrates the apparent response function from a two-particle passive data set and computes the complex response function without correcting for the trap influence.
- **PSD_cal.m** Calibrates a power spectral density data set to yield physical units of nm^2/Hz which is otherwise done in the conversion from response function to shear modulus.
- **write_rawfile.m** Takes data from a U-structure and saves it in the binary format of the Chico-Board.
- **write_calfile.m** Accepts user inputs with calibration values obtained by the PSD-method with PowerSpecCalc.exe, PSD calculation DENEN.vi or TweezerCalib 2.1 and computes and saves the values to an ASCII file (*.cal file) in the same manner as the TrapCommander.vi.
- **Seperate_mG1AMR.m** Reads in data set of one-particle active data containing several independent measurements arranged as a cell array. Outputs each measurement in a separate file.
- **multi_1PMR.m** This function calculates the complex shear modulus directly from raw one-particle passive data sets by stepwise calling the corresponding subroutines. This is performed in a loop to evaluate multiple data sets. The function first requests the necessary information via user input and then runs the loop for all files, which therefore must have been taken under the same conditions (see the warning displayed in the command window). After logarithmic binning the massive raw data is discarded to prevent MATLAB from running out of memory.

-
- **multi_2PMR.m** Works the same as multi_1PMR.m for two-particle passive data.
 - **multi_1AMR.m** Calls CalibActive.m and A2G1AMR.m in a loop to evaluate multiple data sets of one-particle active data, assuming all of them have been taken under the same conditions (namely calibration factors for the QPDs, trap stiffness and system response).
 - **multi_2AMR.m** Similar to multi_1AMR.m for evaluating multiple data sets of two-particle active measurements taken under the same conditions. See also A2G2AMR.m which is called in a loop.

Plot functions for comparing a variety of data sets: (These functions still lack some details like axes labels and legends.)

- **Compare_G1AMRG1PMRx.m** Reads in multiple already evaluated data sets of one-particle active measurements and plots apparent, calibrate response function and complex shear modulus and asks whether any should be discarded. The rest will be averaged to one data set. The same is performed for multiple corresponding data sets of one-particle passive measurements. Finally the averaged passive and active data sets will be compared in one single plot. This is only done for the x-direction (referring to the x-direction of the old MR setup).
- **Compare_G1AMRG1PMRy.m** The same as the above, only for the y-direction.
- **plot_compare_meanG1PMR.m** Subroutine of Compare_G1AMRG1PMRx/y.m for plotting multiple data sets to check for and discard artifacts.
- **Compare_G2AMR2PMR.m** A similar program as the above for multiple data sets of two-particle active and passive measurements. Plots all data sets, asks for discarding any, averages the rest and plots this. Distinguishes between orientation of the bead pairs in x- or y-direction.
- **cut_multi_2AMR.m** Subroutine of Compare_G2AMR2PMR.m for plotting multiple data sets of two-particle active measurements and check for and discard artifacts.

B. MATLAB-PROGRAMS

- **cut_multi_2PMR.m** Subroutine of Compare_G2AMR2PMR.m for plotting multiple data sets of two-particle passive measurements and check for and discard artifacts.
- **CompareG1PMRG2PMR.m** A comparison plot function for two-particle passive data sets. Reads in multiple files of evaluated data sets and averages the intrinsic one-particle data and the two-particle data and displays both in one plot. Distinguishes between x- and y-direction.
- **plotAa.m** Plots the response function of an active microrheology data set.
- **plot_G1AMR.m** Plots the shear modulus over frequency of a one-particle active measurement.
- **plot_G2AMR.m** Plots the shear modulus over frequency of a two-particle active measurement.
- **plot_system_response.m** Plots the system response over frequency.
- **plot_multi_1AMR.m** Plot function for multiple data sets of one-particle active measurements stored in a cell array. Plots apparent and trap corrected response function as well as the complex shear modulus over frequency showing all data sets in one graph.
- **plot_multi_1PMR.m** Similar to plot_multi_1AMR.m for one-particle passive data sets.
- **plot_multi_2PMR.m** Plots multiple data sets of two-particle passive data. The power spectral densities, apparent and trap corrected response functions as well as the complex shear modulus is plot versus frequency. A discrimination between x- and y-channel is plotted as well as a comparison graph to show discrepancies between the two coordinates. Until now the intrinsic one-particle data of each data set is not included into the plotting.
- **plot_multi_2AMR.m** Same as the above for two-particle active data sets. Does not discriminate between different directions of the applied driving force.

Appendix C

Alignment procedure for the optical trapping setup

C.1 Setting up chassis and camera

- First install the microscope's lower chassis on the optical table and insert the 1"-turning mirror. Place a holder with a downward pointing dichroic mirror in the upper opening. Direct a visible light laser in the left opening, such that it enters the chassis parallel to the optical table and perpendicular to its face. Make sure it also leaves the chassis on the lower right in the same manner.
- Insert the tube lens into its place.
- Make sure to dim the laser intensity as much as possible (for example with neutral density filters) to not damage the CCD-chip of the camera.
- Place the CoolSnap EZ camera (without its front lens) to the right of the tube lens. The tube length for Zeiss microscopes is 160 mm. If necessary, dim the room light or place a shielding between camera and chassis to prevent an overexposure of the camera. Position the camera such that it is in the focus of the tube lens, i.e. minimize the spot of the laser beam on the camera. Make sure the spot is also in the middle of the chip in lateral direction. Fix the camera to the table.
- Remove the laser and replace the holder with the dichroic mirror by the upward pointing model with the 1064 nm reflecting dichroic.

C. ALIGNMENT PROCEDURE FOR THE OPTICAL TRAPPING SETUP

- Insert the DIC-prism holder. Remove the manual xy-stage and the piezo-stage for better accessibility.

C.2 Laser alignment

- Leave enough space between laser and microscope for the beam steering optics. Compare table C.1 for necessary focal lengths of the optics and minimum required distances.
- Fix the laser on the table and make sure appropriate safety measures are taken and beam dumps are placed in the laser path. Adjust the laser output power to at least 1.2 W, such that it operates in the TEM₀₀ mode.
- Insert the optical isolator in the beam path, such that the beam enters and exits it in the middle of the in- and output aperture. Use the 4-axis tilt aligner for fine adjustment.

For aligning the isolator proceed as follows:

- Place a power meter in front of the exit aperture.
 - To align the isolator to the laser's plane of polarization rotate the input polarizer until the transmission is maximized.
 - Repeat for the output polarizer. The maximum should be around 45° relative to the laser's plane of polarization, which here is vertical.
- Make sure to put beam dumps at the polarizers' output facets.
 - Place the beam expander in the laser path. The beam should enter and exit perpendicular without any deflection from its original direction. Use the tilt aligner for fine adjustment.
 - Turn the expander's optics until the beam is collimated with a diameter of 4 mm ($1/e^2$). Check with a beam profiler at different distances.
 - Put the motorized rotation stage with the half-wave plate for 1064 nm in the beam path. The wave plate should be centered in the beam without any tilting.

- Next insert the manual rotation stage with the Glan-laser polarizer behind the half-wave plate. Be careful with the laser light exiting from the side port. Again the laser should enter and exit the optic perpendicular. Check for any unwanted reflections coming out of the polarizer and adjust its position accordingly.
- Use the polarizer–half-wave plate combination to adjust the laser power to the desired quantity, i.e. as small as possible during alignment. Place a beam dump at the polarizer’s output facet. If the polarizer is turned, this has to be readjusted.
- Leave enough space for the holders with dichroic mirrors used later on to couple in the 980 nm and 830 nm laser diodes. It makes sense to already place them coarsely aligned into the beam path in this step.
- Now use two mirrors to steer the beam in the microscope’s upper side port. It might help to place a mirror on top of the DIC-prism holder and two pinholes in the beam path at well separated distances. Try to align the beam with the mirrors such, that the back-reflected beam from the mirror co-aligns with the incoming beam. In each step the pinholes’ positions have to be readjusted. Using an IR-viewer greatly simplifies this.
- Screw the objective into the prism-holder. Carefully place the manual xy-stage, the piezo-stage and the sample holder on top of the microscope chassis. Place a cover slip with some immersion oil on the sample holder and put a drop of water on top.
- By adjusting the cover slip’s height with the sample holder, one should see the back-reflection of the laser from the coverslip–water interface on the CoolSnap camera. Adjust the laser power to clearly see the reflection.
The reflection should be around the center of the field of view and more importantly symmetric. Also the intensity distribution should not shift from one side to the other during focusing. Otherwise the beam does not enter the objective perpendicularly (see figure C.1a).

A second beam line, the so called indirect beam, can be implemented by splitting up the laser by polarization. Therefore, a polarizing beam splitter and a beam combiner have to be placed in the path of the direct beam.

C. ALIGNMENT PROCEDURE FOR THE OPTICAL TRAPPING SETUP

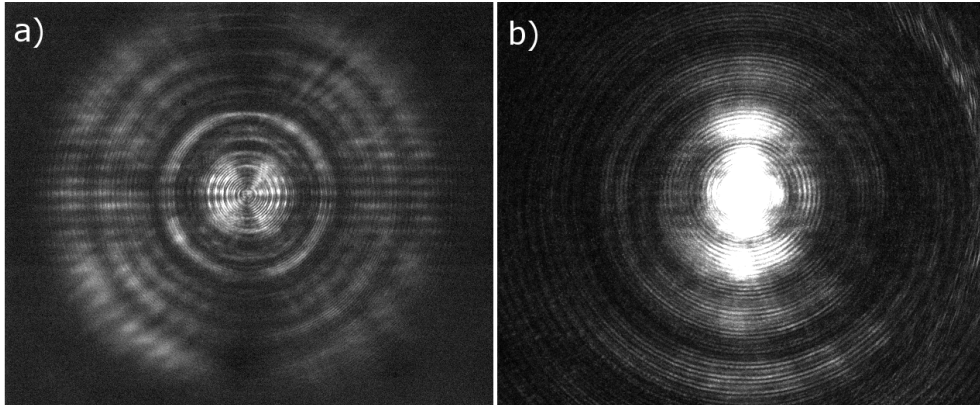


Figure C.1: Reflections at the bottom glass–water interface - a) Reflection of the direct beam close to the coverslip surface. b) Reflexion of the indirect beam. The different patterns are due to polarization effects.

- The beam combiner within its special holder has to be placed not more than 40 mm away from the chassis opening. The direct beam has to enter and leave it perpendicular and the upper side of the crystal has to be parallel to the surface of the table.
- Place the beam splitter in a rotation mount on top of a 4-axis tilt aligner and move it into the beam path, close enough to the laser to leave enough space for the other optics. Adjust the Glan laser polarizer and the half wave plate in front of the 1064 nm laser such that a detectable amount of light exits the beam splitter through the side port.
- Adjust the tilt aligner so that the exiting beam runs perpendicular to the transmitted light. Watch out for unwanted secondary reflections.
- Use a mirror to steer the beam via the combiner into the microscope. Again a back-reflection from the glass–water interface should be visible. Fine tune the orientation of the beam splitter and the mirror to overlap the new reflection with the one from the direct beam. It should also be symmetric and not shift upon focusing (see figure C.1b). It is crucial that the beam runs parallel to the table surface and hits all optics perpendicularly. Readjust the orientation of the beam combiner if necessary.

	direct beam	d [mm]	indirect beam	d [mm]
	BFP objective – dichroic	32.7		
	dichroic – chassis	60		
	chassis – PBS2	40		
Total		132.7		
	PBS2 – 200f (194.8)	67.3	PBS2 - 150f (144.6)	17.3
	200f (194.8) – 75f (69.9)	260.5	150f (144.6) – 75f (69.9)	214.5
	75f (69.9) – EOD exit	15	75f (69.9) – AOD (mid.)	75
	EOD exit – defl. plane	50		
	defl. plane – EOD entr.	75		
	EOD entr. – 100f (97.1)	50		
	100f (97.1) – 100f (97.1)	194.2		
	100f (97.1) – EOD exit	50		
	EOD exit – defl. plane	50		
	defl. plane – EOD entr.	75		
Total		887		306.8
	75f (69.9) - -35f (28.4)	94.1		

Table C.1: Distances between beam steering optics - Distances between neighboring optical elements are given. The list starts from the back-focal-plane of the objective and ends at the last telescope. Up to the beam splitter PBS2 the beam line is identical. The total lengths given at the end define the minimum size of the rectangle formed by the two beam paths (without turning mirrors at the vertices). For the achromatic lenses (Thorlabs) the values given in brackets indicate their back-focal length.

C.3 Implementing telescope lenses

The setup involves four telescopes, three in the direct and one in the indirect beam path. They are used for changing the beam diameter and propagating conjugate planes for beam steering.

The first telescope in the direct beam only reduces the beam diameter so that the beam is small enough to propagate through the EOD without distortion.

The second telescope is a one-to-one telescope in a 2f-configuration. The beam width is maintained, only the deflection plane of the first EOD is imaged onto the deflection plane of the second.

The third telescope images this plane onto the back-focal plane of the objective and expands the beam at the same time to fill the back aperture.

In the indirect beam path only one telescope is necessary to image the deflection plane as well as expand the beam to overfill the objective's back aperture.

The telescopes offer a large freedom to steer the beam into the wanted direction but it is advantageous to hit all the lenses perpendicular and in the middle to not introduce too many aberrations. With the three telescopes in the direct beam path and the large distance between them, the alignment can be quite tedious. It is therefore useful to employ a beam profiler and follow a few tricks.

- First mark on the screen the position of the back-reflection on the camera, since this will serve as the reference point throughout the following procedure.
- One should start from the lens closest to the microscope in the direct beam. The focus of this lens has to lie in the back-focal plane of the objective. The lens with a focal length of 200 mm therefore has to be placed roughly 107.3 mm away from the microscope chassis. If the focus lies in the back-focal plane, the beam should be collimated by the objective. Move the lens carefully in the direction of propagation to achieve the best collimation. Make sure the lens stands perpendicular to the direction of propagation and fix the holder to the table.
- Insert a mirror between the lens and the beam combiner and steer the beam onto the CCD chip of beam profiler. This should be placed at a distance equal to two times the focal length of the lens, i.e. 400 mm. Here the beam has the same diameter as the beam without the lens.

C.3 Implementing telescope lenses

- Take out the lens and remember the position of the beam.
- Place the lens back in its holder and use the screws to adjust the lens position in the xy-plane perpendicular to the direction of propagation. Steer the beam back onto its original position.
- Remove the mirror and observe the back-reflection on the camera. It will look quite distorted compared to the one without the lens, but nevertheless provides an indication of the lens' alignment. The reflection should be symmetric and not shift during focusing.
- The second lens with a focal length of 75 mm should be placed at distance equal to the sum of both lenses, i.e. 275 mm, so that the beam is collimated again. Since the beam is now quite large, it can be difficult to verify the correct collimation. Nevertheless, it should be measured whether the diameter has the same value close and far away from the telescope.
- Using the mirror again, the lens can be aligned such that the laser hits its original position. Here, the back-reflection on the camera, which resembles now the one without the telescope, should be at its original position again.

This procedure can be followed for the subsequent telescopes as well. To get the correct distance between the first, which means the one closer to the chassis, to the next telescope, one can take advantage of the fact, that the beam has to be collimated after implementing the second lens of the first and the first lens of the second telescope.

The second telescope is a 1–1 telescope, which employs two 100 mm lenses. This is the minimum focal length, due to the length of the EODs, which is 12.5 cm. The deflection plane, which lies about 5 cm behind the exit aperture, has to be propagated through the telescope.

The distance between the second and the third telescope is not important, since no imaging of a conjugate plane is involved here. A combination of a 75 mm and 35 mm lens has been used here to narrow the beam from 4 mm to about 1.8 mm $1/e^2$, which is the clear aperture of the EOD. Notice that the beam must not be larger than this, because the EOD does not contain a hard aperture and overfilling can damage the electrodes attached to the crystal.

C. ALIGNMENT PROCEDURE FOR THE OPTICAL TRAPPING SETUP

To test the complete set of telescope, one can remove either of the telescopes and look if the reflection on the camera stays in the same place and looks symmetric.

The telescope for the indirect beam uses a combination of a 100 mm and a 150 mm lens. The beam is expanded to about $6 \text{ mm } 1/e^2$ to overfill the objective's back aperture. Due to the lack of space, it is not possible to place a mirror between the chassis and the telescope. One can remove the objective and set up the beam profiler above the chassis to check for the proper collimation of the beam.

C.4 Alignment of the detection part

The detection part of the microscope chassis is placed on top of the lower part via a tripod. This part has to be aligned such, that the condenser objective collects the light of the optical trap, collimates it and images the back-focal-plane onto a quadrant photo-diode. It is therefore crucial to align the condenser objective to the same axis as the focusing objective, i.e. the laser light exits collimated and perpendicularly. To facilitate this, follow the procedure below.

- Have a water sample, with a drop of immersion oil on top, fixed on the holder.
- Coarsely align the upper part such that it sits straight on the tripod with respect to its side. Tighten the four screw.
- Screw the DIC-prism holder into the upper part's thread. Make sure it is oriented correctly and accepts the DIC-prism. Insert the objective.
- Turn the tripod's three micrometer screws to the maximum so that the objective does not hit the sample.
- Carefully place the tripod onto the holders of the bottom part.
- As a starting point, one can use a spirit level to align the upper part horizontally.
- Turn on the laser and focus the trap slightly above the bottom cover slip. Now slowly lower the detection part by turning each of the tripod's micrometer screws in equal increments until the objective reaches the immersion oil.

C.4 Alignment of the detection part

- Slowly lower the detection part further while watching for any laser light exiting the objective. A focus should become visible which moves further away the closer one gets to the focus of the optical trap. Proceed until a collimated beam exits the chassis. Be sure not to hit the sample with the objective!
- If no laser light can be spotted, loosen the upper parts connection to the tripod and slightly shift it relative to it. At some point the laser light should become visible.
- Insert a couple of Thorlabs lens tubes with an iris at both ends into the upper opening of the chassis. The laser has to be aligned such, that it hits both of the apertures in the center. It can help to place a small Watec-camera on top of this construction and observe the transmitted light on a screen. Make sure to lower the laser intensity accordingly.
- Now move the upper part relative to the tripod by small increments, for example by carefully hitting it with a rubber mallet. Try to align the beam into the center of the lower iris. If it does not come out perpendicularly it will not hit the upper iris in the middle. Then the angle of the whole tripod has to be altered. Notice that any change of the micrometer screws not only alters the angle of the detection part, but also the height which has to be readjusted such that the beam is again collimated. Then repeat this step until the beam goes straight through both apertures. Try to align the upper part without introducing a rotation relative to the tripod. This will alter the direction of the beam going through the side port as is describe further down.
- Insert the dichroic mirror for the illumination. (This will lead to a small lateral beam offset due to its thickness, which has to be corrected eventually by moving the QPD.)
- Insert the polarizing beam splitter. Watch for any light coming out at the side port of the chassis. Adjust the polarization by turning the first polarizer accordingly. The light from the direct path will now exit through the side port, while the indirect beam is transmitted to the top port. If the beam comes out of the side port with a deviation in the horizontal axis, the whole upper part has to be rotated. This will most probably make a realignment of the upper part necessary.

C. ALIGNMENT PROCEDURE FOR THE OPTICAL TRAPPING SETUP

If a variation in the vertical direction is observed, the lateral position of the PBS in its holder has to be changed. Carefully shift its position and tighten it with extreme caution, since a large stress can damage the crystal. A collimated beam should exit the side port in the middle.

C.4.1 Aligning the quadrant photodiodes

The BFP of the condenser objective has to be imaged onto the QPDs. A 50 mm lens is used at a distance of 100 mm to generate a 1–1 image at the distance of $2f$. The lens sits at the very front of a tube, which can be inserted into the microscope's port. At its end a flexure xy-adjustment plate for the Thorlabs 30 mm cage system is placed to which later on the QPD can be attached. A Watec-camera can be placed there as well. The distance between lens and CCD-chip is roughly the same as for the lens–QPD variant. Therefore, the BFP can be observed on the screen. Since there is no aperture in the objective, the correct position of the BFP is not easy to determine. Try the following steps:

- Insert the 50 mm lens with the tube and the xy-mount into the top port and switch on the laser. At about 5 mm above the plate the laser should have roughly the same diameter as the collimated beam without the lens. If the beam appears too wide or a focus is visible, shift the tube axially to obtain the proper beam diameter. Fix the tube's axial position with the locking ring.
- Insert the Watec-camera, after making sure the laser intensity has been lowered enough. The intensity profile should be homogeneous and Gaussian. The image should also have a sharp boundary by the objective's exit pupil (see figure C.2).
- Insert the QPD in the right orientation (see the labels on the housing). Turn on the bias-voltage and the differential amplifier. Adjust the intensity, such that the signal is around the middle of the voltage range. Insert a neutral density filter in the slit in front of the QPD if necessary. Use the xy-adjuster to position the QPD in the middle of the beam.
- The angular position of the QPD can only be fixed after aligning the AODs and EODs (see section C.5).

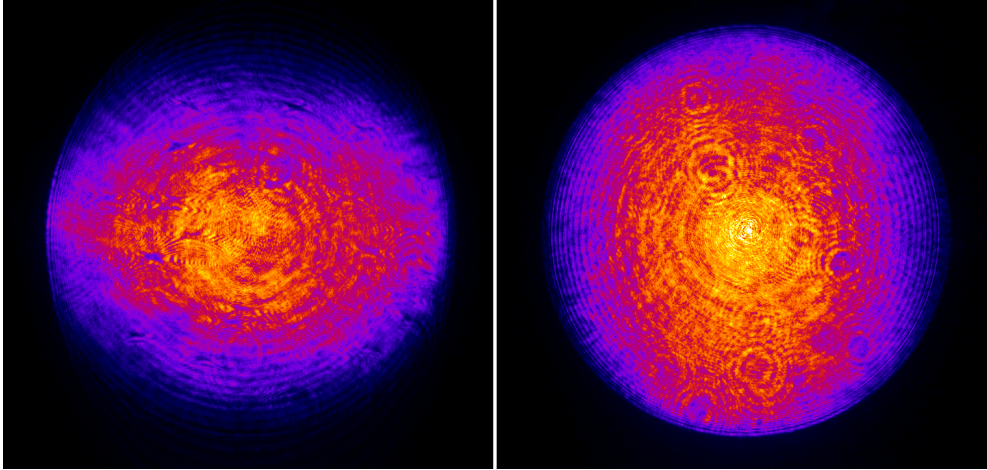


Figure C.2: Images of the laser profile in the back-focal plane - The objective's BFP is imaged with a 50 mm lens onto a camera. a) shows the direct beam, b) the indirect beam. The asymmetry is due to polarization effects, since the direct beam is reflected at the PBS. The small circular structures are either dust particles on optics close to the imaging plane or air bubbles in the immersion oil. Images were taken with a beam profiler (ML37210F, Metrolux GmbH, Göttingen, Germany).

- An oscillating signal has to be applied to the x- or y-channel of the deflectors. Observe the signal on the corresponding channel of the QPD and adjust the frequency and amplitude of the oscillation to get a maximum signal. In the perpendicular channel no cross-talk of the oscillation should be visible. Otherwise turn the tube with the QPD accordingly to minimize the cross-talk. Fix the Tube with the locking ring to the microscope chassis.
- Follow these steps for all QPDs.

C.4.2 Setting up Köhler illumination for DIC

For Köhler illumination, the light source has to be imaged into the BFP of the condenser objective. Since the objective is not equipped with an aperture diaphragm, this as well has to be imaged into the BFP. The field diaphragm has to be imaged into the object plane. To achieve this, the light path has been calculated in MATLAB and verified by an optics design program (WinLens 4.4.1, Linos Photonics, Göttingen, Germany). A sketch of the illumination path is shown in figure C.3, where the necessary optics, their

C. ALIGNMENT PROCEDURE FOR THE OPTICAL TRAPPING SETUP

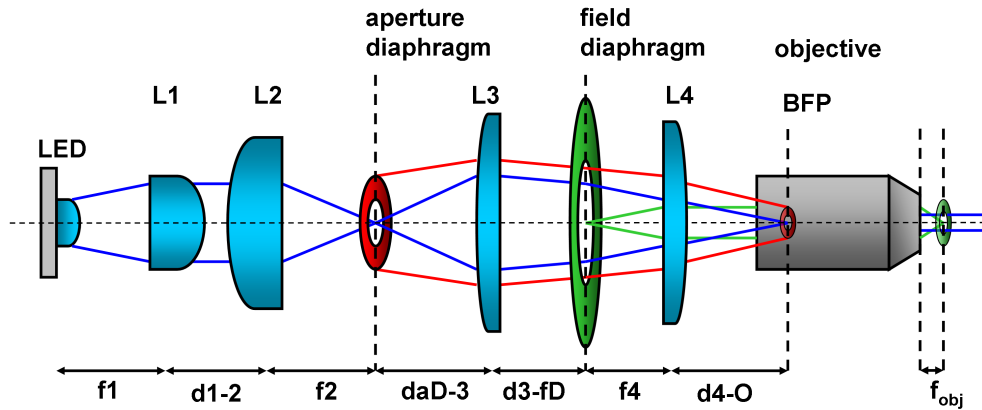


Figure C.3: Illumination light path - Sketch of the imaging in the illumination path (not drawn to scale, no geometrical optics). The LED is imaged via the collector lens L1 and lens L2 at the plane of the aperture diaphragm. Both are subsequently imaged into the objective's BFP via L3 and L4. Lens L4 images the field diaphragm into the object plane. The distances and focal lengths can be found in table C.2. Note, that a turning mirror between L3 and L4 is not shown, which was introduced in the actual setup for compactness. Also, the DIC-polarizer and a diffuser are not displayed.

orientation and the distances are drawn. To establish Köhler illumination, proceed as follows:

- Insert the 75 mm lens in its tube into the side port and push it to the very end. Lock its position with the screw.
- Insert two 4"-assembly rods into the cage holder containing the LED.
- Slide the cage plate holding the 1"-tube with the 12 mm lens close to the LED. Turn it on and adjust the holder such, that the LED forms a sharp image on a wall several meters away. Fix the holder.
- Insert the 25.4 mm lens into the tube.
- Slide the small iris, which serves as the aperture diaphragm, at the position where the LED is imaged and fix its position.
- Attach the the threaded iris, which serves as the field diaphragm, to the xy-mount and screw on the 2"-lens tube. Fix this to the side of the mirror cube.

On top insert two 4"-rods and slide the DIC polarizer in its rotation mount and the 40 mm lens onto this assembly. Insert the system into the side port of the microscope.

- Slide the LED-part onto the cage system and observe the image on the CoolSnap camera. Use the trapping laser reflection to set the focus close to the bottom surface of the coverslip. Shift the whole illumination assembly axially and with the lens tube and laterally with the xy-holder until the field diaphragm is in focus and centered in the field of view. Open the field diaphragm that it is just outside of the field of view.
- Position the LED-part about $dD3 = 45$ mm away from the 40 mm lens and this roughly $d3F = 99$ mm from the 75 mm lens C.2.
- There is no Bertrand lens to observe the objective's BFP. One can use the Water-camera at the top port to at least see the reflected image of the LED and the aperture diaphragm in the condenser's BFP. Adjust the LED-part and if necessary the 40 mm lens to image the LED in the center of the BFP.
- Lock the position of all optical elements in the cage system and fix this to the microscope chassis.
- Because of the striped layout of the LED it makes sense to insert a diffuser between the aperture diaphragm and the 40 mm lens. Position it such, that it is far away from any conjugate plane.
- Insert a polarizer at a 45° angle in the holder of the microscope's bottom part. Rotate the polarizer in the cage system to achieve maximum extinction.
- Insert the DIC prisms and use them together with the aperture diaphragm to adjust the contrast for the DIC illumination.

C.5 Alignment of AODs and EODs

The alignment of the EODs is rather straight forward, since they are direct throughput devices. The only challenge poses the small diameter of the crystals and the correct

C. ALIGNMENT PROCEDURE FOR THE OPTICAL TRAPPING SETUP

Elements	distance [mm]	label
LED - 12f lens	12	f1
12f lens - 25.4f lens	3.7	d12
25.4f lens - aperture diaphragm	25.4	f2
aperture diaphragm - 40f lens	44.9	dA3
40f lens - field diaphragm	99	d3F
field diaphragm 75f lens	73	f4
75f lens - BFP	56.7	d4O

Table C.2: Distances between illumination optics - The distances between neighboring optical elements as calculated. For lenses, the distance to the surface is given. In practice, the alignment cannot be carried out with such accuracy; the given lengths only serve as a reference value. The third column corresponds to the labels as declared in table C.2

orientation with respect to the plane of polarization of the laser. The deflection occurs only in the direction of the polarization. At the exit port of the first EOD, i.e. the one closer to the laser, an integral half-wave plate is mounted to rotate the exiting light by 45° . Another wave plate at the entrance port of the second EOD turns the polarization by another 45° in the same direction, so that the plane of deflection is perpendicular to the one of the first EOD.

- It is important to turn the laser power to less than 200 mW to not damage the device. Again it is useful to place a mirror between the last telescope lens and the housing to direct the beam onto a beam profiler for marking its original positions as well as observing beam distortions as a sign for misalignment.
- The polarization of the direct beam is parallel to the table. Therefore, the first EOD has to be oriented in its holder such that the plane in the middle of the two BNC connectors points upwards. See figure C.4.
- Place the EOD and its holder on a 4-axis tilt aligner into the beam path between the third and the second telescope. Coarsely align it such, that the beam enters and exits the device in the middle of the apertures.
- Use the tilt aligner to fine adjust the EOD's position such, that the beam hits its original positions and the profile is symmetric. Watch for any distortions of the

beam wings indicating a non-symmetric incident on the hexagonal crystal.

Due to its length, there is no single deflection plane in the crystal. Nevertheless deflecting the beam should lead to a minimal change of the intensity distribution in the back-focal plane of the objective. A rough estimate for the corresponding distance between the EOD and the imaging telescope length has been found during the characterization of the device (see chapter 2.2).

- For a fine adjustment apply a sinusoidal voltage with a maximum amplitude of 2V peak-to-peak to the driver. The frequency can be chosen to an easily observable value.
- Place a water sample onto the microscope and put the detection part on top. Observe the signal on the QPD with an oscilloscope or the data acquisition board.
- By moving the EOD in its holder parallel to the beam path try to minimize the amplitude of the oscillation on the QPD.
- After having found the proper distance, check again with the beam profiler if the laser still enters and exits the EOD without distortions. Realign according to the above procedure if necessary.
- Repeat this procedure for the second EOD. This has to be placed between the second and the third telescope. Its distance to the first lens of the third telescope is shorter, since here a 75 mm lens is used. The EOD has to be rotated by 90° with respect to the first one.
- Place an achromatic half-wave plate behind the third telescope. Since the EODs turn the polarization by 90° in total, this has to be compensated so that the beam can pass the polarizing beam splitter without being reflected.

The alignment of the AODs is more cumbersome, since it depends on the position of the AODs relative to the incoming beam as well as their position relative to each other. The AOD-system can either be adjusted to give maximum throughput at one position or a constant throughput over a broad range of deflection angles. Since there is no rule of thumb, follow the instructions given in the manual (97). A more elaborate procedure, but for a different type of AODs is given in (22), which uses a modified QPD to optimize the power of the diffraction order over a large frequency band.

C. ALIGNMENT PROCEDURE FOR THE OPTICAL TRAPPING SETUP

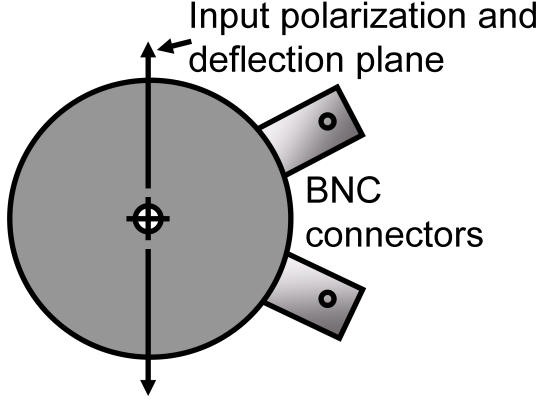


Figure C.4: EOD input polarization - The figure shows the orientation of the electro-optical deflector with respect to the input polarization. Schematic prepared after (96).

C.6 Conversion factors

Several of the components employed in the setup have to be calibrated before usage. To convert the images obtained by the CoolSnap camera from pixels to a physical length of micrometer, an optical grating with a defined grating constant was imaged. The conversion factor is $0.0636 \mu\text{m}/\text{px}$, without pixel binning.

	Deflector (direction)	Conv. [$\mu\text{m}/\text{V}$]	offset [V]
Lock-In 7280	AOD1 (Y)	1.092	2.1
	AOD2 (X)	0.994	2.4
	EOD1 (X)	0.202	
	EOD2 (Y)	0.212	
AFG 3022	AOD1 (Y)	10.962	2.1
	AOD2 (X)	10.238	2.4
	EOD1 (X)	0.277	
	EOD2 (Y)	0.280	

Table C.3: Conversion factors for the optical deflectors - Each deflector was calibrated with the employed frequency generators. The offset for the AODs gives approximately the center frequency to position them in the middle of the field of view. If switching between external and internal voltage input, this offset has to be changed to match the voltage adjusted with the potentiometer.

The voltage applied to the optical deflectors translates into a lateral movement of the trap in the sample plane. This depends on the in- and output-impedance of the voltage supply. To calibrate this, a bead is trapped in a water sample and a sine-wave

voltage is applied by the frequency generator, which is employed during the experiments. A slow frequency below 1 Hz is chosen such, that the bead completely follows the trap movement. A video of this motion is acquired with the camera and analyzed by a custom-built feature-finding algorithm in LabVIEW. The bead's trajectory is then fitted with a sine-curve in Origin (OriginPro 8, OriginLab Cooperation, Northampton, MA, USA). Using the camera calibration factor above, the ratio of the voltage amplitude and the amplitude of the bead's oscillation give the desired conversion factor. In table C.3 the values are given for both frequency generators employed in the setup.

C. ALIGNMENT PROCEDURE FOR THE OPTICAL TRAPPING SETUP

References

- [1] Y.-L. SHIH AND L. ROTHFIELD. **The Bacterial Cytoskeleton.** *Microbiol. Mol. Biol. Rev.*, **70**(3):729–754, 2006. 1
- [2] D. E. DISCHER AND Y.-L. JANMEY, P. AND WANG. **Tissue Cells Feel and Respond to the Stiffness of Their Substrate.** *Science*, **310**(5751):1139–1143, 2005. 2
- [3] A. J. ENGLER, S. SEN, H. L. SWEENEY, AND D. E. DISCHER. **Matrix Elasticity Directs Stem Cell Lineage Specification.** *Cell*, **126**(4):677–689, August 2006. 2
- [4] F. C. MACKINTOSH AND C. F. SCHMIDT. **Active cellular materials.** *Curr. Opin. Cell Biol.*, **22**(1):29–35, February 2010. 2
- [5] F.C. MACKINTOSH AND C.F. SCHMIDT. **Microrheology.** *Curr. Opin. Colloid Interface Sci.*, **4**(4):300–307, August 1999. 2
- [6] A. ASHKIN. **Acceleration and Trapping of Particles by Radiation Pressure.** *Phys. Rev. Lett.*, **24**(4):156–159, January 1970. 3
- [7] A. ASHKIN AND J. M. DZIEDZIC. **Optical Levitation by Radiation Pressure.** *Appl. Phys. Lett.*, **19**(8):283–285, October 1971. 3
- [8] A. ASHKIN, J. M. DZIEDZIC, J. E. BJORKHOLM, AND STEVEN CHU. **Observation of a single-beam gradient force optical trap for dielectric particles.** *Opt. Lett.*, **11**(5):288–290, May 1986. 3
- [9] K. SVOBODA AND S. M. BLOCK. **Biological Applications of Optical Forces.** *Annu. Rev. Biophys.*, **23**(1):247–285, 1994. 3

REFERENCES

- [10] M. J. LANG AND S. M. BLOCK. **Resource Letter: LBOT-1: Laser-based optical tweezers.** *Am. J. Phys.*, **71**(3):201–215, 2003. 3
- [11] A. ASHKIN. **Forces of a single-beam gradient laser trap on a dielectric sphere in the ray optics regime.** *Biophys. J.*, **61**(2 I):569–582, 1992. 4, 5
- [12] G GOUSBET AND G. GREHAN. **Generalized Lorenz-Mie theories - from past to future.** *Atomization and sprays*, **10**:277–333, 2000. 5
- [13] E. A. ABBONDANZIERI, W. J. GREENLEAF, J. W. SHAEVITZ, R. LANDICK, AND S. M. BLOCK. **Direct observation of base-pair stepping by RNA polymerase.** *Nature*, **438**(7067):460–465, November 2005. 5
- [14] J. T. FINER, R. M. SIMMONS, AND J. A. SPUDICH. **Single myosin molecule mechanics: piconewton forces and nanometre steps.** *Nature*, **368**(6467):113–119, March 1994. 5
- [15] W. J. GREENLEAF, M. T. WOODSIDE, E. A. ABBONDANZIERI, AND S. M. BLOCK. **Passive All-Optical Force Clamp for High-Resolution Laser Trapping.** *Phys. Rev. Lett.*, **95**(20):208102–4, November 2005. 5
- [16] K. VISSCHER, S. P. GROSS, AND S. M. BLOCK. **Construction of multiple-beam optical traps with nanometer-resolution position sensing.** *IEEE J. Sel. Top. Quantum Electron.*, **2**(4):1066–1076, 1996. 5
- [17] L. BERGMANN AND C. SCHAEFER. *Lehrbuch der Experimentalphysik - Band 3: Wellen und Teilchenoptik.* Walter de Gruyter, 2004. 6, 7, 8
- [18] J. W. SHAEVITZ. **A Practical Guide to Optical Trapping.** Technical report, Princeton University, 08 2006. 6
- [19] M. T. VALENTINE, N. R. GUYDOSH, B. GUTIÉRREZ-MEDINA, A. N. FEHR, J. A. ANDREASSON, AND S. M. BLOCK. **Precision steering of an optical trap by electro-optic deflection.** *Opt. Lett.*, **33**(6):599–601, 2008. 7, 13, 15, 25
- [20] F. GITTES AND C. F. SCHMIDT. **Interference model for back-focal-plane displacement detection in optical tweezers.** *Opt. Lett.*, **23**(1):7–9, January 1998. 8

-
- [21] K. C. NEUMAN AND S. M. BLOCK. **Optical trapping.** *Rev. Sci. Instrum.*, **75**(9):2787–2809, September 2004. 8, 10
- [22] JOOST VAN MAMEREN. *Single molecule mechanics of biopolymers: An optical tweezer study.* Master’s thesis, Vrije Universiteit Amsterdam, 2002. 9, 40, 117
- [23] W. H. PRESS, S. A. TEUKOLSKY, W. T. VETTERLING, AND FLANNERY B. P. *Numerical recipes in C - The art of scientific computing.* Cambridge University Press, 2. edition, 1992. 9, 34
- [24] A. PRALLE, M. PRUMMER, E.-L. FLORIN, E. H. K. STELZER, AND J. K. H. HÖRBER. **Three-dimensional high-resolution particle tracking for optical tweezers by forward scattered light.** *Microsc. Res. Tech.*, **44**(5):378–386, 1999. 9
- [25] K. BERG-SØRENSEN AND H. FLYVBJERG. **Power spectrum analysis for optical tweezers.** *Rev. Sci. Instrum.*, **75**(3):594–612, March 2004. 10
- [26] M. FISCHER AND K. BERG-SØRENSEN. **Calibration of trapping force and response function of optical tweezers in viscoelastic media.** *J. Opt. A: Pure Appl. Opt.*, **9**(8):S239, 2007. 10
- [27] F. GITTES AND F. C. MACKINTOSH. **Dynamic shear modulus of a semi-flexible polymer network.** *Phys. Rev. E*, **58**(2):R1241–, August 1998. 10, 43, 73, 80, 83
- [28] S. C. KUO AND M. P. SHEETZ. **Force of single kinesin molecules measured with optical tweezers.** *Science*, **260**(5105):232–234, 1993. 10
- [29] F. GITTES, B. SCHNURR, P. D. OLMSTED, F. C. MACKINTOSH, AND C. F. SCHMIDT. **Microscopic Viscoelasticity: Shear Moduli of Soft Materials Determined from Thermal Fluctuations.** *Phys. Rev. Lett.*, **79**(17):3286–, October 1997. 10
- [30] P. M. HANSEN, I. M. TOLIĆ-NØRRELYKKE, H. FLYVBJERG, AND K. BERG-SØRENSEN. **tweezercalib 2.0: Faster version of MatLab package for precise calibration of optical tweezers.** *Comput. Phys. Commun.*, **174**(6):518–520, March 2006. 10, 11

REFERENCES

- [31] I. M. TOLIĆ-NØRRELYKKE, K. BERG-SØRENSEN, AND H. FLYVBJERG. **Mat-Lab program for precision calibration of optical tweezers.** *Comput. Phys. Commun.*, **159**(3):225–240, June 2004. 10
- [32] K. BERG-SØRENSEN, E. J. G. PETERMAN, T. WEBER, C. F. SCHMIDT, AND H. FLYVBJERG. **Power spectrum analysis for optical tweezers. II: Laser wavelength dependence of parasitic filtering, and how to achieve high bandwidth.** *Rev. Sci. Instrum.*, **77**(6):063106–10, June 2006. 10
- [33] K. BERG-SØRENSEN, L. ODDERSHEDE, E. FLORIN, AND H. FLYVBJERG. **Unintended filtering in a typical photodiode detection system for optical tweezers.** *J. Appl. Phys.*, **93**(6):3167–3176, March 2003. 11
- [34] K. C. VERMEULEN, J. VAN MAMEREN, G. J. M. STIENEN, E. J. G. PETERMAN, G. J. L. WUITE, AND C. F. SCHMIDT. **Calibrating bead displacements in optical tweezers using acousto-optic deflectors.** *Rev. Sci. Instrum.*, **77**(1):013704–6, January 2006. 12
- [35] V. BORMUTH, J. HOWARD, AND E. SCHÄFFER. **LED illumination for video-enhanced DIC imaging of single microtubules.** *J. Microsc.*, **226**(1):1–5, April 2007. 12, 20
- [36] M. ATAKHORRAMI, K. M. ADDAS, AND C. F. SCHMIDT. **Twin optical traps for two-particle cross-correlation measurements: Eliminating cross-talk.** *Rev. Sci. Instrum.*, **79**(4):043103, 2008. 13
- [37] CARL ZEISS MICROIMAGING GMBH GERMANY. **Data sheet: alpha-Plan Apochromat.** 17
- [38] CHRISTOPH PIEPER. *Techniken zur Untersuchung einzelner nicht prozessiver Motormoleküle mit optischen Fallen.* Diploma thesis, Georg-August-Universität Göttingen, 2009. 21
- [39] FELIX ZÖRGIEBEL. *Viscoelasticity of biopolymer solutions and the mechanical function of topoisomerases investigated with micromechanical trapping techniques.* Diploma thesis, Georg-August-Universität Göttingen, 2009. 22, 41, 73, 79, 99

-
- [40] F. GITTES AND C. F. SCHMIDT. **Chapter 8 Signals and Noise in Micromechanical Measurements.** In MICHAEL P. SHEETZ, editor, *Methods in Cell Biology*, **Volume 55**, pages 129–156. Academic Press, 1997. 22
- [41] A. R. CARTER, Y. SEOL, AND T. T. PERKINS. **Precision Surface-Coupled Optical-Trapping Assay with One-Basepair Resolution.** *Biophys. J.*, **96(7)**:2926–2934, April 2009. 22
- [42] D. MIZUNO, D. A. HEAD, F. C. MACKINTOSH, AND C. F. SCHMIDT. **Active and Passive Microrheology in Equilibrium and Nonequilibrium Systems.** *Macromolecules*, **41(19)**:7194–7202, 2008. 25, 26, 32, 35, 49, 54, 69
- [43] P. BOLHUIS AND F. C. MACKINTOSH. *Lecture Notes - Statistical Mechanics of Soft Matter, Chapter 2.* 2011. 30
- [44] B. SCHNURR, F. GITTES, F. C. MACKINTOSH, AND C. F. SCHMIDT. **Determining Microscopic Viscoelasticity in Flexible and Semiflexible Polymer Networks from Thermal Fluctuations.** *Macromolecules*, **30(25)**:7781–7792, 1997. 32, 33, 34, 71
- [45] M. ATAKHORRAMI, J. I. SULKOWSKA, K. M. ADDAS, G. H. KOENDERINK, J. X. TANG, A. J. LEVINE, F. C. MACKINTOSH, AND C. F. SCHMIDT. **Correlated fluctuations of microparticles in viscoelastic solutions: Quantitative measurement of material properties by microrheology in the presence of optical traps.** *Phys. Rev. E*, **73(6)**:061501–, June 2006. 33, 35, 36
- [46] J. C. CROCKER, M. T. VALENTINE, E. R. WEEKS, T. GISLER, P. D. KAPLAN, A. G. YODH, AND D. A. WEITZ. **Two-Point Microrheology of Inhomogeneous Soft Materials.** *Phys. Rev. Lett.*, **85(4)**:888–, July 2000. 35, 48, 71
- [47] A. J. LEVINE AND T. C. LUBENSKY. **One- and Two-Particle Microrheology.** *Phys. Rev. Lett.*, **85(8)**:1774–, August 2000. 35, 36, 71
- [48] A. J. LEVINE AND T. C. LUBENSKY. **Two-point microrheology and the electrostatic analogy.** *Phys. Rev. E*, **65(1)**:011501–, December 2001. 35, 36, 69

REFERENCES

- [49] M. BUCHANAN, M. ATAKHORRAMI, J. F. PALIERNE, AND C. F. SCHMIDT. **Comparing Macrorheology and One- and Two-Point Microrheology in Wormlike Micelle Solutions.** *Macromolecules*, **38**(21):8840–8844, October 2005. 35
- [50] D. MIZUNO, R. BACABAC, C. TARDIN, AND C. F. HEAD, D. AND SCHMIDT. **High-Resolution Probing of Cellular Force Transmission.** *Phys. Rev. Lett.*, **102**(16):168102, 2009. 39
- [51] J. GUCK, R. ANANTHAKRISHNAN, H. MAHMOOD, T. J. MOON, C. C. CUNNINGHAM, AND J. KÄS. **The Optical Stretcher: A Novel Laser Tool to Micromanipulate Cells.** *Biophys. J.*, **81**(2):767–784, August 2001. 39
- [52] F. WOTTAWAH, S. SCHINKINGER, B. LINCOLN, R. ANANTHAKRISHNAN, M. ROMEYKE, J. GUCK, AND J. KÄS. **Optical Rheology of Biological Cells.** *Phys. Rev. Lett.*, **94**(9):098103–, March 2005. 39
- [53] M. L. GARDEL, M. T. VALENTINE, J. C. CROCKER, A. R. BAUSCH, AND D. A. WEITZ. **Microrheology of Entangled F-Actin Solutions.** *Phys. Rev. Lett.*, **91**(15):158302–, October 2003. 39, 48, 49, 71
- [54] M. L. GARDEL, J. H. SHIN, F. C. MACKINTOSH, L. MAHADEVAN, P. MATSUDAIRA, AND D. A. WEITZ. **Elastic Behavior of Cross-Linked and Bundled Actin Networks.** *Science*, **304**(5675):1301–1305, May 2004. 39, 64
- [55] J. LIU, M. L. GARDEL, K. KROY, E. FREY, B. D. HOFFMAN, J. C. CROCKER, A. R. BAUSCH, AND D. A. WEITZ. **Microrheology Probes Length Scale Dependent Rheology.** *Phys. Rev. Lett.*, **96**(11):118104, 2006. 39
- [56] M. L. GARDEL, F. NAKAMURA, J. H. HARTWIG, J. C. CROCKER, T. P. STOSSEL, AND D. A. WEITZ. **Prestressed F-actin networks cross-linked by hinged filamins replicate mechanical properties of cells.** *PNAS*, **103**(6):1762–1767, February 2006. 39
- [57] D. MIZUNO, C. TARDIN, C. F. SCHMIDT, AND F. C. MACKINTOSH. **Nonequilibrium Mechanics of Active Cytoskeletal Networks.** *Science*, **315**(5810):370–373, 2007. 39, 54, 55, 57, 70

-
- [58] O. C. RODRIGUEZ, A. W. SCHAEFER, C. A. MANDATO, P. FORSCHER, W. M. BEMENT, AND C. M. WATERMAN-STORER. **Conserved microtubule-actin interactions in cell movement and morphogenesis.** *Nat. Cell Biol.*, **5**(7):599–609, July 2003. 39
- [59] C. P. BRANGWYNNE, F. C. MACKINTOSH, S. KUMAR, N. A. GEISSE, J. TALBOT, L. MAHADEVAN, K. K. PARKER, D. E. INGBER, AND D. A. WEITZ. **Microtubules can bear enhanced compressive loads in living cells because of lateral reinforcement.** *J. Cell Biol.*, **173**(5):733–741, 2006. 39, 72, 74
- [60] V. PELLETIER, N. GAL, P. FOURNIER, AND M. L. KILFOIL. **Microrheology of Microtubule Solutions and Actin-Microtubule Composite Networks.** *Phys. Rev. Lett.*, **102**(18):188303–4, May 2009. 39, 49, 50, 61, 62, 63
- [61] Y.-C. LIN, G. H. KOENDERINK, F. C. MACKINTOSH, AND D. A. WEITZ. **Control of non-linear elasticity in F-actin networks with microtubules.** *Soft Matter*, **7**(3):902–906, 2011. 40
- [62] M. BAI, A. R. MISSEL, W. S. KLUG, AND A. J. LEVINE. **The mechanics and affine-nonaffine transition in polydisperse semiflexible networks.** *Soft Matter*, **7**(3):907–914, 2011. 40
- [63] J. HOWARD. *Mechanics of motor proteins and the cytoskeleton.* Sinauer Associates, Inc., 2001. 40, 42, 44, 45, 47, 67
- [64] J. LÖWE, H. LI, K. H. DOWNING, AND E. NOGALES. **Refined structure of $\alpha\beta$ tubulin at 3.5 Å resolution.** *J. Mol. Biol.*, **313**(5):1045–1057, November 2001. 41
- [65] M. A. JORDAN AND L. WILSON. **Microtubules as a target for anticancer drugs.** *Nat. Rev. Cancer.*, **4**(4):253–265, April 2004. 42
- [66] F. GITTES, B. MICKEY, J. NETTLETON, AND J. HOWARD. **Flexural rigidity of microtubules and actin filaments measured from thermal fluctuations in shape.** *J. Cell Biol.*, **120**(4):923–934, 1993. 42, 44, 78, 83

REFERENCES

- [67] F. PAMPALONI, G. LATTANZI, T. JONÁŠ, A. AND SURREY, E. FREY, AND E.-L. FLORIN. **Thermal fluctuations of grafted microtubules provide evidence of a length-dependent persistence length.** *PNAS*, **103**(27):10248–10253, 2006. 42
- [68] C. P. BRANGWYNNE, G. H. KOENDERINK, E. BARRY, Z. DOGIC, F. C. MACKINTOSH, AND D. A. WEITZ. **Bending Dynamics of Fluctuating Biopolymers Probed by Automated High-Resolution Filament Tracking.** *Biophys. J.*, **93**(1):346–359, 2007. 42, 44, 47, 78, 80, 83
- [69] C. F. SCHMIDT, M. BAERMANN, G. ISENBERG, AND E. SACKMANN. **Chain dynamics, mesh size, and diffusive transport in networks of polymerized actin: a quasielastic light scattering and microfluorescence study.** *Macromolecules*, **22**(9):3638–3649, September 1989. 43, 44
- [70] Y.-C. LIN, G. H. KOENDERINK, F. C. MACKINTOSH, AND D. A. WEITZ. **Viscoelastic Properties of Microtubule Networks.** *Macromolecules*, **40**(21):7714–7720, October 2007. 43, 47, 50
- [71] D. C. MORSE. **Viscoelasticity of Concentrated Isotropic Solutions of Semiflexible Polymers. 2. Linear Response.** *Macromolecules*, **31**(20):7044–7067, October 1998. 43
- [72] D. C. MORSE. **Viscoelasticity of Concentrated Isotropic Solutions of Semiflexible Polymers. 1. Model and Stress Tensor.** *Macromolecules*, **31**(20):7030–7043, October 1998. 43
- [73] D. C. MORSE. **Viscoelasticity of Concentrated Isotropic Solutions of Semiflexible Polymers. 3. Nonlinear Rheology.** *Macromolecules*, **32**(18):5934–5943, September 1999. 43
- [74] G. H. KOENDERINK, M. ATAKHORRAMI, F. C. MACKINTOSH, AND C. F. SCHMIDT. **High-Frequency Stress Relaxation in Semiflexible Polymer Solutions and Networks.** *Phys. Rev. Lett.*, **96**(13):138307, 2006. 43
- [75] DAVID GOODSSELL. **Actin - Molecule of the month**, July 2001. 44

-
- [76] A. GERSON-GURWITZ, C. THIEDE, N. MOVSHOVICH, V. FRIDMAN, M. PODOLSKAYA, T. DANIELI, S. LAKÄMPER, CHRISTOPH F. SCHMIDT, AND L. GHEBER. **Directionality of individual kinesin-5 Cin8 motors is modulated by loop 8, ionic strength and microtubule geometry.** in press. 45
- [77] CHRISTINA THIEDE. *Funktionsanalyse von Kinesin-Motormolekülen mittels Einzelmolekül-Fluoreszenz.* Diploma thesis, Georg-August-Universität Göttingen, 2008. 45, 67, 96
- [78] F. J. NÉDÉLEC, T. SURREY, A. C. MAGGS, AND S. LEIBLER. **Self-organization of microtubules and motors.** *Nature*, **389**(6648):305–308, September 1997. 54
- [79] T. SURREY, F. NÉDÉLEC, S. LEIBLER, AND E. KARSENTI. **Physical Properties Determining Self-Organization of Motors and Microtubules.** *Science*, **292**(5519):1167–1171, 2001. 54
- [80] F. NÉDÉLEC, T. SURREY, AND E. KARSENTI. **Self-organisation and forces in the microtubule cytoskeleton.** *Curr. Opin. Cell Biol.*, **15**(1):118–124, February 2003. 54
- [81] F. C. MACKINTOSH AND A. J. LEVINE. **Nonequilibrium Mechanics and Dynamics of Motor-Activated Gels.** *Phys. Rev. Lett.*, **100**(1):018104, 2008. 57
- [82] O. LIELEG, M. M. A. E. CLAESSENS, Y. LUAN, AND A. R. BAUSCH. **Transient Binding and Dissipation in Cross-Linked Actin Networks.** *Phys. Rev. Lett.*, **101**(10):108101–, September 2008. 64
- [83] C. P. BROEDERSZ, M. DEPKEN, N. Y. YAO, M. R. POLLAK, D. A. WEITZ, AND F. C. MACKINTOSH. **Cross-Link-Governed Dynamics of Biopolymer Networks.** *Phys. Rev. Lett.*, **105**(23):238101–, November 2010. 64
- [84] L. STARRS AND P. BARTLETT. **One- \hat{A} and two-point micro-rheology of viscoelastic media.** *J. Phys. Condens. Matter*, **15**(1):S251–, 2003. 71
- [85] M. ATAKHORRAMI AND C. SCHMIDT. **High-bandwidth one-and two-particle microrheology in solutions of wormlike micelles.** *Rheol. Acta*, **45**(4):449–456, April 2006. 71

REFERENCES

- [86] F. C. MACKINTOSH. **Dynamics of microtubules in viscoelastic media.** Private communication. 72
- [87] C. P. BRANGWYNNE, G. H. KOENDERINK, F. C. MACKINTOSH, AND D. A. WEITZ. **Nonequilibrium Microtubule Fluctuations in a Model Cytoskeleton.** *Phys. Rev. Lett.*, **100**(11):118104, 2008. 72
- [88] A. CASPI, M. ELBAUM, R. GRANEK, A. LACHISH, AND D. ZBAIDA. **Semiflexible Polymer Network: A View From Inside.** *Phys. Rev. Lett.*, **80**(5):1106–, February 1998. 72, 75, 82, 84
- [89] M. M. TIRADO AND J. G. DE LA TORRE. **Translational friction coefficients of rigid, symmetric top macromolecules. Application to circular cylinders.** *J. Chem. Phys.*, **71**(6):2581–2587, September 1979. 74, 79
- [90] J. T. BULLERJAHN, S. STURM, L. WOLFF, AND K. KROY. **Monomer dynamics of a wormlike chain.** Unpublished - Private Communication. 75, 84
- [91] A. OTT, M. MAGNASCO, A. SIMON, AND A. LIBCHABER. **Measurement of the persistence length of polymerized actin using fluorescence microscopy.** *Phys. Rev. E*, **48**(3):R1642–R1645, September 1993. 83
- [92] L. LE GOFF, O. HALLATSCHKE, E. FREY, AND F. AMBLARD. **Tracer Studies on F-Actin Fluctuations.** *Phys. Rev. Lett.*, **89**(25):258101–, December 2002. 83
- [93] L. HOU, F. LANNI, AND K. LUBY-PHELPS. **Tracer diffusion in F-actin and Ficoll mixtures. Toward a model for cytoplasm.** *Biophys. J.*, **58**(1):31–43, July 1990. 83
- [94] M. N. GREEN. **Avidin.** *Adv. Protein Chem.*, **Volume 29**:85–133, 1975. 83
- [95] S. A. WALKER AND J. A. ZASADZINSKI. **Electrostatic Control of Spontaneous Vesicle Aggregation.** *Langmuir*, **13**(19):5076–5081, September 1997. 83
- [96] ConOptics Inc. *Data sheet: Electro-Optic Laser Beam Deflectors.* 118
- [97] F. DARDE. *Operating manual - 2 Axis deflectors DTSXY family with high frequency (-) configuration.* AA optoelectronic, Orsay, France. 117

Danksagung

“Verschiebe die Dankbarkeit nie”, hat Albert Schweitzer gefordert. Und dennoch kann ich ihr erst am Ende dieser Arbeit Ausdruck verleihen. Das Schreiben dieser Dissertation und die damit einhergehende Rückschau auf die vergangenen Jahre hat mir die zahllosen kleinen und großen Beiträge vor Augen geführt, aus denen diese Arbeit erwachsen ist und wie vielen Menschen daher mein Dank gebührt.

Bei meinem Betreuer Prof. Dr. Christoph F. Schmidt möchte ich mich dafür bedanken, dass ich als erster Doktorand in Göttingen meinen Beitrag zum Aufbau der Gruppe leisten durfte. Den tiefen Einblick in die biologische Physik, das immense fachliche Wissen und die Freiheiten bei der Forschung habe ich als äußerst bereichernd für mein Leben empfunden.

Weiterhin möchte ich an dieser Stelle Prof. Dr. Eberhard Bodenschatz für die Übernahme des Zweitgutachtens danken.

Zu Beginn meiner Arbeit, und auch bei späteren Besuchen in Göttingen, hat mir Prof. Dr. Daisuke Mizuno die Geheimnisse der Mikrorheologie nahegebracht und mich geduldig in die vielen Feinheiten dieser Wissenschaftskunst eingeführt. Unserer weiteren Zusammenarbeit sehe ich mit großer Spannung entgegen.

Die damaligen Diplomanden Christoph Pieper und Felix Zörgiebel haben mich, in einer amüsanten und lehrreichen Umkehrung der akademischen Hierarchie, am Anfang der Arbeit unter ihre Fittiche genommen. In vielen interessanten Stunden haben wir uns den Geheimnissen der “großen Falle” genähert und gemeinsam wertvolle Erfahrungen gesammelt, von denen ich noch heute zehre. Christoph hat mit seinen LabVIEW-Programmierkünsten den Grundstein für die Computersteuerung der optischen Fallen gelegt und damit unsere Arbeit enorm vereinfacht. Felix hat mich mit der Programmierlogik von MATLAB vertraut gemacht und viel Zeit und Mühe in die Entwicklung einer Mikrorheologie-Toolbox gesteckt, deren Umfang und Eleganz mich sehr beeindruckt hat.

Mein besonderer Dank gilt Dieter Hille, dem Leiter unserer feinmechanischen Werkstatt. Wie er und seine Mitarbeiter aus nebulösen Ideen und wilden Bleistiftskizzen ein ums andere Mal fein gearbeitete Bauteile gefertigt haben, hat mich immer wieder aufs Neue begeistert. Insbesondere für die vielen graue Haare, die die monatelange Planung, Revision, CAD-Zeichnung und anschließende maschinelle Bearbeitung des neuen Mikrorheologie-Aufbaus verursacht hat, möchte ich mich aufrichtig entschuldigen. Ohne ihr Engagement und ihr Fachwissen wäre die Realisierung dieses Projektes nicht möglich gewesen.

Bei Dr. Karl Lautscham und seinen Mitarbeitern aus der Elektronikwerkstatt bedanke ich mich für die Unterstützung in allen Fragen der Signalverarbeitung und die spezielle Anfertigung der zahlreichen elektronischen Bauteile.

Unseren "BTA's", Stefanie Kramer, Kerstin von Rhoden, Ulrike Schulz und Charlotte "Charley" Willms, danke ich ganz herzlich für die viele biochemische "schwarze Magie" rund um die Proteinaufreinigung, Puffer-Herstellung und Funktionalisierung. Die lange Extraktionsprozedur vom noch warmen Muskelfleisch des Huhns bis hin zum "gebrauchsfertig" aufgereinigten Actin-Molekül war eine interessante Erfahrung. Selten hat man in der Physik die Möglichkeit der Zerlegung eines komplexen Problems in seine Bestandteile so hautnah beizuwohnen.

Für die Unterstützung in allen EDV-Fragen bedanke ich mich bei Thomas Geiling.

Christopher Battle danke ich für die gemeinsamen Stunden des Experimentierens an unseren Mikroskopaufbauten, die vielen fachlichen Diskussionen über optische Fallen und die außerfachlichen Diskussionen über Gott und die Welt, sowie das Korrekturlesen dieser Arbeit in letzter Minute.

Dr. Florian Rehfeldt möchte ich für seine Hilfsbereitschaft in allen experimentellen Fragen und die Zeit, die er sich stets genommen hat, ebenso danken, wie für das Korrekturlesen dieser Arbeit.

Obwohl ich nicht Mitglied seiner Gruppe war, hat mir Dr. Iwan Schaap stets tatkräftig und mit großer Begeisterung bei allen experimentellen Problemen der Optik weitergeholfen.

Dr. Nikta Fakhri gebührt mein Dank für die Präparation der COS-Zellen in einer Nacht-und-Nebel Aktion zwölf Tage vor der Abgabefrist. Selten bin ich Menschen mit solch großem Enthusiasmus für die Wissenschaft begegnet.

Mit Florian Schlosser und André Düselder hat mich nicht nur die gemeinsame Arbeit an der optischen Falle, sondern auch der gleiche, exquisite Musikgeschmack verbunden.

Hendrik Söhnholz bin ich für das Ausleihen des Beam Profilers zu Dank verpflichtet, den ich wesentlich länger okkupiert habe, als ursprünglich veranschlagt.

Allen Sekretärinnen des Dritten Physikalischen Instituts, des Sonderforschungsbereichs 755 und der Göttinger Graduiertenschule für Neurowissenschaften, Biophysik und Molekulare Biowissenschaften danke ich ganz herzlich für die allzeit freundliche Unterstützung bei allen Anträgen, Formularen, Verwaltungsakten und die Organisation der zahlreichen interessanten Sommer- und Winterschulen.

Allen wechselnden Teilnehmern der “Bertrand Russell Ranch” danke ich für die faszinierenden und tiefeschürfenden philosophischen Diskussionen über das Leben, das Universum und den ganzen Rest.

Bei den Mitgliedern der Göttinger Modern Arnis Gruppe möchte ich mich für alle gewalttätigen Formen der Stressbewältigung bedanken, die ich mit wachsender Begeisterung ausgeübt habe. Ihr habt das Unmögliche vollbracht: einen eingefleischten Sportmuffel wie mich zu bekehren. Ich freue mich schon darauf, wieder mit Euch die Stöcke kreuzen zu dürfen.

Die Arbeit wurde finanziell unterstützt vom SFB755, der GGNB und der Deutschen Forschungsgemeinschaft.

Zu guter Letzt möchte ich mich bei meiner Familie, und besonders meinem Bruder Marcus, für die Unterstützung in allen Lebenslagen und gerade in den schweren und dunklen Stunden bedanken. Ohne Euren Rückhalt und Euer Vertrauen wäre diese Arbeit nicht zustande gekommen.

Danke.